Phase Transitions in Strongly Interacting Quantum Systems

By

Christopher Nicholas Varney
B.S. (Northern Arizona University) [2004]
M.S. (University of California, Davis) [2005]

DISSERTATION

Submitted in partial satisfaction of the requirements for the degree of

DOCTOR OF PHILOSOPHY

in

PHYSICS

in the

OFFICE OF GRADUATE STUDIES

of the

UNIVERSITY OF CALIFORNIA

DAVIS

Approved:

[Richard T. Scalettar] (Chair)

[Warren E. Pickett]

[Ching-Yao Fong]

Committee in Charge
2009

For Rebecca, my father Dana, my mother Donna, and my late grandparents Richard and Jeanette.

Contents

List of Figures

Abstract

Strongly correlated materials exhibit some of the most complex and technologically useful phenomena in condensed matter. We use the world line and determinant quantum Monte Carlo techniques to explore the phases of the Hubbard Hamiltonian, a model describing strong interactions, in a number of different contexts. We first consider the spin, charge, and bond order correlations of the one-dimensional extended fermion Hubbard model in the presence of a coupling to the lattice. A static alternating lattice distortion leads to enhanced charge density wave correlations at the expense of antiferromagnetic order. When the lattice degrees of freedom are dynamic, we show that a similar effect occurs even though the charge asymmetry must arise spontaneously. Although the evolution of the total energy with lattice coupling is smooth, the individual components exhibit sharp crossovers at the phase boundaries. Finally, we observe a tendency for bond order in the region between the charge and spin density wave phases.

Second, we examine mixtures of bosons and fermions in one-dimensional optical lattices. We evaluate the density profiles and bosonic visibility $\mathcal{V}_b$, resolving the discrepancy between theory and experiment by identifying parameter regimes where $\mathcal{V}_b$ is reduced and increased. We present a simple qualitative picture of the different response to the fermion admixture in terms of the superfluid and Mott-insulating domains before and after the fermions are included. Finally, we show that $\mathcal{V}_b$ exhibits kinks which are tied to the domain evolution present in the pure bosonic case, and also additional structure arising from the formation of boson-fermion molecules, a prediction for future experiments.

Third, we report large scale calculations of the effective bandwidth, momentum distribution, and magnetic correlations of the square lattice fermion Hubbard Hamiltonian. The sharp Fermi surface of the non-interacting limit is significantly broadened by the electronic correlations, but retains signatures of the approach to the edges of

the first Brillouin zone as the density increases. Finite size scaling of simulations on large lattices allows us to extract the interaction dependence of the antiferromagnetic order parameter, exhibiting its evolution from weak-coupling to the strong-coupling Heisenberg limit. Our lattices provide improved resolution of the momentum distribution, allowing a more quantitative comparison with time-of-flight optical lattice experiments.

Acknowledgments

There are many tremendous people that have helped me become the person I am today. First and foremost, I would like to thank my advisor, Professor Richard Scalettar, for being encouraging and absolutely brilliant in his guidance. None of this would have been possible without him. I would like to give a heartfelt thank you to Robert Blackford, who inspired me to study physics in the first place. A special thanks to Gus Hart, whose love of Condensed Matter physics was so contagious that I fell in love with the field.

Thanks to David Lagattuta and Christopher Ellison for a number of illuminating arguments and discussions in front of the chalkboard. A special thanks to Damien Martin for seemingly understanding everything. Thanks to John Stilley and Carley Kopecky for interesting luncheons that revolved around physics. In addition, I had a number of stimulating discussions with many of my colleagues. For this I would also like to acknowledge Robert Forrest, Dr. Emily Ashbaugh-West, Quan Yin, Dr. Erik Ylvisaker, and all of the others that I forget to mention here. I would also like to thank Laura Peterson, Georgie Tolle, Onelia Yan, and the rest of the office staff for always taking care of any administrative tasks.

I would like to thank Dr. Norman Paris for explaining the basics of determinant quantum Monte Carlo. Thanks to Andrew Baldwin for discussions on computational techniques. Thanks to Dr. Brian Moritz for conversations regarding the Dynamical Cluster Approximation. Thanks to Dr. Khan Mahmud for helping me to understand how to relate the experimental optical lattice parameters with those of the Hubbard model. Many thanks to Dr. Simone Chiesa for numerous discussions on computational methods, the Hubbard model, and optical lattices.

Thanks to Helen Craig for her code writing and contributions to Chapter 3. A special thanks to Dr. Valery Rousseau for the use of his code for Chapter 4. I would also like to acknowledge the contributions of the many collaborators for the work

in Chapter 5: Dr. Simone Chiesa for the concept of the excluded structure factor, Dr. Che-Rung Lee and Professor Zhaojun Bai for their contributions to QUEST, and Dr. Mark Jarrell for his insight. In addition, I would like to thank the members of my qualifying exam committee, Professors Warren Pickett, Sergei Savrasov, Rena Zieve, Daniel Cebra, and Bruno Nachtergaele. Also, a special thanks to Professors Richard Scalettar, Warren Pickett and Ching-Yao Fong for their helpful suggestions while proof-reading this dissertation.

I would like to thank my parents, for their unyielding support at every point in my life, for encouraging me to pursue my dreams no matter the cost. Finally, I would like to thank Rebecca, who has been tremendous from the moment she entered my life.

Chapter 1

Introduction

1.1 Strongly Correlated Systems

One of the primary goals of science is to explain and, if possible, predict the various phenomena present in nature. In condensed matter physics, one of the most successful theories of electrons in a material is band theory. Its biggest success is also one of its biggest failures. By constructing energy bands and filling them up with the known number of fermions, it was able to explain why certain materials are metallic, semiconducting, or insulating. However, it failed at explaining the insulating behavior of systems in which the electronic correlations are strong. For instance, it incorrectly predicts the transition metal oxides MnO, FeO, CoO, NiO, and CuO as metals, when they are in fact insulators. Moreover, band theory produces energy gaps which are roughly an order of magnitude too small for many insulators and semi-conductors. Strong correlations play an important role in a wide variety of physical phenomena besides electrical transport. Electronic correlations are vital components to any description of the Mott metal-insulator transition and magnetism, charge ordering, and superconductivity in heavy fermions, the high-T_c superconductors, the Kondo effect, ultra-cold gases in optical lattices, and others.

Perhaps the biggest impediment to understanding the correlations in a material is simulation time. If, for example, we had attempted to simulate the exact interactions and particle number in a material, the calculation would be for roughly 10^{23} atoms, and as such this calculation would take far longer than the lifetime of the universe! Left with such an unpalatable means of understanding materials, there remains only one truly viable choice: simplifying the interactions and the number of electrons to something that can be handled numerically in a reasonable amount of time. In doing this, we can still gain tremendous insight into the most important mechanisms that are responsible for different physical phenomena, as this dissertation will demonstrate. The choice of the model we study in our attempts to understand a particular experiment is influenced by a number of questions. Are the phonon modes important? Is the electron-electron interaction screened? Is magnetism present? Is it an insulator or a metal? Does the material superconduct, and, if so, at what concentrations?

There are literally dozens of Hamiltonians that have been studied extensively as models for the interactions in a solid. Of these, the simplest is the Hubbard model,

$$H = -t \sum_{\langle i,j \rangle} \sum_{\sigma} \left(c^{\dagger}_{i\sigma} c_{j\sigma} + \text{h.c.} \right) + U \sum_{i} n_{i\uparrow} n_{i\downarrow} - \mu \sum_{i} n_{i} \,, \tag{1.1}$$

which is the main subject of this dissertation. It was developed independently by Gutzwiller [1], Hubbard [2–5], and Kanamori [6] in 1963 as a model for electrons occupying d-bands in transition metals. It has since been used to describe the electronic properties of solids with small bandwidths, magnetism in the transition metal oxides (a small selection of the relevant work in this area can be found in Refs. 7–11), the Mott metal-insulator transition [12, 13], the electronic properties of the high-T_c cuprates [14–17] and heavy fermions [18], and the properties of ultra-cold atomic gases confined in an optical lattice [19–25].

In the remainder of this chapter, I will derive the Hubbard Hamiltonian, discuss

its properties in various limits, its symmetries, and also discuss the properties of two extensions of the model: the Extended Hubbard and the Bose-Hubbard models. It is assumed that the reader has a firm understanding of solid state physics [26, 27] and second quantization [28, 29].

1.2 Fermion Hubbard Model

As mentioned in Sec. 1.1 above, the Hubbard model was developed by Gutzwiller, Hubbard, and Kanamori [1–6]. There are many excellent reviews of the Hubbard model that discuss its motivation and properties. I shall, however, refer the reader to two excellent resources [30, 31] for details not discussed here.

Let us imagine a solid. It is comprised of ions and electrons in a crystalline structure. Comparatively, the ions are significantly heavier than the electrons and barely move. It is therefore a reasonable assumption that the ions form a static lattice and that a many-body Hamiltonian describing the dynamics of the electrons can be written as

$$H = \sum_{i=1}^{N} \left(\frac{\mathbf{p}_i}{2m} + U_{\text{ion}}(\mathbf{r}_i) \right) + \sum_{i \neq j} U_{e-e}(\mathbf{r}_i - \mathbf{r}_j) \,, \tag{1.2}$$

where N is the number of electrons in the solid; $\mathbf{r}_i$ and $\mathbf{p}_i$ are the electron position and momenta, respectively; $\mathbf{R}_i$ and $\mathbf{P}_i$ are the ion position and momenta, where we take $\mathbf{P}_i = 0$ and the ion positions to be frozen; $U_{\text{ion}}(\mathbf{r})$ is the periodic potential of the ions; and

$$U_{e-e}(\mathbf{r}) = \frac{e^2}{\|\mathbf{r}\|} \tag{1.3}$$

is the Coulomb repulsion between the electrons. The first term in the Hamiltonian is the one-body piece h_1, while the second term is a two-body interaction. Equation (1.2)

can be written in second-quantized form. Let us first consider the eigenstates of the one-particle Hamiltonian. Because $U_{\text{ion}}(\mathbf{r})$ is periodic, the eigenfunctions are Blöch functions and of the form

$$\varphi_{\alpha\mathbf{k}}(\mathbf{r}) = e^{i\mathbf{k}\cdot\mathbf{r}} u_{\alpha\mathbf{k}}(\mathbf{r})\,, \tag{1.4}$$

where $u_{\alpha\mathbf{k}}(\mathbf{r})$ has the periodicity of the lattice, α is the band index, and $\mathbf{k}$ is the wave vector. For the following, we shall assume that there is only one band near the Fermi energy and all remaining bands are completely occupied or empty. This allows us to ignore the band index, $\varphi_{\alpha\mathbf{k}}(\mathbf{r}) = \varphi_{\mathbf{k}}(\mathbf{r})$. The Blöch functions $\varphi_{\mathbf{k}}$ form a basis of one-particle states.

It is advantageous to instead choose a basis that is localized around the ions. We therefore choose a basis complementary to the eigenfunctions of the one-particle Hamiltonian, the Wannier functions

$$\phi(\mathbf{r} - \mathbf{R}_j) = \frac{1}{\sqrt{L}} \sum_{\mathbf{k}} \varphi_{\mathbf{k}}(\mathbf{r} - \mathbf{R}_j)\,, \tag{1.5}$$

where $\mathbf{R}_j$ is a lattice vector and L is the number of ions in the lattice. Here the Wannier functions $\phi(\mathbf{r} - \mathbf{R}_j)$ are centered about $\mathbf{R}_j$ and are orthogonal for different site indices j. If we express the Blöch functions in terms of the Wannier functions, we have

$$\varphi_{\mathbf{k}}(\mathbf{r}) = \frac{1}{\sqrt{L}} \sum_{j} e^{i\mathbf{k}\cdot\mathbf{R}_j} \phi(\mathbf{r} - \mathbf{R}_j)\,. \tag{1.6}$$

Next, let us introduce the particle creation operator $c^\dagger_{j\sigma}$, which creates electrons of spin σ in the combination of Blöch states $\varphi_{\mathbf{k}}(\mathbf{r})$ centered at $\mathbf{R}_j$. This allows us to introduce a corresponding field operator $\Psi^\dagger_\sigma(\mathbf{r})$, which creates an electron of spin σ

at position $\mathbf{r}$,

$$\Psi_\sigma^\dagger(\mathbf{r}) = \sum_j \phi^*(\mathbf{r} - \mathbf{R}_j) c_{j\sigma}^\dagger \,. \tag{1.7}$$

We can relate first and second quantization formalizations for the Hamiltonian by the formula [28, 32]

$$\begin{aligned} H = &\sum_{\sigma=\uparrow,\downarrow} \int d^3r \, \Psi_\sigma^\dagger(\mathbf{r}) h_1 \Psi_\sigma(\mathbf{r}) \\ &+ \frac{1}{2} \sum_{\sigma\sigma'} \int d^3r \int d^3r' \, \Psi_\sigma^\dagger(\mathbf{r}) \Psi_{\sigma'}^\dagger(\mathbf{r}') U(\mathbf{r}, \mathbf{r}') \Psi_{\sigma'}(\mathbf{r}') \Psi_\sigma(\mathbf{r}) \,. \end{aligned} \tag{1.8}$$

Expressing the Hamiltonian in the basis of Wannier functions yields,

$$H = \sum_{\alpha,i,j,\sigma} t_{ij} c_{i,\sigma}^\dagger c_{j,\sigma} + \sum_{i,j,k,l} \sum_{\sigma,\sigma'} U_{ijkl} c_{i,\sigma}^\dagger c_{j,\sigma'}^\dagger c_{k,\sigma'} c_{l,\sigma} \,. \tag{1.9}$$

The hopping matrix elements t_{ij} are

$$t_{ij} = \int dr^3 \, \phi^*(\mathbf{r} - \mathbf{R}_i) h_1 \phi(\mathbf{r} - \mathbf{R}_j) = \frac{1}{L} \sum_{\mathbf{k}} e^{i\mathbf{k}\cdot(\mathbf{R}_i - \mathbf{R}_j)} \varepsilon_{\mathbf{k}} \tag{1.10}$$

The interaction term U_{ijkl} can be expressed as an overlap integral

$$U_{ijkl} = \int d^3r \int d^3r' \, \phi^*(\mathbf{r} - \mathbf{R}_i) \phi^*(\mathbf{r}' - \mathbf{R}_j) U(\mathbf{r}, \mathbf{r}') \phi(\mathbf{r}' - \mathbf{R}_k) \phi(\mathbf{r} - \mathbf{R}_l) \,. \tag{1.11}$$

Equation (1.9), which retains long range interactions, is equivalent to Eq. (1.2), and the Hubbard model is obtained when the electron-electron interaction is heavily screened so that only the onsite piece U_{iiii} remains and when we assume that the Wannier functions $\phi(\mathbf{r} - \mathbf{R}_i)$ are heavily localized around $\mathbf{R}_i$, as is true in the tight-binding approximation. Because the Wannier functions are heavily localized, the hopping matrix elements t_{ij} will be largest for nearest neighbor hoppings, allowing

us to ignore kinetic energy terms that are long range. If we introduce the particle number operators $n_{i\sigma} = c^\dagger_{i\sigma} c_{i\sigma}$, the Hamiltonian finally reduces to

$$H = -t \sum_{\langle i,j \rangle} \sum_{\sigma} \left(c^\dagger_{i\sigma} c_{j\sigma} + \text{h.c.} \right) + U \sum_i n_{i\uparrow} n_{i\downarrow} \,. \tag{1.12}$$

Because the Hamiltonian commutes with the number operator, we can subtract the term $\mu \sum_i n_i$, where μ is the chemical potential that sets the filling.

There are, of course, numerous descendents to the fermion Hubbard model. Many of these are discussed in Refs. 33 and 34. I shall consider one of these, the Extended Fermion Hubbard model, at length in Sec. 1.3.

1.2.1 Limiting Cases

There are a handful of special cases where the Hubbard model has an exact solution. In one-dimension, the Hubbard model is solved exactly by the Bethe-ansatz [30]. It can also be solved exactly in the non-interacting limit $U = 0$ and in the atomic limit $t = 0$, which is also referred to as the one-site Hubbard model as the different lattice sites do not communicate. First, let us examine the non-interacting result. The tight binding Hamiltonian is

$$H = -t \sum_{\langle i,j \rangle} \sum_{\sigma} \left(c^\dagger_{i\sigma} c_{j\sigma} + \text{h.c.} \right) - \mu \sum_i n_i \,. \tag{1.13}$$

The creation(annihilation) operator can be expressed in terms of the quasimomentum by means of a Fourier transform

$$c^\dagger_{j\sigma} = \frac{1}{\sqrt{L}} \sum_{\mathbf{k}} e^{-i\mathbf{k}\cdot\mathbf{R}_j} c^\dagger_{\mathbf{k}\sigma} \,. \tag{1.14}$$

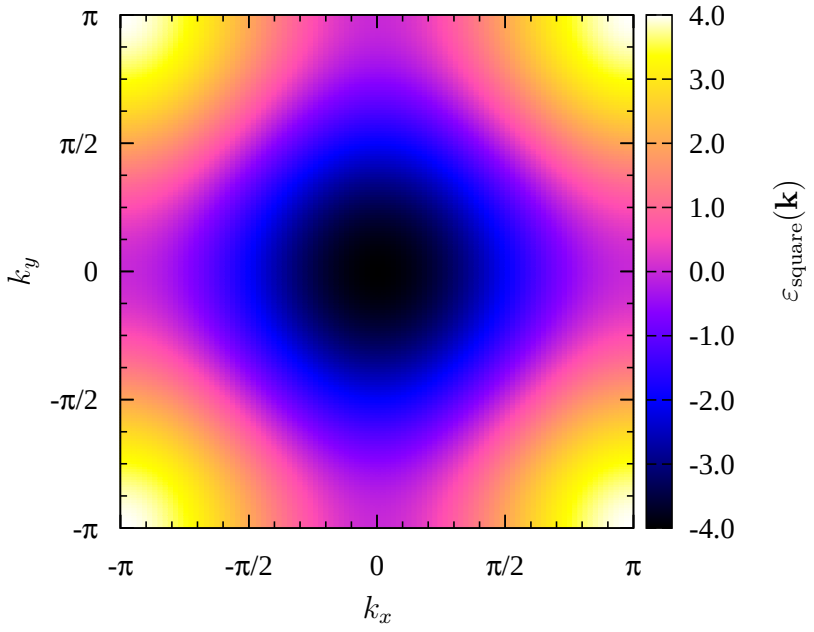

Figure 1.1: Color contour plot depiction of the dispersion relation $\varepsilon_{\text{square}}(\mathbf{k})$ in the non-interacting limit for $t = 1$ For ε close to the band minimum $\varepsilon_0 = -4t$, the Fermi surface is a circle, as expected since $\varepsilon(\mathbf{k}) \sim -4 + (k_x^2 + k_y^2)$. As ε increases, the circles become increasingly distorted, as seen in Fig. 1.3.

The Hamiltonian therefore becomes

$$H = -\frac{t}{L}\sum_{\langle i,j\rangle}\sum_{\sigma}\sum_{\mathbf{k},\mathbf{k}'}\left(e^{-i\mathbf{k}\cdot\mathbf{R}_i}e^{i\mathbf{k}'\cdot\mathbf{R}_j} + \text{h.c.}\right)c^{\dagger}_{\mathbf{k}\sigma}c_{\mathbf{k}'\sigma} - \frac{\mu}{L}\sum_{i}\sum_{\mathbf{k},\mathbf{k}'}e^{i(\mathbf{k}'-\mathbf{k})\cdot\mathbf{R}_i}c^{\dagger}_{\mathbf{k}\sigma}c_{\mathbf{k}'\sigma}\,. \tag{1.15}$$

Next, we utilize the symmetry of our lattice to sum over nearest neighbors. In turn, the tight-binding Hamiltonian can be written simply as

$$H = \sum_{\mathbf{k}\sigma}(\varepsilon_{\mathbf{k}} - \mu)c^{\dagger}_{\mathbf{k}\sigma}c_{\mathbf{k}\sigma}\,, \tag{1.16}$$

where $\varepsilon_{\mathbf{k}}$ is the dispersion relation. The dispersion relation depends on the symmetry of the lattice. The dispersion relations for the 1D, square, triangular, and cubic

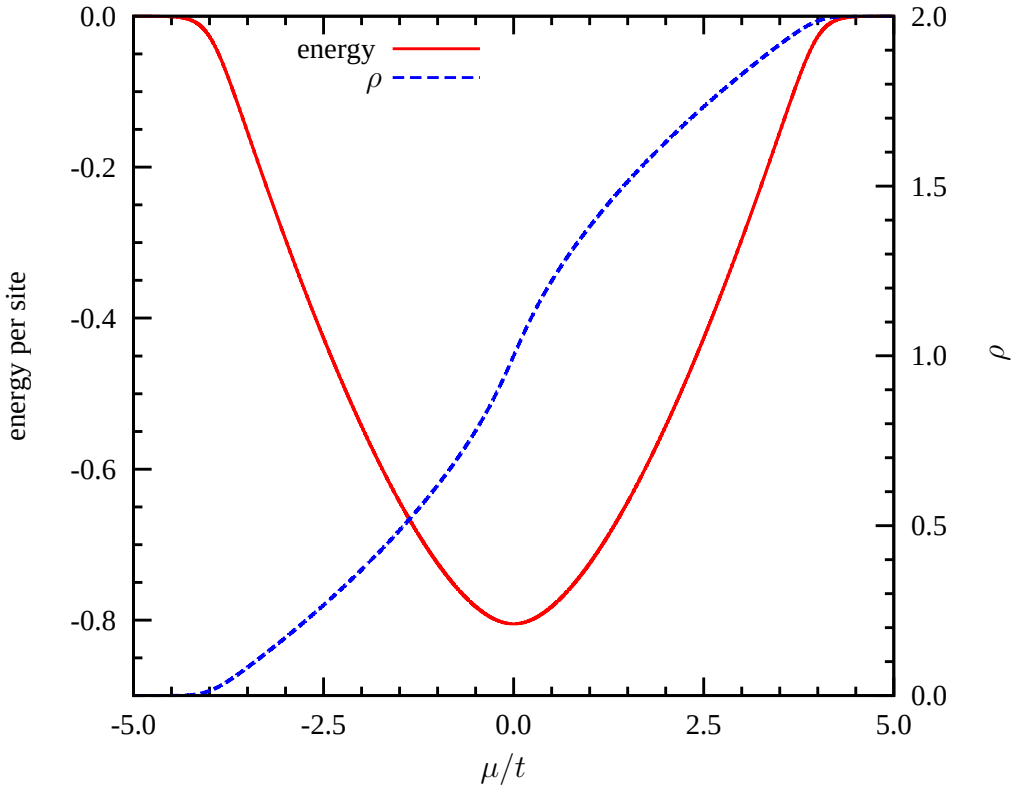

Figure 1.2: Energy per site (red) and density ρ (blue) versus chemical potential μ/t for the $U = 0$ Hubbard model on a square lattice at $\beta t = 8$.

lattices, respectively, are:

$$\varepsilon_{\mathrm{1D}}(k) = -2t \cos k \,, \tag{1.17a}$$

$$\varepsilon_{\mathrm{square}}(\mathbf{k}) = -2t(\cos k_x + \cos k_y) \,, \tag{1.17b}$$

$$\varepsilon_{\mathrm{triangular}}(\mathbf{k}) = -2t \left[\cos k_x + 2 \cos \left(\frac{1}{2} k_x \right) + \cos \left(\frac{\sqrt{3}}{2} k_y \right) \right] \,, \tag{1.17c}$$

$$\varepsilon_{\mathrm{cubic}}(\mathbf{k}) = -2t(\cos k_x + \cos k_y + \cos k_z) \,. \tag{1.17d}$$

Let us examine the properties of the square lattice in the non-interacting limit. In Fig. 1.1, the dispersion relation is shown as a function of the quasi-momentum. Next,

in Fig. 1.2, are the energy per site and the filling

$$\rho = \sum_{\mathbf{k}} f(\mathbf{k}) = \sum_{\mathbf{k}} \left[e^{\beta\epsilon(\mathbf{k})-\mu} + 1 \right]^{-1} \tag{1.18}$$

as functions of the chemical potential μ (in the units of the hopping parameter t). Half-filling occurs at $\mu = 0$ and coincides with the minimum in the energy curve. Lastly, we show the momentum distribution,

$$n(\mathbf{k}) = \langle c^{\dagger}_{\mathbf{k}\sigma} c_{\mathbf{k}\sigma} \rangle \ , \tag{1.19}$$

in Fig. 1.3 for densities $\rho = 0.1, 0.5, 1.0, 1.5$, and 1.9. The momentum distribution is a representation of the Fermi surface of the system. At low densities, the Fermi surface is circular. This is also true at high densities, where the unoccupied region of the Fermi surface is a circle centered around the corners of the first Brillioun zone. This is a consequence of particle-hole symmetry, present in Eqns. (1.17a), (1.17b), (1.17d), but not Eq. (1.17c). At half-filling, the square lattice Fermi surface exhibits perfect nesting with ordering vector $\mathbf{Q} = (\pi, \pi)$, which, as we shall see in Chapter 5, is crucial to the antiferromagnetic correlations at half-filling.

Now, what happens when the hopping parameter is turned off? When $t = 0$ the different lattice sites are completely disconnected. Thus, we effectively have a one-site system that has four possible states: $|\cdot\rangle, |\uparrow\rangle, |\downarrow\rangle, |d\rangle = |\uparrow\downarrow\rangle$. It is clear that we can use statistical mechanics to exactly solve the Hubbard model in this limit. Before we discuss the properties, let us shift the chemical potential of the system by a factor of $U/4$ so that we can write the Hamiltonian in a more symmetric fashion:

$$H = U \sum_i \left(n_{i\uparrow} - \frac{1}{2} \right) \left(n_{i\downarrow} - \frac{1}{2} \right) - \mu \sum_i n_i \tag{1.20}$$

The partition function and the density are

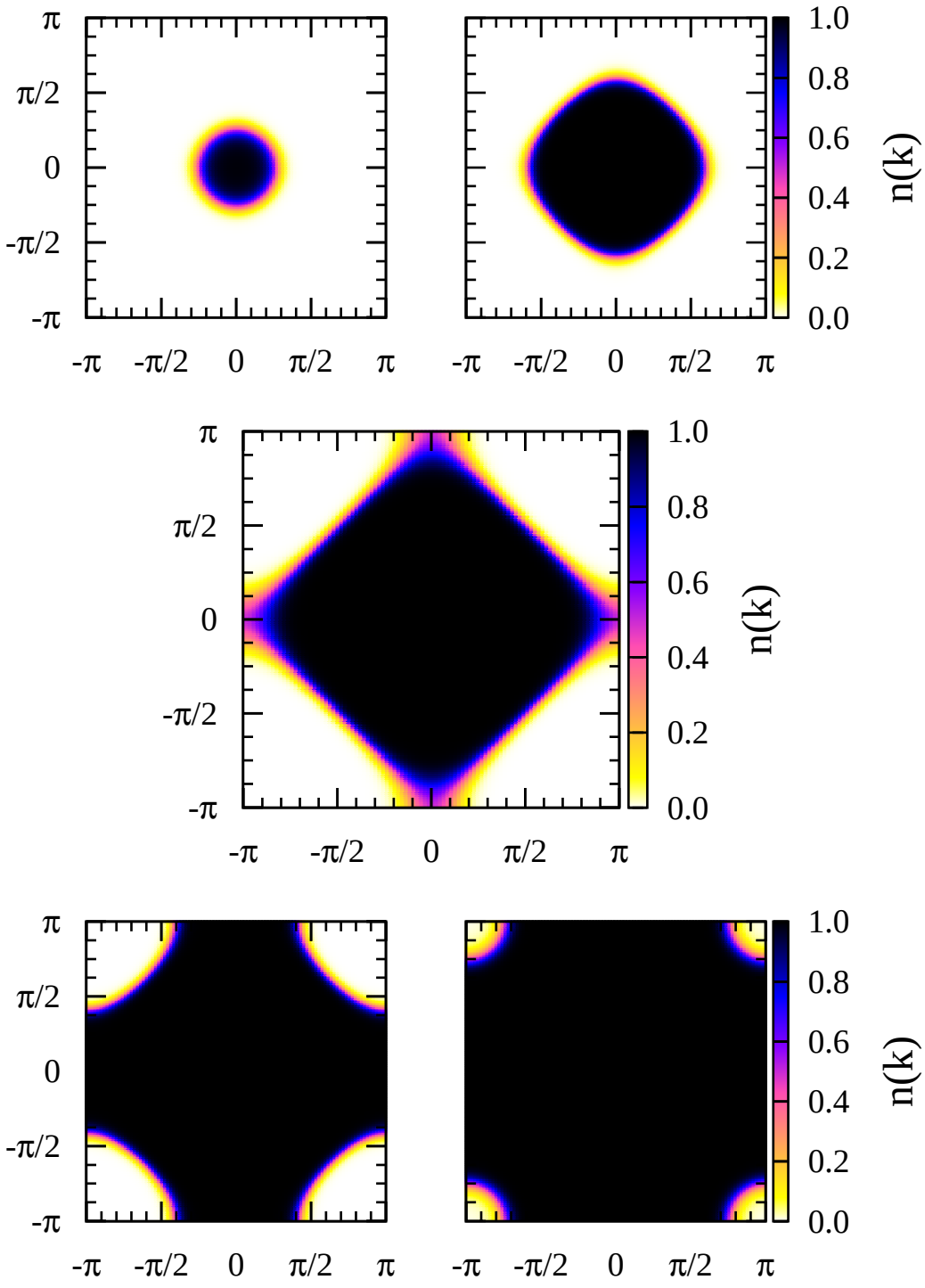

Figure 1.3: Color contour plot depiction of the momentum distribution $n(\mathbf{k})$ on a square lattice in the non-interacting limit for $\rho = 0.1, 0.5, 1.0, 1.5$, and 1.9 and inverse temperature $\beta t = 8$. The momentum distribution at half-filling, $\rho = 1.0$, exhibits perfect nesting with ordering vector $\mathbf{Q} = (\pi, \pi)$.

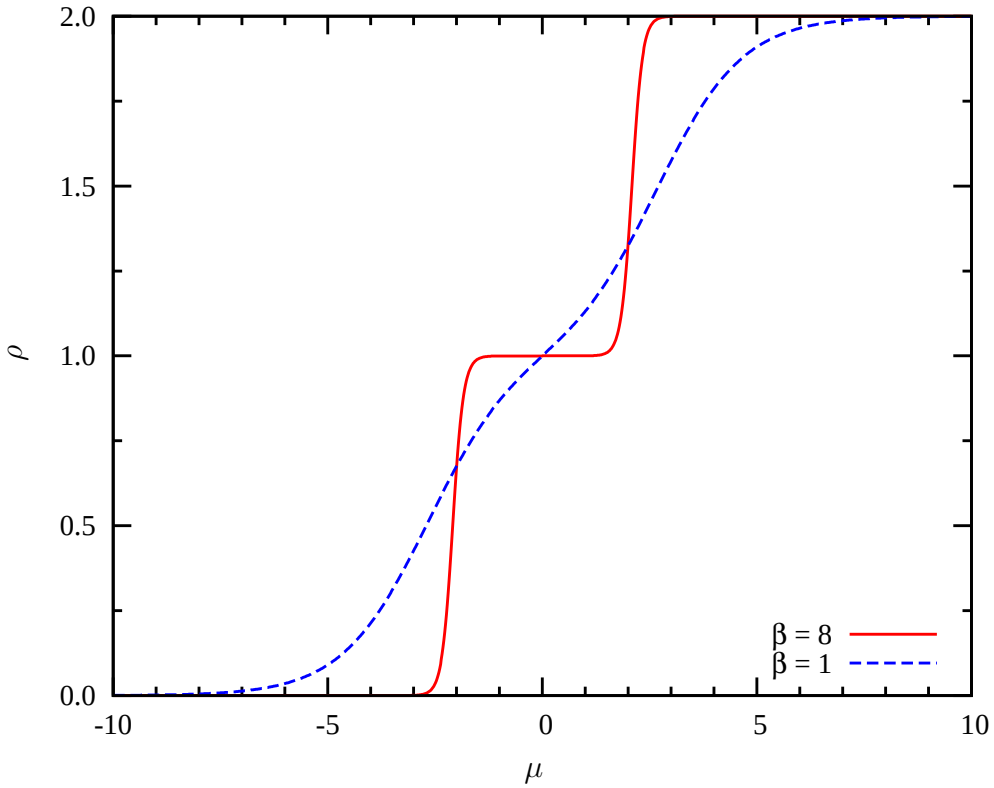

Figure 1.4: Density versus chemical potential μ for the one-site Hubbard model with $U = 4$ and inverse temperatures $\beta = 1, 8$. Here, for the particle-hole symmetric form of the interaction $U(n_\uparrow - \frac{1}{2})(n_\downarrow - \frac{1}{2})$, half-filling ($\rho = 1$) occurs at chemical potential $\mu = 0$. If the interaction is instead $Un_\uparrow n_\downarrow$, then $\mu = U/2 = 2$ gives $\rho = 1$.

$$\mathcal{Z} = \mathrm{Tr}\left[e^{-\beta H}\right] = e^{-\beta U/4} + 2e^{\beta(U/4+\mu)} + e^{-\beta(U/4-2\mu)}\,, \tag{1.21}$$

$$\rho = \mathcal{Z}^{-1}\mathrm{Tr}\left[n\, e^{-\beta H}\right] = \frac{2\left(e^{\beta(U/4+\mu)} + e^{-\beta(U/4-2\mu)}\right)}{e^{-\beta U/4} + 2e^{\beta(U/4+\mu)} + e^{-\beta(U/4-2\mu)}}\,, \tag{1.22}$$

respectively. Figure 1.4 shows the density for $U = 4$ and inverse temperatures $\beta = 1$ and 8. The plateau at $\rho = 1$ is known as the Mott plateau and is one of the crucial signatures of strong interactions. It is due to the high energy cost in doubly occupying a site, especially at low temperatures. This is clearly evident in Fig. 1.4, where for $\beta = 8$ the size of the gap is approximately equal to U. In fact, just as thermal fluctuations can destroy the plateau, so too can t wipe out the effects of U. Quantum fluctuations make it easier for a particle to overcome the energy gap, destroying the plateau. For the Hubbard model, the energy ratio U/t is central to

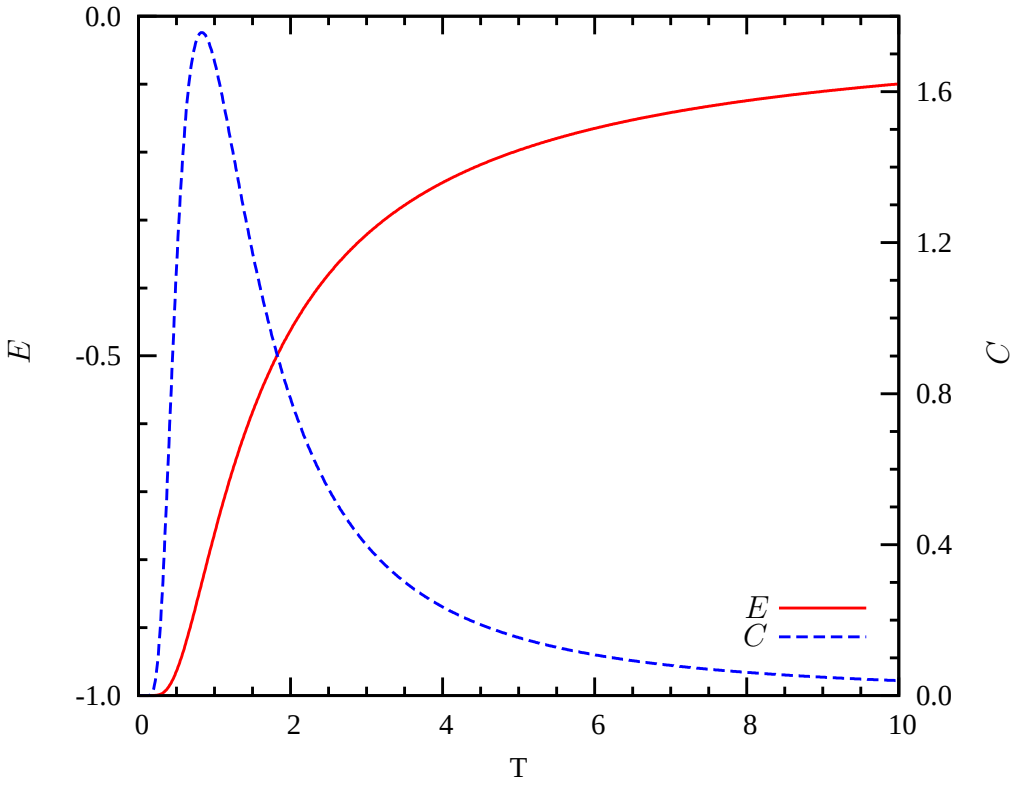

Figure 1.5: Energy (red) and specific heat C (blue) as functions of temperature for the one-site Hubbard model with $U = 4$.

the physics. We can also write expressions for the energy, specific heat, and local moment $\langle m^2 \rangle \equiv \langle (n_\uparrow - n_\downarrow)^2 \rangle$. At half-filling, we find

$$E = \mathcal{Z}^{-1} \mathrm{Tr} \left[H \, e^{-\beta H} \right] = -\frac{U}{4} \tanh \left(\frac{\beta U}{4} \right) , \tag{1.23}$$

$$C = \frac{dE}{dT} = \left(\frac{\beta U}{4} \right)^2 \mathrm{sech}^2 \left(\frac{\beta U}{4} \right) , \tag{1.24}$$

$$\langle m^2 \rangle = \mathcal{Z}^{-1} \mathrm{Tr} \left[(n_\uparrow - n_\downarrow)^2 e^{-\beta H} \right] = \left(1 + e^{-\beta U/2} \right)^{-1} . \tag{1.25}$$

In Fig. 1.5, we show the energy and specific heat versus temperature for $U = 4$. Here the peak in the specific heat is simply the Schottky anomaly. At $\mu = 0$, the one-site Hubbard Hamiltonian is a two-level system, and the increase in C at low temperatures is due to thermal population of the discrete energy levels. Next, Fig. 1.6 shows the local moment for $U = 4, 8$ as a function of temperature and for temperatures $T =$

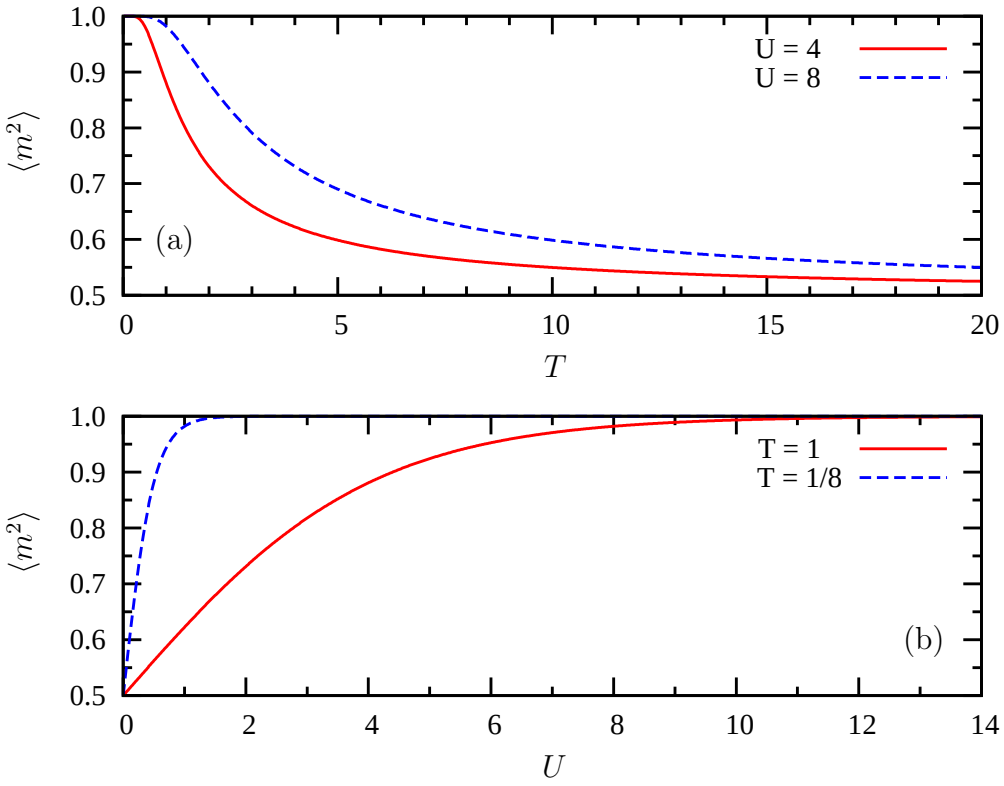

Figure 1.6: Local moment $\langle m^2 \rangle$ for the one-site Hubbard model at half-filling (a) as a function of temperature T for $U = 4, 8$ and (b) as a function of interaction strength U for temperatures $T = 0.125, 1$.

$0.125, 1$ as a function of U. For weak interaction and large temperatures, $\langle m^2 \rangle = 0.5$, whereas as for large U or low temperatures, a moment forms and the local moment approaches 1.

1.2.2 Symmetries

The Hubbard model has a number of symmetries that can be exploited. In particular, we are interested in two such symmetries: spin-rotational invariance and particle-hole symmetry.

It should be fairly obvious that the kinetic energy term of the Hubbard Hamiltonian is already spin-rotationally invariant (as we chose a basis with the spin in the z-direction). The invariance of the interaction term is not quite obvious. Let us

rewrite it as follows:

$$n_{j\uparrow}n_{j\downarrow} = c^\dagger_{j\uparrow}c_{j\uparrow}c^\dagger_{j\downarrow}c_{j\downarrow} = c^\dagger_{j\uparrow}c_{j\uparrow}(1 - c_{j\downarrow}c^\dagger_{j\downarrow}) = n_{j\uparrow} - S^+_j S^-_j \,. \tag{1.26}$$

where the spin raising operator $S^+_j = c^\dagger_{j\uparrow}c_{j\downarrow}$ converts a spin-down fermion to spin-up and $S^-_j = (S^+_j)^\dagger$. We can write a similar expression for the interaction term

$$n_{j\uparrow}n_{j\downarrow} = n_{j\downarrow} - S^-_j S^+_j \,. \tag{1.27}$$

Next, let us take the square of the z-component of the spin,

$$(S^z_j)^2 = \frac{1}{4}(n_{j\uparrow} - n_{j\downarrow})^2 = \frac{1}{4}(n^2_{j\uparrow} - 2n_{j\uparrow}n_{j\downarrow} + n^2_{j\uparrow}) = \frac{1}{4}(n_j - 2n_{j\uparrow}n_{j\downarrow}) \,. \tag{1.28}$$

where we have used $n^2_{j\sigma} = n_{j\sigma}$ and $n_j = n_{j\uparrow} + n_{j\downarrow}$. Solving for the interaction term yields

$$n_{j\uparrow}n_{j\downarrow} = \frac{1}{2}n_j - 2(S^z_j)^2 \,. \tag{1.29}$$

Combining Eqns. (1.26), (1.27) and (1.29), we find that the interaction term becomes

$$n_{j\uparrow}n_{j\downarrow} = \frac{1}{2}n_j - \frac{2}{3}\mathbf{S}^2_j \tag{1.30}$$

and that the part of the Hubbard Hamiltonian becomes

$$\frac{UN}{2} - \frac{2U}{3}\sum_j \mathbf{S}^2_j \,. \tag{1.31}$$

By expressing the Hamiltonian in this fashion, it is clear that the system is spin-rotationally invariant. Furthermore, it can easily be shown that the number operator commutes with the Hamiltonian, $[n_{j\sigma}, H] = 0$. As a result, the z-component of the

spin will also commute with the Hamiltonian, $[S_j^z, H] = 0$, and S^z is conserved by the Hubbard model. By symmetry, there is no difference between S^x, S^y, and S^z, and the Hamiltonian actually commutes with all three terms. However, the three operators do not commute with each other,

$$[S^x, S^y] = iS^z\,, \qquad [S^z, S^x] = iS^y\,, \qquad [S^y, S^z] = iS^x\,, \tag{1.32}$$

and we generally choose a basis in terms of the z-component of the spin for convenience.

Next, let us examine the particle-hole symmetry of the Hubbard model. For the purposes of this discussion, we will use the form of the interaction term given in Eqn. (1.20) and a more general expression for the kinetic energy term than just nearest neighbor hopping to write the Hubbard Hamiltonian as

$$H = -\frac{1}{2}\sum_{j,l}\sum_{\sigma}(t_{jl}c_{j\sigma}^{\dagger}c_{l\sigma} + t_{jl}^{*}c_{l\sigma}^{\dagger}c_{j\sigma}) + U\sum_{j}\left(n_{j\uparrow} - \frac{1}{2}\right)\left(n_{j\downarrow} - \frac{1}{2}\right). \tag{1.33}$$

Let us transform an electron of spin σ into a hole of spin σ by $c_{j\sigma}^{\dagger} \to c_{j\sigma}$, $c_{j\sigma} \to c_{j\sigma}^{\dagger}$. The occupation numbers $n_{j\sigma} \to c_{j\sigma}c_{j\sigma}^{\dagger} = 1 - n_{j\sigma}$. The interaction term remains the same, as a factor of -1 appears in from both the spin-up and spin-down terms. The hopping term becomes

$$t_{jl}c_{j\sigma}^{\dagger}c_{l\sigma} + t_{jl}^{*}c_{l\sigma}^{\dagger}c_{j\sigma} \to -t_{jl}^{*}c_{j\sigma}^{\dagger}c_{l\sigma} - t_{jl}c_{l\sigma}^{\dagger}c_{j\sigma}\,, \tag{1.34}$$

which is completely different from what it was before. Thus, the Hubbard model does not generally show particle-hole symmetry. However, if the lattice is bipartite, meaning that it can be decomposed into two sublattices A and B such that the neighbors of A are in sublattice B, then the minus sign in Eq. (1.34) can be taken

care of with the transformation:

$$c_{j\sigma}^{\dagger} \to \eta_j c_{j\sigma} \qquad\qquad c_{j\sigma} \to \eta_j c_{j\sigma}^{\dagger} \tag{1.35}$$

where

$$\eta_j = \begin{cases} 1 & \text{if } j \in A \\ -1 & \text{if } j \in B\,. \end{cases} \tag{1.36}$$

Thus, for nearest neighbors $\eta_j \eta_\ell = -1$ and, as $t_{j\ell}$ is nonzero only for j, ℓ on separate sublattices, the hopping term reverts to its original form.

If we do the particle-hole transformation on only one spin species,

$$c_{j\uparrow} \to c_{j\uparrow} \qquad\qquad c_{j\downarrow} \to (-1)^j c_{j\downarrow}^{\dagger}\,, \tag{1.37}$$

then we get the following:

1. The hopping term is unchanged for the down-spin electron provided the lattice is bipartite.

2. The sign of the interaction changes: $U \to -U$.

3. The chemical potential becomes a magnetic field: $\mu \leftrightarrow B_z$.

4. Spin and charge correlation functions interchange

$$n_{j\uparrow} - n_{j\downarrow} \leftrightarrow n_{j\uparrow} + n_{j\downarrow}\,. \tag{1.38}$$

5. The + spin and − spin correlations (S^+ and S^-) become s-wave pairing corre-

lations

$$c^\dagger_{j\uparrow} c_{j\downarrow} \leftrightarrow c^\dagger_{j\uparrow} c^\dagger_{j\downarrow} \tag{1.39}$$

$$c^\dagger_{j\downarrow} c_{j\uparrow} \leftrightarrow c_{j\downarrow} c_{j\uparrow} \,. \tag{1.40}$$

Thus, we see that the half-filled ($\mu = 0$) Hubbard model becomes the half-filled negative U Hubbard model, where both charge density wave and superconducting order exist simultaneously because of the xyz symmetry of the positive U Hubbard model! Thus, the half-filled system is a supersolid [35], meaning that it is spatially ordered but also has the characteristics of a superfluid, i.e. there is no friction. Lastly, when we move away from half-filling, we find that the system is a superconductor [36].

1.3 Extended Fermion Hubbard Model

In the fermion Hubbard model, the interaction is heavily screened and charge ordering does not play a large role in determining the physics of the system. But what if this is important, as it is in charge transfer solids and in conducting polymers? There is no mechanism in the fermion Hubbard model to handle charge ordering, and we need to modify our treatment of the overlap integral [Eq. (1.11)] to include intersite interactions. The simplest treatment of intersite interactions is to include nearest-neighbor interactions V, which we shall refer to as the Extended Hubbard model,

$$H = -t \sum_{\langle i,j \rangle} \sum_{\sigma} \left(c^\dagger_{i\sigma} c_{j\sigma} + \text{h.c.} \right) + U \sum_i n_{i\uparrow} n_{i\downarrow} + V \sum_{\langle i,j \rangle} n_i n_j - \mu \sum_i n_i \,. \tag{1.41}$$

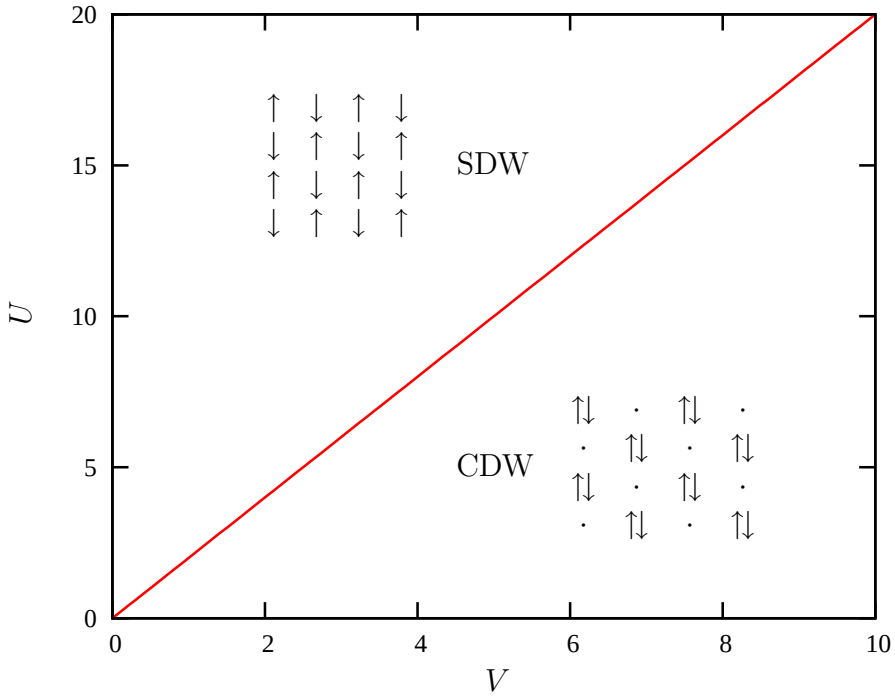

Figure 1.7: Phase diagram for the Extended Hubbard model in the strong-coupling limit $t = 0$ at half-filling. The boundary between the spin density wave and charge density wave phases lies on the line $U = 2V$. The transition is first-order.

1.3.1 Strong Coupling Limit

In the strong coupling limit $t = 0$, the phase diagram of the extended Hubbard model at zero temperature can be determined exactly. At half-filling, there are two possible ground states for the system: a charge density wave (CDW) or a spin density wave (SDW). The ordering vector for the SDW phase is $\mathbf{Q} = (\pi, \pi)$, although doping the system away from half-filling causes $\mathbf{Q}$ to change and increases the wavelength of the SDW phase. The ground state energies are

$$E_{\mathrm{CDW}} = \frac{1}{2}NU\,, \qquad\qquad E_{\mathrm{SDW}} = NV\,. \tag{1.42}$$

By equating these energies, we can determine the phase boundary to be $U = 2V$ (see Fig. 1.7). Strong coupling perturbation theory to second order in the hopping [37, 38]

yields the following:

$$E^{(2)}_{\mathrm{CDW}} = N\left[\frac{U}{2} + \frac{2t^2}{3V-U}\right] \tag{1.43}$$

$$E^{(2)}_{\mathrm{SDW}} = N\left[V + \frac{4t^2\ln 2}{U-V}\right] \tag{1.44}$$

We can determine how the phase boundary shifts by setting $U = 2V$ and looking at both energies. We find

$$E_{\mathrm{CDW}} = N\left[\frac{U}{2} + \frac{t^2}{U}\right] \tag{1.45}$$

$$E_{\mathrm{SDW}} = N\left[\frac{U}{2} - \frac{8t^2\ln 2}{U}\right]. \tag{1.46}$$

Thus, $E_{\mathrm{SDW}} < E_{\mathrm{CDW}}$ and the phase boundary in Fig. 1.7 is shifted down by the quantum fluctuations. In order to understand the reason for this, let us consider the entropy of each phase at $t = 0$. The degeneracy of the SDW phase is $\binom{N}{N/2}$ while the CDW phase is only doubly degenerate. As the hopping is turned on, the large degeneracy is lifted and lowers the energy more for the SDW phase.

1.3.2 Bond Ordered Wave Controversy

There is some controversy over the phase diagram of the Extended Hubbard Hamiltonian at weak-coupling. The original studies of this model with renormalization group found only SDW and CDW regions defined by a second-order transition at weak coupling that changes at a tricritical point to a first-order transition at strong coupling [37, 39, 40]. QMC simulations with the stochastic series expansion discovered something quite different at weak coupling, a bond order wave (BOW) phase that transitions to SDW via a Kosterlitz-Thouless and also to CDW by a second-order transition [41]. The BOW phase is distinguished by the kinetic energy alternating between two values as one moves through the lattice. A schematic drawing of the

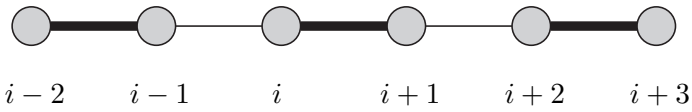

Figure 1.8: Illustration of a BOW phase. The thick lines indicate a high kinetic energy while the thin lines indicate a small kinetic energy.

phase in one dimension is shown in Fig. 1.8. To add to this controversy, density matrix renormalization group calculations [42–44] find that the BOW phase only exists precisely on the SDW-CDW transition line instead of over an extended region. In addition, the BOW phase began at finite, nonzero coupling (unlike the Stochastic Series Expansion (SSE) calculation which began at $U = V = 0$). At the time of this writing, it is clear that the BOW phase does exist in real materials, as the phase has been found experimentally in Rb-TCNQ(II) [45]. The exact details of the phase diagram of the extended Hubbard Hamiltonian, however, remain unclear.

1.4 Summary of the Main Results

In the decades following its proposal in the mid-1960's, the Hubbard model was extensively studied by approximate analytic techniques like the random phase approximation, renormalization group approaches, series expansions, and strong- and weak-coupling perturbation theories. Then, beginning in the mid-to-late 1980's, quantum Monte Carlo methods were developed and brought to bear. It is the application of these latter techniques to some new areas of Hubbard Hamiltonian physics that will be the topic of this thesis.

The remainder of this dissertation is organized in the following manner. In Chapter 2, the theoretical background of path integral quantum Monte Carlo is reviewed and both world-line quantum Monte Carlo (WLQMC) and determinant quantum Monte Carlo (DQMC) are discussed in detail. Then, in Chapter 3, I separately examine the impact of static and dynamic fluctuations on the one-dimensional extended

fermion Hubbard Hamiltonian. Next, Chapter 4 is a discussion of the visibility, a quantity central to optical lattice experiments, in the one-dimensional Bose-Fermi Hubbard Hamiltonian with a harmonic trap. Chapter 5 examines the single particle properties and magnetic correlations in the two-dimensional fermion Hubbard model. This chapter also introduces a computationally convenient definition of the structure factor that allows for a more accurate linear fit and extrapolation of the order parameter. Finally, in Chapter 6, I discuss some of the conclusions of my dissertation work and the open questions that remain to be studied, particularly the effect of adding an optical trap to the two-dimensional fermion Hubbard model. Chapters 3-5 are all based on published journal articles (See Refs. 25, 46 and 47).

1.5 References

[1] M. C. Gutzwiller, Effect of Correlation on the Ferromagnetism of Transition Metals, *Phys. Rev. Lett.* **10**, 159 (1963).

[2] J. Hubbard, Electron Correlations in Narrow Energy Bands, *Proc. Roy. Soc. London A* **276**, 238 (1963).

[3] J. Hubbard, Electron Correlations in Narrow Energy Bands. II. The Degenerate Band Case, *Proc. Roy. Soc. London A* **277**, 237 (1964).

[4] J. Hubbard, Electron Correlations in Narrow Energy Bands. III. An Improved Solution, *Proc. Roy. Soc. London A* **281**, 401 (1964).

[5] J. Hubbard, Electron Correlations in Narrow Energy Bands. IV. The Atomic Representation, *Proc. Roy. Soc. London A* **285**, 542 (1965).

[6] J. Kanamori, Electron Correlation and Ferromagnetism of Transition Metals, *Progress of Theoretical Physics* **30**, 275 (1963).

[7] A. Svane and O. Gunnarsson, Transition-metal oxides in the self-interaction˘corrected density-functional formalism, *Phys. Rev. Lett.* **65**, 1148 (1990).

[8] V. I. Anisimov, J. Zaanen, and O. K. Andersen, Band theory and Mott insulators: Hubbard U instead of Stoner I, *Phys. Rev. B* **44**, 943 (1991).

[9] A. I. Liechtenstein, V. I. Anisimov, and J. Zaanen, Density-functional theory and strong interactions: Orbital ordering in Mott-Hubbard insulators, *Phys. Rev. B* **52**, R5467 (1995).

[10] K. Held, V. I. Anisimov, I. A. Nekrasov, V. Eyert, G. Keller, T. Pruschke, D. Vollhardt, N. Blümer, A. K. McMahan, and R. T. Scalettar, The LDA+DMFT Approach to Materials with Strong Electronic Correlations, in *Quantum Simulations of Complex Many-Body Systems: From Theory to Algorithms*, vol. 10 of *NIC Series*, edited by J. Grotendorst, D. Marx, and A. Muramatsu, pp. 175–209 (John von Neumann Institute for Computing, 2002).

[11] K. Held, V. I. Anisimov, V. Eyert, G. Keller, A. K. McMahan, I. A. Nekrasov, and D. Vollhardt, *Advances in Solid State Physics*, vol. 43 of *Advances in Solid State Physics*, ch. 23, pp. 267–286 (Springer, 2003).

[12] N. F. Mott, Metal-Insulator Transition, *Rev. Mod. Phys.* **40**, 677 (1968).

[13] F. Gebhard (ed.), *The Mott Metal-Insulator Transition: Model and Methods* (Springer, New York, 1997).

[14] S. R. White, D. J. Scalapino, R. L. Sugar, E. Y. Loh, J. E. Gubernatis, and R. T. Scalettar, Numerical study of the two-dimensional Hubbard model, *Phys. Rev. B* **40**, 506 (1989).

[15] D. J. Scalapino, Does the Hubbard Model Have the Right Stuff, in *Proceedings of the International School of Physics, "Enrico Fermi"*, edited by R. A. Broglia and J. R. Schrieffer (1994), and references cited therein.

[16] T. A. Maier, M. Jarrell, T. C. Schulthess, P. R. C. Kent, and J. B. White, Systematic Study of *d*-Wave Superconductivity in the 2D Repulsive Hubbard Model, *Phys. Rev. Lett.* **95**, 237001 (2005).

[17] D. J. Scalapino, *Handbook of High Temperature Superconductivity*, ch. 13, pp. 495–526 (Springer, 2007).

[18] C. Chen, Electron correlation and heavy-fermion states in the Hubbard model, *Physica B: Condensed Matter* **206-207**, 729 (1995), proceedings of the International Conference on Strongly Correlated Electron Systems.

[19] B. DeMarco and D. S. Jin, Onset of Fermi Degeneracy in a Trapped Atomic Gas, *Science* **285**, 1703 (1999).

[20] A. G. Truscott, K. E. Strecker, W. I. McAlexander, G. B. Partridge, and R. G. Hulet, Observation of Fermi Pressure in a Gas of Trapped Atoms, *Science* **291**, 2570 (2001).

[21] K. M. O'Hara, S. L. Hemmer, M. E. Gehm, S. R. Granade, and J. E. Thomas, Observation of a Strongly Interacting Degenerate Fermi Gas of Atoms, *Science* **298**, 2179 (2002).

[22] M. Köhl, H. Moritz, T. Stöferle, K. Günter, and T. Esslinger, Fermionic Atoms in a Three Dimensional Optical Lattice: Observing Fermi Surfaces, Dynamics, and Interactions, *Phys. Rev. Lett.* **94**, 080403 (2005).

[23] M. Köhl and T. Esslinger, Fermionic atoms in an optical lattice: a new synthetic material, *Europhysics News* **37**, 18 (2006).

[24] R. Jordens, N. Strohmaier, K. Gunter, H. Moritz, and T. Esslinger, A Mott insulator of fermionic atoms in an optical lattice, *Nature* **455**, 204 (2008).

[25] C. N. Varney, C.-R. Lee, Z. J. Bai, S. Chiesa, M. Jarrell, and R. T. Scalettar, Quantum Monte Carlo study of the two-dimensional fermion Hubbard model, *Phys. Rev. B* **80**, 075116 (2009).

[26] N. W. Ashcroft and N. D. Mermin, *Solid State Physics* (Thomson Learning, 1976).

[27] C. Kittel, *Quantum Theory of Solids* (John Wiley and Sons, 1987).

[28] A. L. Fetter, *Quantum Theory of Many-Particle Systems* (Dover Publications, 2003).

[29] G. D. Mahan, *Many-Particle Physics*, Physics of Solids and Liquids (Springer, 2007), third edition.

[30] F. H. L. Essler, H. Frahm, F. Göhmann, A. Klümper, and V. E. Korepin, *The One-Dimensional Hubbard Model* (Cambridge University Press, 2005).

[31] P. Fazekas, *Lecture Notes on Electron Correlation and Magnetism* (World Scientific, Singapore, 1999).

[32] C. Cohen-Tannoudji, B. Diu, and F. Laloe, *Quantum Mechanics* (Wiley-Interscience, 2006).

[33] J. E. Hirsch, Metallic ferromagnetism in a single-band model. II. Finite-temperature magnetic properties, *Phys. Rev. B* **40**, 9061 (1989).

[34] A. Auerbach, *Interacting Electrons and Quantum Magnetism*, Graduate Texts in Contemporary Physics (Springer, 1994).

[35] R. T. Scalettar, E. Y. Loh, J. E. Gubernatis, A. Moreo, S. R. White, D. J. Scalapino, R. L. Sugar, and E. Dagotto, Phase diagram of the two-dimensional negative-U Hubbard model, *Phys. Rev. Lett.* **62**, 1407 (1989).

[36] A. Moreo and D. J. Scalapino, Two-dimensional negative-U Hubbard model, *Phys. Rev. Lett.* **66**, 946 (1991).

[37] J. E. Hirsch, Charge-Density-Wave to Spin-Density-Wave Transition in the Extended Hubbard Model, *Phys. Rev. Lett.* **53**, 2327 (1984).

[38] P. G. J. van Dongen, The Extended Hubbard Model at Large Interaction, in *The Hubbard Model: Its Physics and Mathematical Physics*, vol. 345 of *NATO Series B*, edited by D. Baeriswyl, D. K. Campbell, J. M. P. Carmelo, F. Guinea, and E. Louis (Plenum Press, 1993).

[39] J. E. Hirsch, Phase diagram of the one-dimensional molecular-crystal model with Coulomb interactions: Half-filled-band sector, *Phys. Rev. B* **31**, 6022 (1985).

[40] J. W. Cannon and E. Fradkin, Phase diagram of the extended Hubbard model in one spatial dimension, *Phys. Rev. B* **41**, 9435 (1990).

[41] P. Sengupta, A. W. Sandvik, and D. K. Campbell, Bond-order-wave phase and quantum phase transitions in the one-dimensional extended Hubbard model, *Phys. Rev. B* **65**, 155113 (2002).

[42] E. Jeckelmann, Ground-State Phase Diagram of a Half-Filled One-Dimensional Extended Hubbard Model, *Phys. Rev. Lett.* **89**, 236401 (2002).

[43] A. W. Sandvik, P. Sengupta, and D. K. Campbell, Comment on "Ground-State Phase Diagram of a Half-Filled One-Dimensional Extended Hubbard Model", *Phys. Rev. Lett.* **91**, 089701 (2003).

[44] E. Jeckelmann, Jeckelmann Replies:, *Phys. Rev. Lett.* **91**, 089702 (2003).

[45] T. McQueen, D. Ho, C. J. Cahua, R. Cava, R. P. Jr, and Z. Soos, Realization of the bond order wave (BOW) phase of extended Hubbard models in Rb-TCNQ(II), *Chemical Physics Letters* **475**, 44 (2009).

[46] H. A. Craig, C. N. Varney, W. E. Pickett, and R. T. Scalettar, Static versus dynamic fluctuations in the one-dimensional extended Hubbard model, *Phys. Rev. B* **76**, 125103 (2007).

[47] C. N. Varney, V. G. Rousseau, and R. T. Scalettar, Quantum Monte Carlo study of the visibility of one-dimensional Bose-Fermi mixtures, *Phys. Rev. A* **77**, 041608(R) (2008).

Chapter 2

Path Integral Quantum Monte Carlo for Lattice Fermions

2.1 Introduction

In this chapter, I will review two quantum Monte Carlo (QMC) methods for lattice fermions, the world-line [1] and determinantal [2] algorithms. It is assumed that the reader have a firm grasp of statistical mechanics [3–5] and classical Monte Carlo techniques (See Ref. 6, Chapter 1 of Ref. 7, and Chapter 2 of Ref. 8).

Let us consider a Hubbard Hamiltonian with particle-hole symmetry:

$$\begin{aligned} H &= K + V \,, \\ K &= -t \sum_{\langle i,j \rangle} \left(c^\dagger_{i\sigma} c_{j\sigma} + c^\dagger_{j\sigma} c_{i\sigma} \right) - \mu \sum_{i,\sigma} n_{i\sigma} \,, \\ V &= U \sum_i \left(n_{i\uparrow} - \frac{1}{2} \right) \left(n_{i\downarrow} - \frac{1}{2} \right) \,. \end{aligned} \tag{2.1}$$

Here $c^\dagger_{j\sigma}$ ($c_{j\sigma}$) are creation (annihilation) operators for a fermion of spin σ on site j and number operator $n_j = c^\dagger_{j\sigma} c_{j\sigma}$.

Both algorithms originate from the Feynman path-integral representation of the

quantum fields [9]. The partition function $\mathcal{Z}$ and the average value of a physical observable A are

$$\mathcal{Z} = \mathrm{Tr}(e^{-\beta H}) \,, \tag{2.2}$$

$$A = \mathcal{Z}^{-1}\mathrm{Tr}(Ae^{-\beta H}) \,, \tag{2.3}$$

where $\beta = 1/kT$ is the inverse temperature. In order to evaluate the trace, we must break up the imaginary-time interval $0 \leq \tau \leq \beta$ into L subintervals of width $\Delta\tau = \beta/L$ (note that in Chapter 3 we use ϵ in place of $\Delta\tau$ to avoid confusion with another variable) and utilize the Suzuki-Trotter decomposition [10, 11]

$$\mathcal{Z} = \mathrm{Tr}\left[e^{-\beta H}\right] = \mathrm{Tr}\left[\lim_{\Delta\tau\to 0}\left(e^{-\Delta\tau K}e^{-\Delta\tau V}\right)^{L}\right] \tag{2.4}$$

to split up the kinetic and interaction terms. This Suzuki-Trotter approximation introduces errors in measurements [12, 13],

$$e^{-\Delta\tau H} = e^{-\Delta\tau K}e^{-\Delta\tau V}\left\{1 + (\Delta\tau^2)[K,V]\right\} \,, \tag{2.5}$$

which are commonly referred to as "Trotter" errors. Thus, for a Hamiltonian in which K and V commute, the Suzuki-Trotter decomposition is exact. For the Hubbard Hamiltonian, this is not the case and in order to minimize the Trotter error we must keep the quantity $Ut(\Delta\tau)^2$ small (typically less than $1/8$ is considered acceptable). Although we follow the prescription outlined above, there are many ways to reduce the error by using different Suzuki-Trotter decompositions [14].

There are two different prescriptions for evaluating the traces in Eqns. (2.2) and (2.3). The first method, world-line quantum Monte Carlo (WLQMC), introduces a complete set of states at each time slice and the sums are carried out by importance sampling techniques. The second method employs an auxiliary bosonic field to in-

tegrate out the fermionic fields and is known as determinant quantum Monte Carlo (DQMC). In the sections that follow, I will discuss the details of both algorithms and a major difficulty of QMC simulations of fermions known as the sign problem.

2.2 World-Line Quantum Monte Carlo

World-line quantum Monte Carlo (WLQMC) was developed for Hubbard models by Hirsch, Sugar, Scalapino and Blankenbecler in 1982 [1]. The path integral in Eq. (2.4) is treated by inserting complete sets of fermion occupation number states $I = \sum |n_{j,\ell,\sigma}\rangle \langle n_{j,\ell,\sigma}|$ for both the trace and at all imaginary-times. Here, j is the site index, ℓ is the index for the time slice, σ is the spin. This yields

$$\begin{aligned} \mathcal{Z} =& \mathrm{Tr}\left[e^{-\beta H}\right] = \mathrm{Tr}\left[\lim_{\Delta\tau\to 0}\left(e^{-\Delta\tau K}e^{-\Delta\tau V}\right)^{L}\right] \\ \mathcal{Z} =& \sum_{i_1,\ldots,i_L} \left\langle i_1 \middle| e^{-\Delta\tau K}e^{-\Delta\tau V} \middle| i_L \right\rangle \left\langle i_L \middle| e^{-\Delta\tau K}e^{-\Delta\tau V} \middle| i_{L-1} \right\rangle \cdots \\ & \times \left\langle i_2 \middle| e^{-\Delta\tau K}e^{-\Delta\tau V} \middle| i_1 \right\rangle \end{aligned} \tag{2.6}$$

where the state $|i_\ell\rangle$ is the occupation number state at time slice ℓ,

$$|i_\ell\rangle = |n_{1,\ell,\uparrow} n_{2,\ell,\uparrow} \cdots n_{N,\ell,\uparrow} n_{1,\ell,\downarrow} n_{2,\ell,\downarrow} \cdots n_{1,\ell,\downarrow}\rangle \ . \tag{2.7}$$

The matrix elements in Eq. 2.6 are easily determined when we notice that the Hamiltonian is factorizable: it consists of independent two-site pieces. This is achieved by subdividing the kinetic energy K into K_{odd} and K_{even} via the "checkerboard decom-

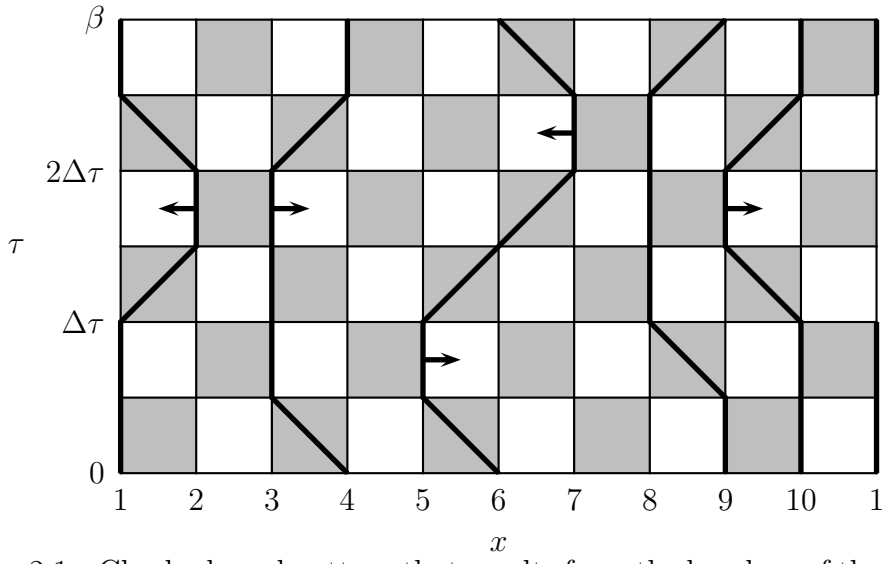

Figure 2.1: Checkerboard pattern that results from the breakup of the time-evolution operator. World-lines can only traverse diagonals of shaded squares. The bolded lines are examples of allowed fermion world-lines, and the arrows indicate a typical Monte Carlo move that pulls a world-line across an unshaded square. Periodic boundary conditions connect sites and imaginary-time slices at the edges of the lattice.

position" [1]

$$K = K_{\text{odd}} + K_{\text{even}} \tag{2.8a}$$

$$K_{\text{odd}} = -t \sum_{i \text{ odd}} \sum_{\sigma} (c^{\dagger}_{i+1,\sigma} c_{i,\sigma} + c^{\dagger}_{i,\sigma} c_{i+1,\sigma}) \,, \tag{2.8b}$$

$$K_{\text{even}} = -t \sum_{i \text{ even}} \sum_{\sigma} (c^{\dagger}_{i+1,\sigma} c_{i,\sigma} + c^{\dagger}_{i,\sigma} c_{i+1,\sigma}) \,. \tag{2.8c}$$

This allows us to write the matrix elements of the trace as

$$\begin{aligned}
\left\langle 00 \left| e^{t\Delta\tau(c^{\dagger}_i c_{i+1} + c^{\dagger}_{i+1} c_i)} e^{-\Delta\tau U\left(n_{i,\uparrow} - 1/2\right)\left(n_{i,\uparrow} - 1/2\right)} \right| 00 \right\rangle &= e^{-\Delta\tau U/4} \,, \\
\left\langle 11 \left| e^{t\Delta\tau(c^{\dagger}_i c_{i+1} + c^{\dagger}_{i+1} c_i)} e^{-\Delta\tau U\left(n_{i,\uparrow} - 1/2\right)\left(n_{i,\uparrow} - 1/2\right)} \right| 11 \right\rangle &= e^{-\Delta\tau U/4} \,, \\
\left\langle 10 \left| e^{t\Delta\tau(c^{\dagger}_i c_{i+1} + c^{\dagger}_{i+1} c_i)} e^{-\Delta\tau U\left(n_{i,\uparrow} - 1/2\right)\left(n_{i,\uparrow} - 1/2\right)} \right| 10 \right\rangle &= \cosh(t\Delta\tau) e^{\Delta\tau U/4} \,, \\
\left\langle 10 \left| e^{t\Delta\tau(c^{\dagger}_i c_{i+1} + c^{\dagger}_{i+1} c_i)} e^{-\Delta\tau U\left(n_{i,\uparrow} - 1/2\right)\left(n_{i,\uparrow} - 1/2\right)} \right| 01 \right\rangle &= \sinh(t\Delta\tau) e^{\Delta\tau U/4} \,.
\end{aligned} \tag{2.9}$$

The allowed moves in the WLQMC algorithm can be visualized simply. In Fig. 2.1, the checkerboard pattern in space and imaginary-time is shown with several allowed

fermion world-lines. If a fermion hops from one site to another, the world-line can only move through the diagonal of a shaded square. It cannot traverse the diagonal of an unshaded square.

When $U = 0$, there is a very simple interpretation of the weights in Eq. (2.9) [1]. A single fermion hops one site to the left or the right or moves forward in imaginary-time with matrix element $\sinh(t\Delta\tau)$ and $\cosh(t\Delta\tau)$, respectively. This explains the elements $\langle 10|\ldots|10\rangle = \cosh(t\Delta\tau)$ and $\langle 10|\ldots|01\rangle = \sinh(t\Delta\tau)$. Two fermions can interchange by hopping past each other with matrix element $-\sinh^2(t\Delta\tau)$. Lastly, two fermions on adjacent sites can move forward in imaginary-time with matrix element $\cosh^2(t\Delta\tau)$. The combination of these processes, along with the identity $\cosh^2 - \sinh^2 = 1$, yields $\langle 11|\ldots|11\rangle = 1$.

The WLQMC algorithm has been modified beyond the simple local update method described here. Of particular note are the loop algorithm [15], the continuous time versions of the local update algorithm [16] and the loop algorithm [17], and the worm algorithm [18]. While not discussed here, these developments and the local update algorithm of this section are reviewed in Refs. 8 and 19–24.

2.3 Determinant Quantum Monte Carlo

2.3.1 Multidimensional Gaussian Integrals

Determinant quantum Monte Carlo (DQMC) shares many similarities with multidimensional Gaussian integrals. Let us recall the one-dimensional Gaussian integral,

$$\int_{-\infty}^{\infty} dx\, e^{-ax^2} = \sqrt{\frac{\pi}{a}}\,. \tag{2.10}$$

Generalizing this formula to many dimensions, we find

$$\mathcal{Z} = \int_{-\infty}^{\infty} \cdots \int_{-\infty}^{\infty} dx_1 dx_2 \ldots dx_N \, e^{-\mathbf{x}\cdot\mathsf{A}\cdot\mathbf{x}^T} = \frac{\pi^{n/2}}{\sqrt{\det \mathsf{A}}}\,, \tag{2.11}$$

which we recall is the form of the partition function for a set of classical variables whose action is given by $\mathbf{x}\cdot\mathsf{A}\cdot\mathbf{x}^T$ [4]. When the integrand includes factors of x_i, as it would for an expectation value in statistical mechanics, the integral becomes

$$\langle x_i x_j \rangle = \mathcal{Z}^{-1} \int_{-\infty}^{\infty} \cdots \int_{-\infty}^{\infty} dx_1 dx_2 \ldots dx_N \, x_i x_j e^{-\mathbf{x}\cdot\mathsf{A}\cdot\mathbf{x}^T} = \frac{1}{2}\left[\mathsf{A}^{-1}\right]_{ij}\,. \tag{2.12}$$

Adding additional factors of x_i to the integrand yields,

$$\begin{aligned}\langle x_i x_j x_k x_l \rangle &= \mathcal{Z}^{-1} \int_{-\infty}^{\infty} \cdots \int_{-\infty}^{\infty} dx_1 dx_2 \ldots dx_N \, x_i x_j x_k x_l e^{-\mathbf{x}\cdot\mathsf{A}\cdot\mathbf{x}^T} \\ &= \frac{1}{4}\left(\left[\mathsf{A}^{-1}\right]_{ij}\left[\mathsf{A}^{-1}\right]_{kl} + \left[\mathsf{A}^{-1}\right]_{ik}\left[\mathsf{A}^{-1}\right]_{jl} + \left[\mathsf{A}^{-1}\right]_{il}\left[\mathsf{A}^{-1}\right]_{jk}\right)\,,\end{aligned} \tag{2.13}$$

which is similar in form to "Wick's Theorem." This theorem tells us that contractions of products of many fermion operators can be expressed as a sum of products of contractions, where the contractions are taken two operators at a time and the sum is over all possible permutations [25].

In Sec. 2.3.2, we will see that these quantities are directly related to the Hubbard-Stratonovich transformation [26] and the formulas for the partition function and Green's function.

2.3.2 Formalism

The determinant quantum Monte Carlo algorithm was developed by Blankenbecler, Scalapino, and Sugar (BSS) [2]. Like world-line quantum Monte Carlo, it is based on Feynman's path integral formulation of statistical mechanics and utilizes the Trotter discretization of β to arrive at Eq. (2.4). The trace can be done if the Hamiltonian

in Eq. (2.1) is quadratic in terms of the fermion operators

$$H = \sum_{ij} c_i^\dagger \, \mathsf{h}_{ij} \, c_j \, . \tag{2.14}$$

Here h is an $N \times N$ matrix. The kinetic energy K is already in the correct form, but V is quartic in fermion operators. To handle this term, we employ the discrete Hubbard-Stratonovich transformation [26],

$$e^{-U\Delta\tau\left(n_{i\uparrow}-\frac{1}{2}\right)\left(n_{i\downarrow}-\frac{1}{2}\right)} = \frac{1}{2} e^{-U\Delta\tau/4} \sum_{s_i=\pm 1} e^{\lambda s_i \left(n_{i\uparrow}-n_{i\downarrow}\right)} \tag{2.15}$$

where $\cosh\lambda = e^{U\Delta\tau/2}$ and s_i is an Ising variable referred to as the Hubbard-Stratonovich (HS) field. Other ways of reducing the Hamiltonian have been developed [27–29] and the effects of different transformations are briefly discussed in Section 2.4.

Now that we can write the Hamiltonian in quadratic form, we can evaluate the trace in the path integral with the identity

$$\mathcal{Z} = \mathrm{Tr}\left[e^{-\beta H}\right] = \det\left[\mathsf{I} + e^{-\beta \mathsf{h}}\right] \, , \tag{2.16}$$

where I is an $N \times N$ identity matrix. More generally, as we have discretized β via the Suzuki-Trotter decomposition, we have a set of quadratic Hamiltonians (one for each time slice). The Hubbard-Stratonovich transformation is applied at every time slice, and the Hubbard-Stratonovich field $s_i(\ell)$ has two indices, space i and imaginary-time ℓ. The set of Hamiltonians is therefore defined as

$$H(\ell) = \sum_{ij} c_i^\dagger \, \mathsf{h}_{ij}(\ell) \, c_j \, , \tag{2.17}$$

and the resultant identity for the partition function is

$$\begin{aligned} \mathcal{Z} &= \mathrm{Tr}\left[e^{-\Delta\tau H(L)}e^{-\Delta\tau H(L-1)}\cdots e^{-\Delta\tau H(1)}\right] \\ &= \det\left[\mathsf{I} + e^{-\Delta\tau \mathsf{h}(L)}e^{-\Delta\tau \mathsf{h}(L-1)}\cdots e^{-\Delta\tau \mathsf{h}(1)}\right] . \end{aligned} \tag{2.18}$$

The partition function becomes

$$\mathcal{Z} = \sum_{\{s_i(\ell)\}}\prod_{\sigma}\det \mathsf{M}^{\sigma} , \tag{2.19}$$

with

$$\mathsf{M}^{\sigma} = \mathsf{I} + \mathsf{B}^{\sigma}_{L}\mathsf{B}^{\sigma}_{L-1}\cdots\mathsf{B}^{\sigma}_{1} , \tag{2.20}$$

and

$$\mathsf{B}^{\sigma}_{\ell} = e^{-\Delta\tau\mathsf{k}}e^{-\Delta\tau\mathsf{v}^{\sigma}(\ell)} . \tag{2.21}$$

Here k is an $N\times N$ matrix defined by

$$\mathsf{k}_{ij} = \begin{cases} -t & \text{if } i \text{ and } j \text{ are nearest neighbors,} \\ -\mu & \text{along the diagonal,} \\ 0 & \text{otherwise,} \end{cases} \tag{2.22}$$

and $\mathsf{v}^{\sigma}(\ell)$ is a diagonal $N\times N$ matrix where the ii-th element is

$$\mathsf{v}^{\sigma}_{ii}(\ell) = \lambda\sigma s_i(\ell) . \tag{2.23}$$

The quantum partition function has now been expressed as a classical Monte Carlo problem for an Ising field in $d+1$ dimensions. The most naive approach to the

simulation would involve flipping a HS spin, evaluating the "Boltzmann weight," and accepting with the Metropolis algorithm. If we let $\{s'\}$ and $\{s\}$ be two sets of HS configurations such that all of the Ising spins are the same except for the ones on site i and imaginary-time slice ℓ, then the ratio of the "Boltzmann weights" is

$$R = \frac{P(\{s'\})}{P(\{s\})} = \prod_{\sigma} R_{\sigma} \,, \tag{2.24}$$

where the ratio of fermion determinants is

$$R_{\sigma} = \frac{\det \mathsf{M}^{\sigma}(\{s'\})}{\det \mathsf{M}^{\sigma}(\{s\})} \,. \tag{2.25}$$

The cpu time for each move would be $\mathcal{O}(N^3)$. Thus, updating all of the HS fields would require a cpu time of $\mathcal{O}(N^4)$. Fortunately, a clever approach can reduce this scaling to $\mathcal{O}(N^3)$. If a single spin is flipped on site i and time slice ℓ, the ii-th element of the matrices $\mathsf{v}^{\uparrow}(\ell)$ and $\mathsf{v}^{\downarrow}(\ell)$ change, affecting $\mathsf{B}_{\ell}^{\uparrow}$ and $\mathsf{B}_{\ell}^{\downarrow}$, respectively. The HS field $s_i(\ell) \to -s_i(\ell)$, and the change in the matrix element $\mathsf{v}_{ij}^{\sigma}(\ell)$ is

$$\delta \mathsf{v}_{ij}^{\sigma}(\ell) = \mathsf{v}_{ij}^{\sigma}(\ell, -s) - \mathsf{v}_{ij}^{\sigma}(\ell, s) = -2\lambda\sigma s_i(\ell)\delta_{ij} \,. \tag{2.26}$$

The change in the matrix $\mathsf{B}_{\ell}^{\sigma} \to [\mathsf{B}_{\ell}^{\sigma}]'$ can be written as a matrix product,

$$[\mathsf{B}_{\ell}^{\sigma}]' = \mathsf{B}_{\ell}^{\sigma} \Delta_{\ell}^{\sigma}(i) \,, \tag{2.27}$$

where the elements of the matrix $\Delta_{\ell}^{\sigma}(i)$ are

$$[\Delta_{\ell}^{\sigma}(i)]_{jk} = \begin{cases} 0 & \text{if } j \neq k \,, \\ 1 & \text{if } j = k \neq i \,, \\ e^{-2\lambda\sigma s_i(\ell)} & \text{if } j = k = i \,. \end{cases} \tag{2.28}$$

In order to write the ratio of the fermion determinants, we require the Green's function, which plays an important role in the DQMC algorithm. The equal-time Green's function is defined as

$$[G_\sigma]_{ij} \equiv \left\langle c_{i\sigma} c_{j\sigma}^\dagger \right\rangle = \mathcal{Z}^{-1} \mathrm{Tr} \left[c_{i\sigma} c_{j\sigma}^\dagger e^{-\Delta\tau h(L)} e^{-\Delta\tau h(L-1)} \cdots e^{-\Delta\tau h(1)} \right] . \tag{2.29}$$

In analogy with the relationship in Eq. (2.12), we find that the equal-time Green's function matrix can be written as

$$[\mathsf{G}^\sigma]_{ij} = [\mathsf{M}^\sigma]_{ij}^{-1} . \tag{2.30}$$

The Green's function matrix at the ℓ-th time slice is defined as

$$[\mathsf{G}_\ell^\sigma]_{ij} \equiv \left\langle c_{i\sigma}(\ell) c_{j\sigma}^\dagger(0) \right\rangle = [\mathsf{I} + \mathsf{A}_\ell^\sigma]_{ij}^{-1} , \tag{2.31}$$

where

$$A_\ell^\sigma \equiv \mathsf{B}_{\ell-1}^\sigma \mathsf{B}_{\ell-2}^\sigma \cdots \mathsf{B}_1^\sigma \mathsf{B}_L^\sigma \cdots \mathsf{B}_\ell^\sigma . \tag{2.32}$$

Using Eq. (2.31) and the cyclic properties of the determinant, we can rewrite the ratio of the fermion determinants as

$$\begin{aligned} R = \frac{\det[\mathsf{1} + \mathsf{A}_\ell^\sigma \Delta_\ell^\sigma(i)]}{\det[1 + \mathsf{A}_\ell^\sigma]} &= \det\left[(1 + \mathsf{A}_\ell^\sigma \Delta_\ell^\sigma(i))\, \mathsf{G}_\ell^\sigma \right] \\ = \det\left[1 + (1 - \mathsf{G}_\ell^\sigma)\, (\Delta_\ell^\sigma(i) - 1) \right] &= 1 + (1 - [\mathsf{G}_\ell^\sigma]_{ii}) \left(e^{-2\lambda\sigma s_i(\ell)} - 1 \right) , \end{aligned} \tag{2.33}$$

which is a rank-1 update that depends only on the HS field and the Green's function. The Green's function can be updated in two ways: from scratch by Eq. (2.31) or by iterating the "old" Green's function, referred to as "wrapping." One can show that

the Green's function at time slice $\ell + 1$ can be written as

$$\mathsf{G}^{\sigma}_{\ell+1} = \mathsf{B}^{\sigma}_{\ell} \mathsf{G}^{\sigma}_{\ell} \left[\mathsf{B}^{\sigma}_{\ell}\right]^{-1} . \tag{2.34}$$

Computing the Green's function from scratch requires $\mathcal{O}(N^4 L)$ operations. "Wrapping" the Green's function reduces the computational complexity by a factor of 2 or 3. In all, the rank-1 update for the determinant ratio in conjunction with "wrapping" the Green's function reduces the computational complexity by an order of magnitude in N, although it is important to note that "wrapping" is not numerically stable as round-off errors propogate rapidly when performing matrix inversions and multiplications. In practice, we find that it is necessary to recompute the Green's function from scratch after "wrapping" about 10 times.

From the Green's function matrix, we can determine a number of quantities. The density of electrons of spin σ on a given site i is

$$\langle n_{i\sigma} \rangle = \langle c^{\dagger}_{i\sigma} c_{i\sigma} \rangle = 1 - \langle c_{i\sigma} c^{\dagger}_{i\sigma} \rangle = 1 - \left[\mathsf{G}^{\sigma}\right]_{ii} . \tag{2.35}$$

The double occupancy and local moment are

$$\langle n_{i\uparrow} n_{i\downarrow} \rangle = \left(1 - \left[\mathsf{G}^{\uparrow}\right]_{ii}\right) \left(1 - \left[\mathsf{G}^{\downarrow}\right]_{ii}\right) , \tag{2.36}$$

$$\left\langle m^2 \right\rangle = \left\langle (n_{i\uparrow} - n_{i\downarrow})^2 \right\rangle = \left[\mathsf{G}^{\uparrow}\right]_{ii} + \left[\mathsf{G}^{\downarrow}\right]_{ii} - 2 \left[\mathsf{G}^{\uparrow}\right]_{ii} \left[\mathsf{G}^{\downarrow}\right]_{ii} , \tag{2.37}$$

respectively. We can examine the magnetic, charge, superconducting order by looking at correlation functions of the form:

$$c(\ell) = \left\langle \mathcal{O}_{i+\ell} \mathcal{O}^{\dagger}_{i} \right\rangle - \left\langle \mathcal{O}_{i+\ell} \right\rangle \left\langle \mathcal{O}^{\dagger}_{i} \right\rangle , \tag{2.38}$$

where for spin order in the xx direction, spin order in the zz direction, charge order,

and superconductivity we have

$$\mathcal{O}_i^{\text{xx spin}} = c_{i\downarrow}^\dagger c_{i\uparrow}\,, \tag{2.39a}$$

$$\mathcal{O}_i^{\text{zz spin}} = n_{i\uparrow} - n_{i\downarrow}\,, \tag{2.39b}$$

$$\mathcal{O}_i^{\text{charge}} = n_{i\uparrow} + n_{i\downarrow}\,, \tag{2.39c}$$

$$\mathcal{O}_i^{\text{pair}} = c_{i\downarrow} c_{i\uparrow}\,. \tag{2.39d}$$

The correlation functions are evaluated through the use of "Wick's Theorem" [25], which allows us to express these measurements in terms of the Green's function. For example, the spin-spin correlation function in the xx direction is

$$\begin{aligned} c_{\text{xx spin}}(\ell) &= \left\langle c_{i+\ell,\downarrow}^\dagger c_{i+\ell,\uparrow} c_{i,\uparrow}^\dagger c_{i,\downarrow} \right\rangle - \left\langle c_{i+\ell,\downarrow}^\dagger c_{i+\ell,\uparrow} \right\rangle \left\langle c_{i,\uparrow}^\dagger c_{i,\downarrow} \right\rangle \\ &= \left[\mathsf{G}^\uparrow\right]_{i+\ell,i} \left(\delta_{\ell,0} - \left[\mathsf{G}^\downarrow\right]_{i,i+\ell}\right)\,. \end{aligned} \tag{2.40}$$

The DQMC algorithm has been heavily studied since its inception in 1981. There are many aspects of the technique which are not discussed here, as they have already been reviewed in Refs. 7, 22–24 and 30. I will, however, discuss two ways in which the algorithm can be improved, and also, in Sec. 2.4, a major difficulty in QMC simulations.

As with any Monte Carlo technique, one is always interested in ways reduce the computational time and improve the ergodicity of the algorithm. Perhaps the simplest improvement one can make is to incorporate modern BLAS/LAPACK numerical kernels, which can handle matrix multiplication, inversion, and determinant calculation efficiently. In practice, the use of BLAS/LAPACK reduces computational time by a factor of 2 to 3. The computational complexity can be also reduced by introducing "delayed updating" of the Green's functions [31, 32]. In the algorithm described in this Section, every time a HS field is flipped, the $N \times N$ Green's function matrix at this position must be updated. Because only the determinant ratio R and a diagonal

entry of G_ℓ are required to accept or reject a Monte Carlo move, it is possible to delay multiple rank-1 updates and perform a rank-k update, where k is the number of Monte Carlo moves performed between updates. This results in reducing the computational effort to calculate the transition probability R for the delayed algorithm from N^2L^2 to kNL.

At large interaction strength, the algorithm described above experiences well-known problems with ergodicity. One manifestation of this difficulty results in a breaking of the spin-flip symmetry $\langle n_\uparrow \rangle \neq \langle n_\downarrow \rangle$. Furthermore, we note that the values of these quantities will precisely equal i/N, where i is an integer and N is the lattice size. One way of overcoming this problem with ergodicity is by introducing global moves [33]. Instead of flipping the Hubbard-Stratonovich field for one spatial site and one imaginary-time slice, we instead flip the fields for all imaginary-time slices on a given site. This move has the effect of transforming $n_{i,\sigma}$ to $n_{i,-\sigma}$. A global move of this sort requires a recalculation of the fermion determinant before and after the move. The improved ergodicity comes with a cost: the orthogonalization necessary to ensure stability during recomputation of the determinant has components that scale as N^2L^2 as well as N^3.

2.4 Sign Problem

The expectation value of a physical observable A is of the general form

$$\langle A \rangle = \frac{\sum_{\{x\}} w(x) A(x)}{\sum_{\{x'\}} w(x')}, \tag{2.41}$$

where $\sum_{\{x\}}$ is a sum over discrete spin variables. In the grand canonical ensemble, $w(x)$ is proportional to the fermion determinants for the spin-up and spin-down electrons

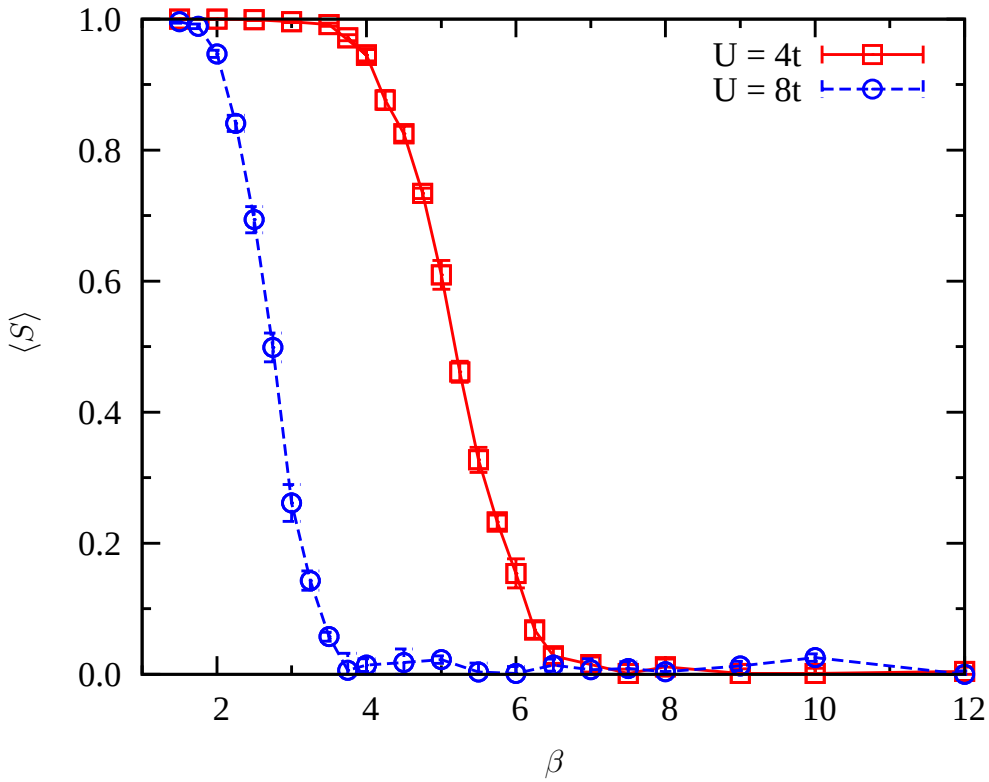

Figure 2.2: Average sign $\langle S \rangle$ vs. β on a 10×10 lattice for $U = 4t$ and $8t$. The chemical potentials are $\mu = -t$ and $-3t$, respectively, leading to fillings $\langle n \rangle \sim 0.83$ and 0.75. $\langle S \rangle = 1$ for high temperatures before it exponentially approaches 0.

[2]. As long as $w(x)$ is positive semidefinite, then Eq. (2.41) can be evaluated by importance-sampling techniques, where a sequence of configurations $\{x\}$ is generated with a probability distribution

$$P(x) = \frac{w(x)}{\sum_{\{x'\}} w(x')} \,. \tag{2.42}$$

Unfortunately, for simulations of fermions there are only a small number of cases in which $w(x)$ is positive semidefinite. One such example is the negative-U Hubbard model. Another example of larger interest to the remainder of this dissertation is the half-filled Hubbard model with a repulsive Coulomb interaction. When we dope this model away from half-filling, $w(x)$ is not positive semidefinite, and we can write the

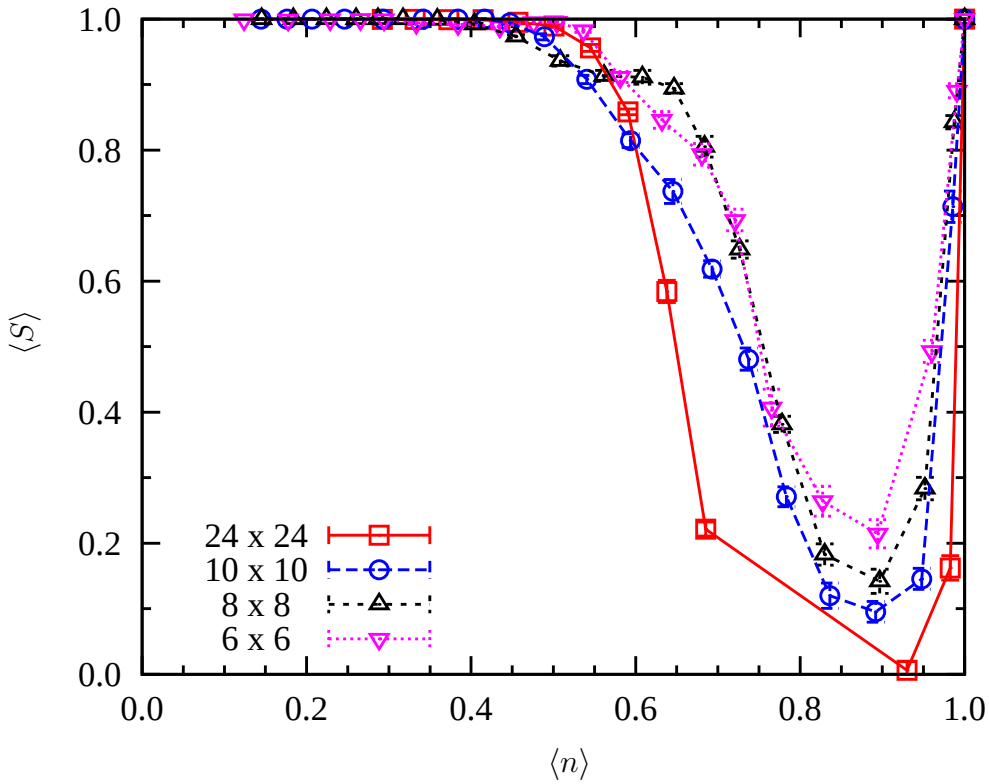

Figure 2.3: Average sign $\langle S \rangle$ vs. $\langle n \rangle$ for various lattice sizes at $U = 4t$ and $\beta t = 6$. The sign problem is the worst for fillings $0.65 \leq \langle n \rangle \leq 0.95$. Also, $\langle S \rangle$ depends weakly on the lattice size, with the largest lattices experiencing the smallest $\langle S \rangle$.

weight $w(x)$ as

$$w(x) = |w(x)|S(x)\,. \tag{2.43}$$

Here $S(x) = \pm 1$. We can define a new probability distribution,

$$\bar{P}(x) = \frac{|w(x)|}{\sum_{\{x'\}} |w(x')|}\,, \tag{2.44}$$

allowing us to rewrite Eq. (2.41) as [34]

$$\langle A \rangle = \frac{\langle AS \rangle_{\bar{P}}}{\langle S \rangle_{\bar{P}}}\,, \tag{2.45}$$

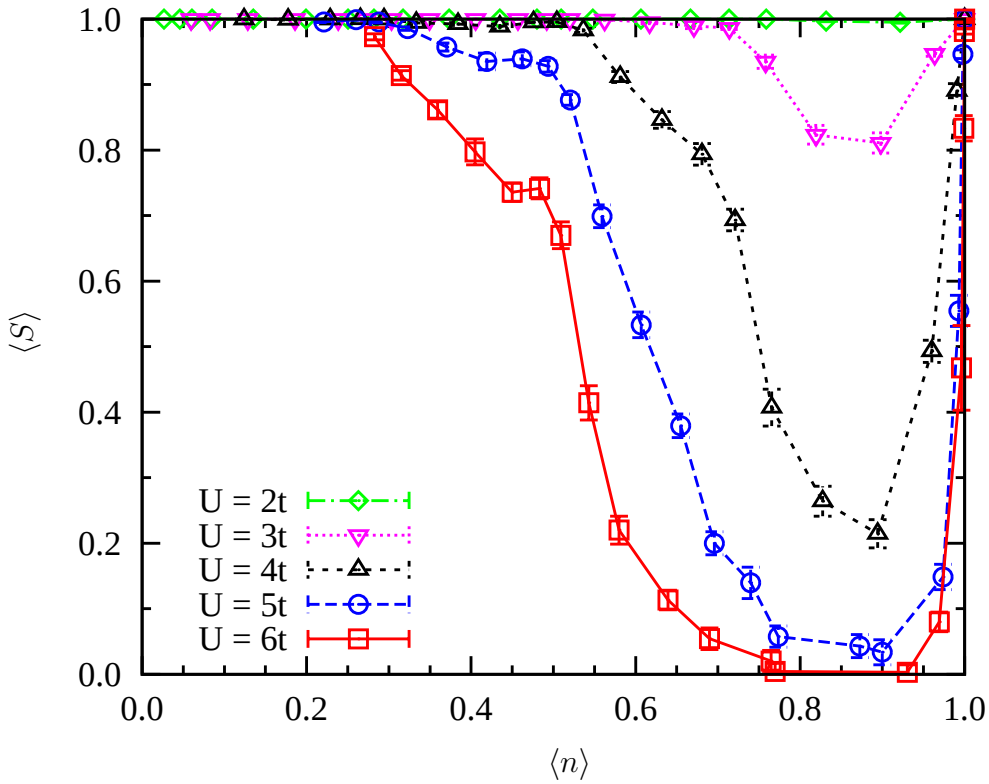

Figure 2.4: Average sign $\langle S \rangle$ vs. $\langle n \rangle$ for interaction strengths $U = 2t$, $3t$, $4t$, $5t$, and $6t$ on a 6×6 lattice at $\beta t = 6$. At the weakest couplings, the sign problem is virtually nonexistent, while for $U \geq 4t$, $\langle S \rangle \to 0$ for densities $0.65 \leq \langle n \rangle \leq 0.95$.

where $\langle\ \rangle_{\bar{P}}$ indicates an average with respect to the probability distribution $\bar{P}$. As long as $\langle S \rangle_{\bar{P}} \sim 1$, then we can obtain useful information about the system [34, 35]. When the sign deviates from 1, we must account for it in our measurement by means of Eq. (2.45).

$\langle S \rangle_{\bar{P}}$ depends on a multitude of factors. The most important of these are the inverse temperature β, the system size N, and the particle number. As seen in Refs. 34 and 35, the sign falls off exponentially with β. This is illustrated in Fig. 2.2 for a 10×10 lattice at $U = 4t$ and $8t$. Furthermore, it has been shown that the sign also depends on the particular path integral formulation [27]. For example, the world-line algorithm has no sign problem in one-dimension as the weights are all positive semidefinite, but in higher dimensions the sign problem is severe. For the DQMC algorithm, the type of Hubbard-Stratonovich transformation can have an enormous

effect on $\langle S \rangle$ [27–29].

Next, in Fig. 2.3, we show the dependence of the sign on the lattice filling $\langle n \rangle$ for different lattice sizes. The sign problem is at its worst in the region surrounding $\langle n \rangle = 0.85$, which is extremely problematic for any attempt at using the Hubbard model to explain the high-T_c superconductivity of the cuprates. We do note, however, that although increasing the size of the system does impact $\langle S \rangle$, it does so weakly and there is little difference between the average sign for a 10×10 and a 24×24 lattice (which contains nearly 6 times the number of sites!).

The fermion sign problem has been studied extensively in the literature. Additional information can be found in Refs. 7, 24, 27, and 30.

2.5 References

[1] J. E. Hirsch, R. L. Sugar, D. J. Scalapino, and R. Blankenbecler, Monte Carlo simulations of one-dimensional fermion systems, *Phys. Rev. B* **26**, 5033 (1982).

[2] R. Blankenbecler, D. J. Scalapino, and R. L. Sugar, Monte Carlo calculations of coupled boson-fermion systems I, *Phys. Rev. D* **24**, 2278 (1981).

[3] L. D. Landau and E. M. Lifshitz, *Statistical Physics*, vol. 5 of *Course of Theoretical Physics* (Butterworth-Heinemann, Oxford, 1980), third edition.

[4] R. K. Pathria, *Statistical Mechanics* (Elsevier Butterworth-Neinemann, Oxford, 1996), second edition.

[5] W. Krauth, *Statistical Mechanics: Algorithms and Computations* (Oxford University Press, UK, 2006).

[6] D. P. Landau and K. Binder, *A Guide to Monte Carlo Simulations in Statistical Physics* (Cambridge University Press, UK, 2000).

[7] J. Grotendorst, D. Marx, and A. Muramatsu (eds.), *Quantum Simulations of Complex Many-Body Systems: From Theory to Algorithms*, vol. 10 of *NIC Series* (John von Neumann Institute for Computing, 2002).

[8] M. Troyer, Classical and Quantum Monte Carlo Algorithms and Exact Diagonalization (2003), lecture notes for ORNL workshop on Wang-Landau sampling. They can be accessed at http://www.itp.phys.ethz.ch/people/troyer/troyerP27.pdf.

[9] R. P. Feynman and A. R. Hibbs, *Quantum Mechanics and Path Integrals* (McGraw-Hill, New York, 1965).

[10] H. F. Trotter, On the product of semi-groups of operators, *Proc. Am. Math. Soc.* **10**, 545 (1959).

[11] M. Suzuki, General correction theorems on decomposition formulae of exponential operators and extrapolation methods for quantum Monte Carlo simulations, *Phys. Lett.* **A113**, 299 (1985).

[12] R. M. Fye, New results on Trotter-like approximations, *Phys. Rev. B* **33**, 6271 (1986).

[13] R. M. Fye and R. T. Scalettar, Calculation of specific heat and susceptibilities with the use of the Trotter approximation, *Phys. Rev. B* **36**, 3833 (1987).

[14] M. Suzuki (ed.), *Quantum Monte Carlo Methods in Condensed Matter Physics* (World Scientific, 1993).

[15] H. G. Evertz, G. Lana, and M. Marcu, Cluster algorithm for vertex models, *Phys. Rev. Lett.* **70**, 875 (1993).

[16] N. V. Prokof'ev, B. V. Svistunov, and I. S. Tupitsyn, Exact Quantum Monte Carlo Process for the Statistics of Discrete Systems (1996), arXiv:cond-mat/9612091.

[17] B. B. Beard and U.-J. Wiese, Simulations of Discrete Quantum Systems in Continuous Euclidean Time, *Phys. Rev. Lett.* **77**, 5130 (1996).

[18] N. V. Prokof'ev, B. V. Svistunov, and I. S. Tupitsyn, Exact, complete, and universal continuous-time worldline Monte Carlo approach to the statistics of discrete quantum systems, *J. Exp. Theor. Phys.* **87**, 310 (1998).

[19] G. G. Batrouni and R. T. Scalettar, World-line quantum Monte Carlo algorithm for a one-dimensional Bose model, *Phys. Rev. B* **46**, 9051 (1992).

[20] R. T. Scalettar, World-line quantum Monte Carlo, in *Quantum Monte Carlo Methods in Physics and Chemistry*, vol. 525 of *Series C: Mathematical and Physical Sciences*, edited by M. P. Nightingale and C. J. Umrigar, pp. 65–100, NATO Science Series (Kluwer Academic Publishers, 1998).

[21] M. Troyer, F. Alet, S. Trebst, and S. Wessel, Non-local Updates for Quantum Monte Carlo Simulations (2003), arXiv:physics/0306128 (2003).

[22] M. Vekić and S. R. White, Determinantal and worldline quantum Monte Carlo methods for many-body systems, *Phys. Rev. B* **47**, 16131 (1993).

[23] A. Muramatsu, Quantum Monte Carlo for lattice fermions, in *Quantum Monte Carlo Methods in Physics and Chemistry*, vol. 525 of *Series C: Mathematical and Physical Sciences*, edited by M. P. Nightingale and C. J. Umrigar, pp. 343–374, NATO Science Series (Kluwer Academic Publishers, 1998).

[24] F. F. Assad and H. G. Evertz, World-line and Determinantal Quantum Monte Carlo Methods for Spins, Phonons, and Electrons, *Lecture Notes in Physics* **739**, 277 (2008).

[25] G. D. Mahan, *Many-Particle Physics*, Physics of Solids and Liquids (Springer, 2007), third edition.

[26] J. E. Hirsch, Discrete Hubbard-Stratonovich transformation for fermion lattice models, *Phys. Rev. B* **28**, 4059 (1983).

[27] G. G. Batrouni and R. T. Scalettar, Anomalous decouplings and the fermion sign problem, *Phys. Rev. B* **42**, 2282 (1990).

[28] G. G. Batrouni and P. de Forcrand, Fermion sign problem: Decoupling transformation and simulation algorithm, *Phys. Rev. B* **48**, 589 (1993).

[29] Y. Motome and M. Imada, A Quantum Monte Carlo Method and Its Applications to Multi-Orbital Hubbard Models, *Journal of the Physical Society of Japan* **66**, 1872 (1997).

[30] R. R. dos Santos, Introduction to quantum Monte Carlo simulations for fermionic systems, *Braz. J. Phys.* **33**, 36 (2003).

[31] G. Alvarez, M. S. Summers, D. E. Maxwell, M. Eisenbach, J. S. Meredith, J. M. Larkin, J. Levesque, T. A. Maier, P. R. C. Kent, E. F. D'Azevedo, and T. C. Schulthess, New algorithm to enable 400+ TFlop/s sustained performance in simulations of disorder effects in high-Tc superconductors, in *SC '08: Proceedings of the 2008 ACM/IEEE conference on Supercomputing*, pp. 1–10 (IEEE Press, Piscataway, NJ, USA, 2008).

[32] K. Michelsons and M. Jarrell, (unpublished).

[33] R. T. Scalettar, R. M. Noack, and R. R. P. Singh, Ergodicity at large couplings with the determinant Monte Carlo algorithm, *Phys. Rev. B* **44**, 10502 (1991).

[34] S. Sorella, S. Baroni, R. Car, and M. Parrinello, A Novel Technique for the Simulation of Interacting Fermion Systems, *Europhys. Lett.* **8**, 663 (1989).

[35] E. Y. Loh, J. E. Gubernatis, R. T. Scalettar, S. R. White, D. J. Scalapino, and R. L. Sugar, Sign problem in the numerical simulation of many-electron systems, *Phys. Rev. B* **41**, 9301 (1990).

Chapter 3

Static versus dynamic fluctuations in the one-dimensional Extended Hubbard Model

The work described in this Chapter was done in collaboration with Helen Craig, Warren Pickett, and Richard Scalettar. It has been published in Reference 1.

3.1 Introduction

The study of strong interaction effects in low-dimensional systems remains one of the most active fields of research in condensed matter physics. The extended Hubbard Hamiltonian (EHH) has been widely explored as a model of correlation effects in tight-binding systems and, more specifically, for the competition between different types of ground state order: charge density wave, antiferromagnetism, and, in the case of attractive interactions, superconductivity. In one dimension, it has also been used to understand the behavior of materials including conducting polymers [2] and organic superconductors [3].

The ground state phase diagram of the one-dimensional EHH was first obtained

within a weak coupling renormalization group (RG) calculation [4, 5]. For repulsive on-site interactions U which are sufficiently large compared to the intersite repulsion V, specifically, for $U > 2V$, the ground state is a spin density wave (SDW) phase, with power law decay of spin correlations. For $2V > U$, the ground state has charge density wave (CDW) order. These charge correlations exhibit true long range order, that is, they go asymptotically to a nonzero value at large separations, since the associated broken symmetry is discrete. Finally, for attractive intersite interactions, singlet and triplet superconducting phases exist at $T = 0$, again with power law decays of the associated correlation functions.

Subsequent to the RG work, the question of the order of the transitions between these different phases was studied, with a prediction that for repulsive U and V second-order SDW-CDW transitions at weak coupling were separated by a tricritical point from first-order transitions at strong coupling [6–9]. Up to several years ago, estimates of the location of the tricritical point varied from $U_t = 1.5t$ to $U_t = 5t$ (with $V_t \approx U_t/2$). More recently, this picture has been further modified by the suggestion that a narrow region exhibiting "bond ordered wave" (BOW) correlations separates the SDW and CDW regions at weak coupling [10–16].

The competition of CDW and SDW order in the one-dimensional EHH is further modified if the electrons couple to lattice degrees of freedom. In the case where these are static, most investigations have addressed the case when there is only on-site repulsion U, that is, $V = 0$. In this "ionic Hubbard model" the frozen distortions have an alternating pattern down the chain [17], and an additional issue is the possibility that the band insulator at $U = 0$ and half-filling is first driven metallic before becoming a SDW Mott insulator [18, 19]. If the coupling of the electrons to the lattice is in the form of dynamically varying phonon degrees of freedom, one has the Hubbard-Holstein or Su-Schrieffer-Heeger Hamiltonian.

The interplay between band-insulating behavior and electron-electron interaction

effects such as those studied in this chapter has recently been explored in a number of contexts. Dynamical mean field theory studies of binary alloy band insulators described by a bimodal distribution of randomly located one-body potentials have observed several novel effects, including Mott insulating behavior away from half-filling [20, 21] and band-insulator to metal transitions driven by increasing on-site repulsion [22]. Analogous studies of interacting bosons in "superlattice" potentials in which the site energies are modulated have also been used [23–27] to describe experiments on ultracold optically trapped (bosonic) atoms [28–31].

There has been relatively little work, especially using quantum Monte Carlo (QMC) simulations, which addresses how such lattice coupling affects the SDW-CDW phase boundary in the EHH in which both U and V are nonzero. In this chapter, we apply the world-line QMC (WLQMC) method to the one-dimensional EHH with an additional, static one-body potential, and with dynamically fluctuating ("Holstein") phonons. We quantitatively determine the amount of lattice coupling required to stabilize a charge ordered phase when the system begins at values of the electron-electron interactions in the spin density wave regime. An interesting feature of our results is that the quantum fluctuations induced by the hopping t have the opposite effect on the strong coupling ($t = 0$) phase boundary in the two cases. We also present detailed results for the evolution of the different components of the energy through the phase transition region.

The remainder of this chapter is organized as follows. An explicit description of our Hamiltonian and a brief review of our numerical approach are presented in Sec. 3.2. Results for coupling to static and dynamic lattice deformations are given in Secs. 3.3.1 and 3.3.2, respectively.

3.2 Model and Computational Methods

The extended Hubbard Hamiltonian is

$$\begin{aligned} \widehat{H}_{\text{el}} &= \widehat{K} + \widehat{P}\,, \\ \widehat{K} &= -t \sum_{i\sigma} (c^{\dagger}_{i+1,\sigma} c_{i,\sigma} + c^{\dagger}_{i,\sigma} c_{i+1,\sigma})\,, \\ \widehat{P} &= U \sum_{i} n_{i,\uparrow} n_{i,\downarrow} + V \sum_{i} n_i n_{i+1}\,. \end{aligned} \tag{3.1}$$

Here $c^{\dagger}_{i,\sigma}, c_{i,\sigma}$, and $n_{i,\sigma}$ are the creation, destruction, and number operators, respectively, for electrons of spin σ at site i of a one-dimensional lattice, and $n_i = \sum_\sigma n_{i,\sigma}$. The hopping t determines the kinetic energy (non-interacting band dispersion $\varepsilon_k = -2t\cos k$), and is set to $t = 1$. U and V, taken to be positive, are the on-site and intersite repulsions. We will be exclusively interested in the properties of the model at half-filling where the number of fermions $N_f = \sum_i n_i = N$, is equal to the number of lattice sites.

We will consider additional couplings to an on-site lattice degree of freedom,

$$\begin{aligned} \widehat{H} &= \widehat{H}_{\text{el}} + \widehat{H}_{\text{lattice}}\,, \\ \widehat{H}_{\text{IHM}} &= \Delta \sum_i (-1)^i n_i\,, \\ \widehat{H}_{\text{Holstein}} &= \lambda \sum_i x_i n_i + \sum_i \left(\frac{1}{2} p_i^2 + \frac{1}{2} \omega_0^2 x_i^2 \right)\,, \end{aligned} \tag{3.2}$$

where $\widehat{H}_{\text{lattice}}$ can take one of two possible forms: either static (ionic Hubbard model "IHM") or dynamic ("Holstein"). The half-filled one-dimensional IHM was proposed as a model ferroelectric by Nagaosoa [32] and Egami [33] as one expects a transition from an ionic band insulator to a Mott insulator as U is increased. The Hubbard-Holstein Hamiltonian is of particular interest in understanding how strong electronic correlations are influenced by electron-phonon interactions. Analytic and numeric

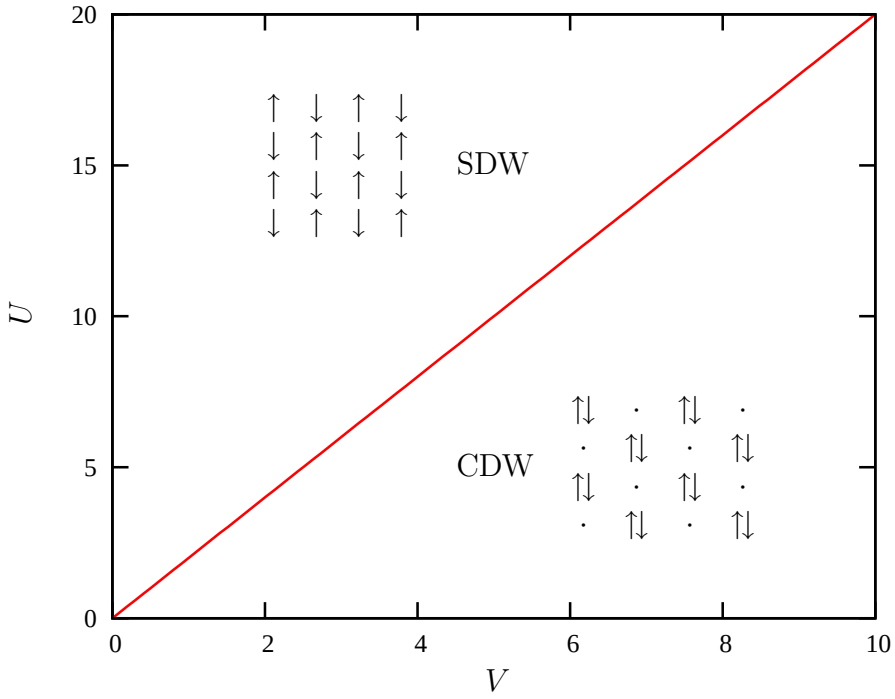

Figure 3.1: Phase diagram for the Extended Hubbard model in the strong-coupling limit $t = 0$ at half-filling. The boundary between the spin density wave and charge density wave phases lies on the line $U = 2V$.

studies on such Hamiltonians are quite numerous [18, 19, 32–44].

It is useful to review the strong coupling ($t = 0$) phase diagram (shown in Fig. 3.1), since when the hopping is nonzero the topology of the phase diagram is rather similar qualitatively and even quantitatively. In the absence of an interaction with the lattice, the SDW phase, which consists of a collection of singly occupied sites, has energy $E^{t=0}_{\mathrm{SDW}} = NV$, while the CDW phase has alternating empty and doubly occupied sites, and energy $E^{t=0}_{\mathrm{CDW}} = NU/2$. The boundary is given by $U = 2V$.

A static lattice distortion Δ breaks the twofold symmetry of the CDW state and lowers the energy by $N\Delta$ on the preferred sublattice. The resulting boundary is shifted to $V = U/2 - \Delta$.

In the case of coupling to a dynamical phonon, we can construct the $t = 0$ phase diagram by completing the square of the electron-phonon term in the Hamiltonian. The result is an oscillator with the same frequency ω_0 and an equilibrium position

shifted by λ/ω_0^2. An attractive on-site interaction $-(\lambda^2/2\omega_0^2)n_{i,\uparrow}n_{i,\downarrow}$ is also generated. Other terms can be absorbed into a shifted chemical potential and energy. As with the static term, the weakening of the on-site U shifts the strong coupling phase diagram in favor of CDW order. If $-(\lambda^2/2\omega_0^2)$ is sufficiently large, pairing correlations can come to dominate, especially in the doped case. We will not work in that parameter regime here.

In order to understand how the quantum fluctuations, which develop as t increases, modify these simple considerations, we employ the world-line quantum Monte Carlo (WLQMC) method [45]. Consider first the approach for $\widehat{H} = \widehat{H}_{\rm el} + \widehat{H}_{\rm IHM}$. We begin by discretizing the inverse temperature β into intervals $\epsilon = \beta/L$ in the partition function, and approximating the incremental (imaginary) time evolution operator by the product of the exponentials of the kinetic energy and potential energy terms separately.

$$Z = {\rm Tr}\left[e^{-\beta\widehat{H}}\right] \approx {\rm Tr}\left[e^{-\epsilon\widehat{K}}e^{-\epsilon(\widehat{P}+\widehat{H}_{\rm IHM})}\right]^L . \tag{3.3}$$

This Suzuki-Trotter approximation [46, 47] introduces errors in measurements [48, 49] which are of order the commutator $[\widehat{K},\widehat{P}]$, that is, $t\,U\,\epsilon^2$, $t\,\Delta\,\epsilon^2$, and $t\,V\,\epsilon^2$. Except where otherwise noted, we will choose $\epsilon = 0.25$, which is sufficiently small that the systematic Trotter errors in the location of the phase boundary are comparable to those arising from statistical fluctuations in the Monte Carlo sampling and uncertainties associated with finite size scaling.

The construction of a path integral for Z is completed by introducing complete sets of fermion occupation number states $I = \sum |n_{i,\sigma}\rangle_\tau \langle n_{i,\sigma}|_\tau$ both for the trace and at all imaginary times, i.e., between each product, $e^{-\epsilon\widehat{K}}e^{-\epsilon\left(\widehat{P}+\widehat{H}_{\rm IHM}\right)}$. The exponentials of the terms in $\widehat{P}+\widehat{H}_{\rm IHM}$ immediately act on the eigenstates, replacing all operators by numbers. Thus the weight of a particular occupation number configuration gets a

contribution $W_{\rm P}\, W_{\rm IHM}$,

$$W_{\rm P}(\{n_{i,\tau,\sigma}\}) = \exp\Big(\epsilon \sum_{i,\tau} \left[U n_{i,\tau,\uparrow} n_{i,\tau,\downarrow} + V(n_{i,\tau,\uparrow} + n_{i,\tau,\downarrow})(n_{i+1,\tau,\uparrow} + n_{i+1,\tau,\downarrow}\right]\Big)\,, \quad (3.4)$$

$$W_{\rm IHM}(\{n_{i,\tau,\sigma}\}) = \exp\Big(\epsilon \sum_{i,\tau} \Delta(-1)^i (n_{i,\tau,\uparrow} + n_{i,\tau,\downarrow})\Big)\,, \quad (3.5)$$

where $\{n_{i,\tau,\sigma}\}$ denotes the space- and imaginary-time-dependent occupation numbers in the collection of intermediate states.

To accomplish the same replacement of operators by numbers for the kinetic energy exponentials, $\widehat{K}$ is further subdivided (the "checkerboard decomposition") [45, 50] into

$$\begin{aligned} \widehat{K} &= \widehat{K}_{\rm odd} + \widehat{K}_{\rm even}\,, \\ \widehat{K}_{\rm odd} &= -t \sum_{i \text{ odd}} \sum_{\sigma} (c^\dagger_{i+1,\sigma} c_{i,\sigma} + c^\dagger_{i,\sigma} c_{i+1,\sigma})\,, \\ \widehat{K}_{\rm even} &= -t \sum_{i \text{ even}} \sum_{\sigma} (c^\dagger_{i+1,\sigma} c_{i,\sigma} + c^\dagger_{i,\sigma} c_{i+1,\sigma})\,. \end{aligned} \quad (3.6)$$

The expectation value of $\widehat{K}_{\rm odd}$ and $\widehat{K}_{\rm even}$ between the occupation number states $|n_{i,\sigma}\rangle_\tau$ and $\langle n_{i,\sigma}|_{\tau+1}$ then reduces to a product of independent two-site problems which can be solved analytically. Since particle number is conserved in each hopping process, the number of electrons on each pair of sites in the two states to the left and to the right of the exponential is identical. Thus the world lines generated by connecting all occupied sites ($n_{i,\tau,\sigma} = 1$) are continuous. The four nonzero matrix elements are

$$\left\langle\, 00 \,\middle|\, e^{\epsilon t (c^\dagger_1 c_2 + c^\dagger_2 c_1)} \,\middle|\, 00 \,\right\rangle = 1\,, \quad (3.7a)$$

$$\left\langle\, 11 \,\middle|\, e^{\epsilon t (c^\dagger_1 c_2 + c^\dagger_2 c_1)} \,\middle|\, 11 \,\right\rangle = 1\,, \quad (3.7b)$$

$$\left\langle\, 10 \,\middle|\, e^{\epsilon t (c^\dagger_1 c_2 + c^\dagger_2 c_1)} \,\middle|\, 10 \,\right\rangle = \cosh(t\epsilon)\,, \quad (3.7c)$$

$$\left\langle\, 10 \,\middle|\, e^{\epsilon t (c^\dagger_1 c_2 + c^\dagger_2 c_1)} \,\middle|\, 01 \,\right\rangle = \sinh(t\epsilon)\,. \quad (3.7d)$$

The product of all these factors over the space-time lattice constitutes a second contribution $W_{\rm K}$ to the weight associated with the configuration. Thus, the total weight is $W_{\rm tot} = W_{\rm P} W_{\rm IHM} W_{\rm K}$. Because all of the matrix elements are positive in one dimension, the WLQMC algorithm does not exhibit a sign problem.

In the case $\widehat{H} = \widehat{H}_{\rm el} + \widehat{H}_{\rm Holstein}$, the trace and intermediate states include not only fermion occupation labels, but also a complete set of phonon position eigenstates. As with $\widehat{H}_{\rm el}$, the exponential of the phonon kinetic and potential energies is discretized and split apart. The result is that in addition to the electronic contributions $W_P\, W_K$ there is a final phonon piece,

$$W_{\rm ph}(\{x_{i,\tau}\}) = \exp\left[\frac{1}{2}\epsilon \sum_{i,\tau} \omega_0^2 x_{i,\tau}^2 + \left(\frac{x_{i,\tau+1} - x_{i,\tau}}{\epsilon}\right)^2\right] . \tag{3.8}$$

Let us then summarize the basic features of the simulation. The degrees of freedom being summed over are two space-time arrays of occupation numbers $n_{i,\tau,\uparrow}$ and $n_{i,\tau,\downarrow}$, and, in the Holstein case, a space-time array of phonon coordinates $x_{i,\tau}$, with $i = 1, 2, \ldots, N$ and $\tau = 1, 2, \ldots, 2M$. (The factor of 2 comes from the checkerboard decomposition.) The total weight of the configuration is $W_{\rm tot} = W_{\rm P} W_{\rm K} W_{\rm Ph}$. The elemental Monte Carlo moves consist of local distortions of the continuous world lines, together with updates of the phonon degrees of freedom. Moves are accepted or rejected according to the Metropolis algorithm: a random number $0 < r < 1$ is generated and the move is accepted if $r < W'_{\rm tot}/W_{\rm tot}$.

The WLQMC algorithm can suffer from long autocorrelation times. Other approaches such as the stochastic series expansion method [51–53] and loop algorithms [54] can be used to speed up the evolution in phase space. Here we confine ourselves only to introducing global moves [55] in the phonon degrees of freedom to address even more serious large autocorrelation times there.

We conclude with a discussion of the observables we will measure. The various

components of the energy exhibit sharp features as the phase boundaries are crossed. Real space spin, charge (relative to the mean), and bond operators are defined by

$$m(l,\tau) = n_{l,\tau,\uparrow} - n_{l,\tau,\downarrow}\,, \tag{3.9a}$$

$$n(l,\tau) = n_{l,\tau,\uparrow} + n_{l,\tau,\downarrow} - 1\,, \tag{3.9b}$$

$$k(l,\tau) = \sum_{\sigma} (c^{\dagger}_{l+1,\sigma}(\tau)c_{l,\sigma}(\tau) + c^{\dagger}_{l,\sigma}(\tau)c_{l+1,\sigma}(\tau))\,. \tag{3.9c}$$

The associated correlation functions are

$$c_{\mathrm{spin}}(l,\tau) = \langle m(l,\tau)m(0,0)\rangle\ , \tag{3.10a}$$

$$c_{\mathrm{charge}}(l,\tau) = \langle n(l,\tau)n(0,0)\rangle\ , \tag{3.10b}$$

$$c_{\mathrm{bond}}(l,\tau) = \langle k(l,\tau)k(0,0)\rangle\ , \tag{3.10c}$$

where $(0,0)$ is some reference site in our system. The local moment is defined as $\langle m_z^2\rangle = c_{\mathrm{spin}}(0,0)$.

We will also look at the Fourier transforms of these quantities. The equal time spin structure factor is

$$S_{\mathrm{spin}}(q) = \frac{1}{N}\sum_{l} e^{iql} c_{\mathrm{spin}}(l,0)\,, \tag{3.11}$$

with analogous definitions for S_{charge} and S_{bond}. The corresponding zero-frequency susceptibility is

$$\chi_{\mathrm{spin}}(q) = \frac{1}{N}\sum_{\tau}\sum_{l} e^{iql} c_{\mathrm{spin}}(l,\tau)\,, \tag{3.12}$$

again with analogous definitions for χ_{charge} and χ_{bond}.

At half-filling the largest responses in the Hubbard model are at wave vector $q = \pi$. In a disordered phase, $c(l,0)$ decays exponentially to zero with the site separation l,

and the structure factor is independent of lattice size N. If true long range order develops, then the structure factor grows linearly with lattice size, with the factor $e^{i\pi l}$ providing the necessary phases so that the oscillating $c(l)$ add constructively. The susceptibility similarly examines the asymptotics in imaginary time, diverging as $\beta \to \infty$ when $c(l, \tau)$ remains nonzero for large τ.

3.3 Results

3.3.1 Extended Ionic Hubbard Hamiltonian

In the extended Hubbard Hamiltonian with $U = 6t$ and $V = 1.5t$, we are well within the SDW phase since $U > 2V$. In Fig. 3.2 we see that as Δ is increased, the SDW susceptibility decreases and the CDW susceptibility grows. Indeed, χ_{CDW} rises dramatically in the vicinity of $\Delta = U/2 - V$, as suggested by the strong coupling analysis. The transition becomes increasingly sharp as the lattice size is increased. Because the CDW correlations break a discrete symmetry, true long range order is possible at $T = 0$. With our normalization conventions we expect the CDW structure factor and susceptibility to grow linearly with lattice size after the onset of long range order. This is borne out in the central panel of Fig. 3.2. The inset in this panel shows a scaled version of the raw data for χ_{CDW}. A crossing of the curves for different lattice sizes N allows us to determine the location of the critical point.

The SDW correlations that are dominant at small Δ break a continuous symmetry, and hence in one dimension decay with a power law at $T = 0$, that is, $c_{\mathrm{spin}}(l, 0) \propto 1/l$. This behavior accounts for the relatively less rapid growth of the SDW susceptibility with lattice size.

It is important to make another distinction between the CDW and SDW phases, the phases that arise as broken symmetries from the interaction terms V and U, and the staggered density which is caused by the one-body term Δ. This staggered

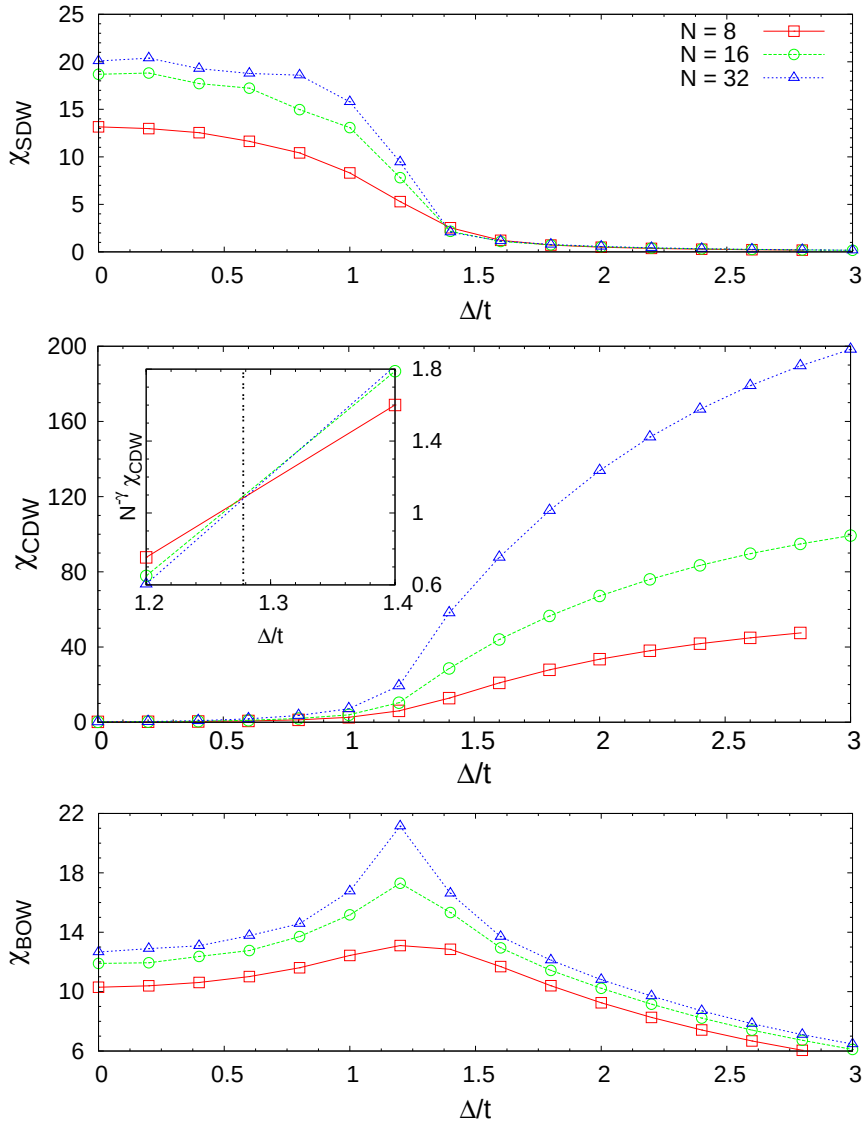

Figure 3.2: Spin density wave (top), charge density wave (middle), and bond ordered wave (bottom) susceptibilities versus staggered site energy Δ for $U = 6t$, $V = 1.5t$, $\beta t = 8$, and $N = 8, 16, 32$. The SDW-CDW transition occurs at close to the $t = 0$ value, $\Delta = U/2 - V$. BOW correlations are enhanced in the intermediate region. In the inset to the central panel, the scaled χ_{CDW} is shown for $\gamma = 1$. The scaled susceptibilities cross at $\Delta_c/t = 1.278$, indicated by the vertical dotted line.

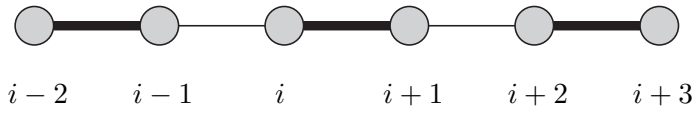

Figure 3.3: Illustration of a BOW phase. The thick lines indicate a high kinetic energy while the thin lines indicate a small kinetic energy.

potential Δ breaks translational invariance so that there is a small degree of CDW order even in the SDW phase. By contrast, in a competition solely between U and V at $\Delta = 0$, no CDW order would exist in the SDW phase.

The bottom panel of Fig. 3.2 shows the BOW correlations. In a BOW phase the kinetic energy on the links oscillates between two values as one traverses the chain (see Fig. 3.3). SDW correlations are immediately plausible after observing that U leads to singly occupied sites (moment formation) and that neighboring spins that are antiparallel have a second-order lowering of their energy ($\Delta E^{(2)} \propto -t^2/U$) relative to neighboring spins that are parallel. Analogous reasoning applies to CDW correlations. A picture of the less familiar BOW order is the following: consider a CDW pattern of doubly occupied and empty sites. A fermion hopping from doubly occupied site i onto neighboring empty site $i+1$ will prevent, through the interaction U, the hopping of a second electron from doubly occupied site $i+2$ onto $i+1$. Instead, an electron on site $i+2$ would prefer to hop to $i+3$. Thus the bonds $(i, i+1)$ and $(i+2, i+3)$ have high kinetic energy, while the intermediate bond $(i+1, i+2)$ has low kinetic energy. This way of understanding the origin of BO invokes both CDW and SDW correlations, making it plausible that the BOW might form on the boundary between the two.

Since the BOW phase also breaks a discrete translational symmetry, the associated ground state order should be long ranged. As mentioned in the Introduction, in the extended Hubbard model ($\Delta = 0$) the original picture of the phase diagram was one with only SDW and CDW regions, with a weak coupling second-order transition changing at a tricritical point to a strong coupling first-order transition [6–9]. Recent QMC simulations with the stochastic series expansion (SSE) have suggested instead that, at weak coupling, as V is increased at fixed U there are two separate transitions: a SDW-BOW transition of the Kosterlitz-Thouless type, followed by a second-order BOW-CDW transition. These transitions merge at a multicritical point into a single,

direct, first order SDW-CDW transition line at strong coupling [12]. The multicritical point was found to be at $(U_m, V_m) = (4.7 \pm 0.1, 2.51 \pm 0.04)$.

Aspects of this conclusion had been challenged by density matrix renormalization group calculations [56–58]. In particular, the suggestion is that the BOW phase exists only precisely on the SDW-CDW transition line, as opposed to being present in an extended region. Moreover, rather than starting at $U = V = 0$ and reaching out to the multi-critical point, the BOW line was concluded to begin at finite, nonzero coupling and also extend somewhat beyond the numerical value for the multi-critical point obtained using the SSE. Further SSE calculations [14] and functional RG treatments [16] appear to confirm earlier SSE work.

We do not propose here to add to this discussion, since our main focus is on the shift in the SDW-CDW phase boundary. Indeed, the value of U in Fig. 3.2 is large enough that we would likely be above the BOW region of the phase diagram. Nevertheless, the bottom panel of Fig. 3.2 does indicate a pronounced maximum in χ_{BOW} near the SDW-CDW transition, hinting that such order may be present at weaker coupling. If long range BO were to exist, we would expect to see χ_{BOW} grow linearly with N, as does χ_{CDW}. This is clearly not the case for the parameters and lattice sizes of Fig. 3.2.

In Fig. 3.4 we fix $U = 6t$ and the lattice size at $N = 32$, and sweep Δ for different choices of V. As expected, the size of Δ required to destroy the SDW phase decreases as the intersite interaction V, which cooperates with Δ, rises. As with the data of Fig. 3.2, the fall of χ_{SDW} coincides closely with the rise of χ_{CDW}. In each case the transition is marked also by a maximum in χ_{BOW}. The sharpness of the peak in χ_{BOW} diminishes as V grows, which is consistent with the SSE [57] and density matrix (DM) RG [56] calculations on the extended Hubbard model which (although they disagree in certain respects) both conclude that BO is not present at strong coupling. We note that a Mott-insulator–BO transition has also been suggested by Zhang *et al.* in the

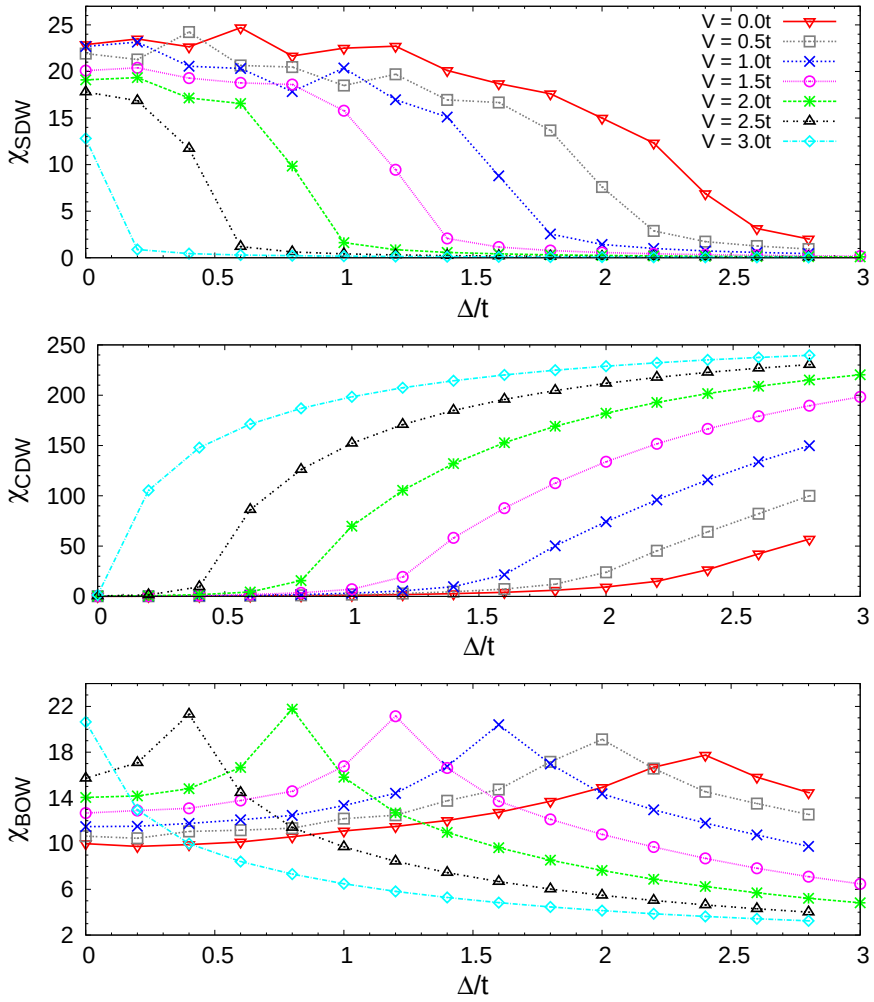

Figure 3.4: Spin density wave (top), charge density wave (middle), and bond ordered wave (bottom) susceptibilities versus staggered site energy Δ for $U = 6t$, $V = 0.0t, (0.5t), 3.0t$, and $N = 32$.

$V = 0$ limit with $\Delta = 2.0$ and $U_c = 5.95 \pm 0.01$ [42].

The behavior of the total energy, Fig. 3.5(a), is featureless through the sweep upward in Δ. However, abrupt evolution of the individual components of the energy, Figs. 3.5(b)-(d), accompanies the transitions in the susceptibilities. The energy associated with V decreases sharply upon exiting the SDW phase where adjacent sites are occupied, while the energy associated with U jumps upward with the development of double occupancy. The kinetic energy is relatively benign, but, like χ_{BOW}, reaches maxima along the SDW-CDW transition line. Evidently, the near balance be-

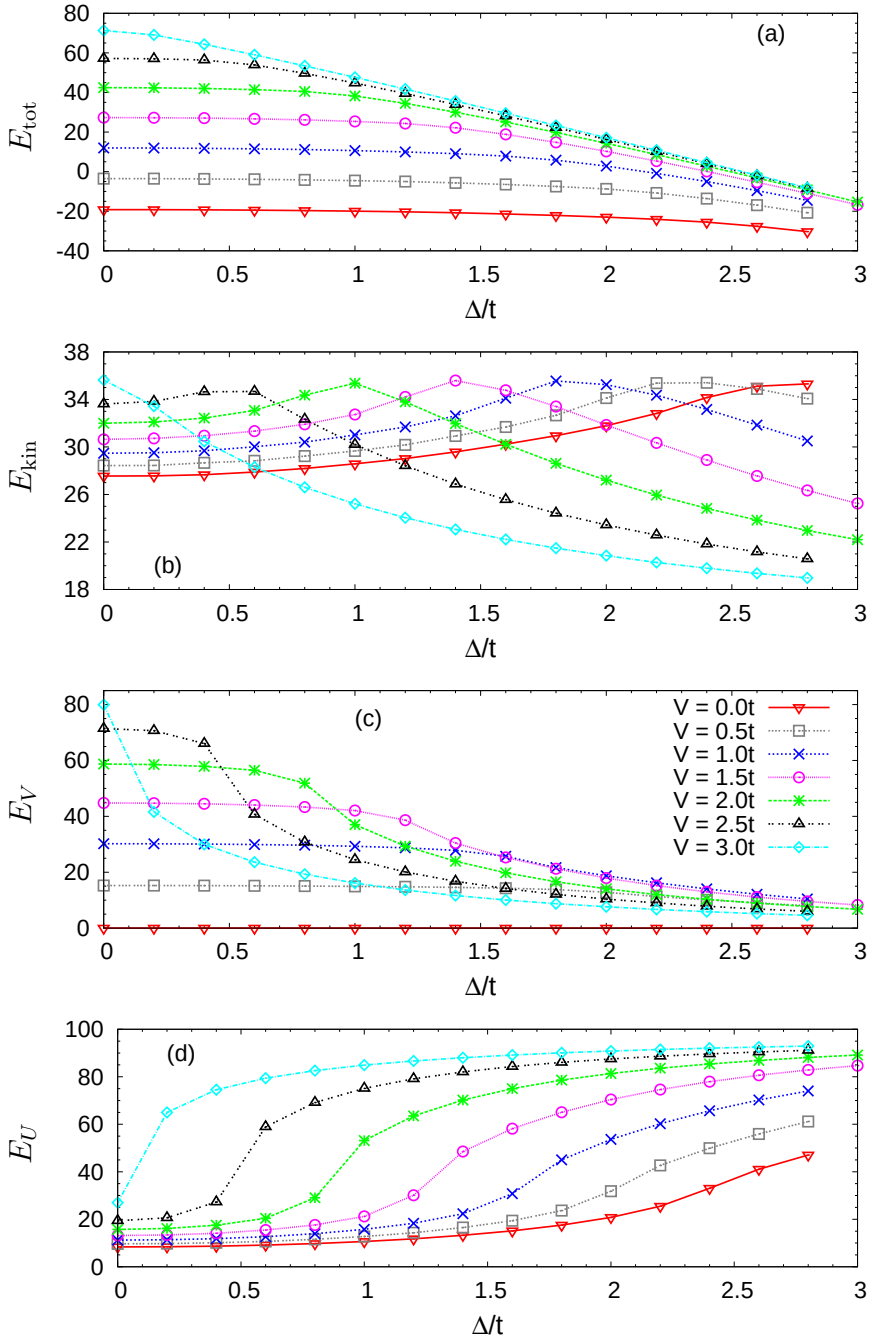

Figure 3.5: Total (a), kinetic (b), intersite Coulomb (c), and on-site Coulomb (d) energies at fixed $U = 6t$ and different V. The inverse temperature is fixed at $\beta t = 8$ and the lattice size at $N = 32$. The kinetic energy is largest in the region where there is a balance between the CDW and SDW insulating tendencies, in good correspondence with the behavior of χ_{BOW}. The intersite interaction energy falls abruptly on entry to the CDW state, and the on-site energies rise steeply as the pairs form.

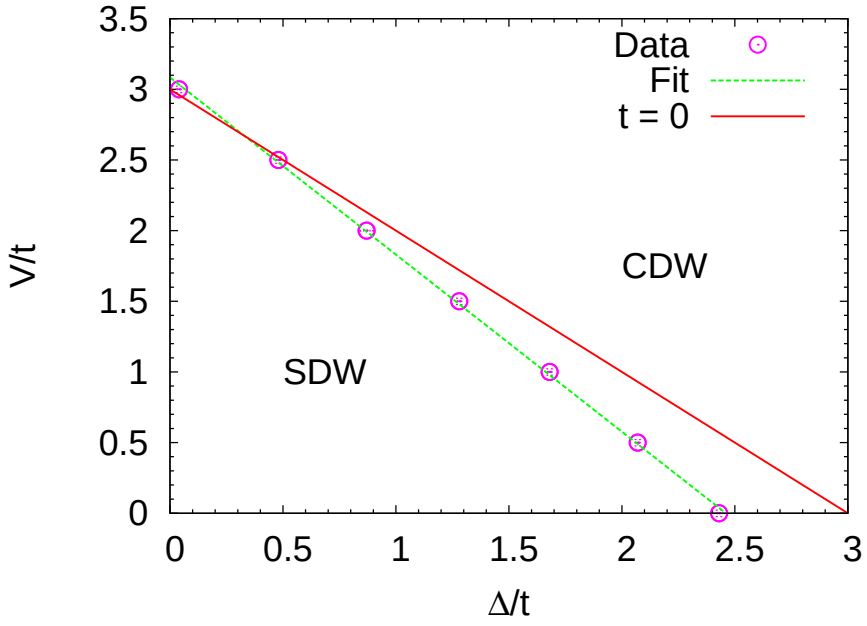

Figure 3.6: Phase diagram in the intersite V and staggered site energy Δ plane, with $U = 6t$ and $\beta t = 8$. Line with symbols is the result of the WLQMC simulations in this chapter. We also show the exact result (line without symbols) for $t = 0$. As expected, the strong coupling limit works well at large V, but there are significant deviations as V becomes smaller.

tween the insulating tendencies of U and V allows greater fluctuation in the electron positions.

The values of Δ at which the different susceptibilities change abruptly, and at which features in the energy are also evident, enable us to draw the phase diagram in the V-Δ plane for fixed $U = 6t$ shown in Fig. 3.6. At $\Delta = 0$ our QMC results match quite nicely the DMRG results of Jeckelmann [56], who finds $V_c = 3.155 \pm 0.005$ for $U = 6t$. This $\Delta = 0$ transition point is not too far shifted from the strong coupling value $V_c = U/2 = 3t$ when $U = 6t$.

As the staggered potential Δ becomes greater, our QMC phase boundary bends more away from the $t = 0$ line $V_c = U/2 - \Delta$. The SDW phase appears to terminate at $\Delta = 2.46 \pm 0.05$ in the absence of intersite repulsion V. While labeled as CDW, the large Δ phase in the $V = 0$ limit is perhaps more properly termed a band insulator, where the alternating charge density is a consequence of the staggered one-body

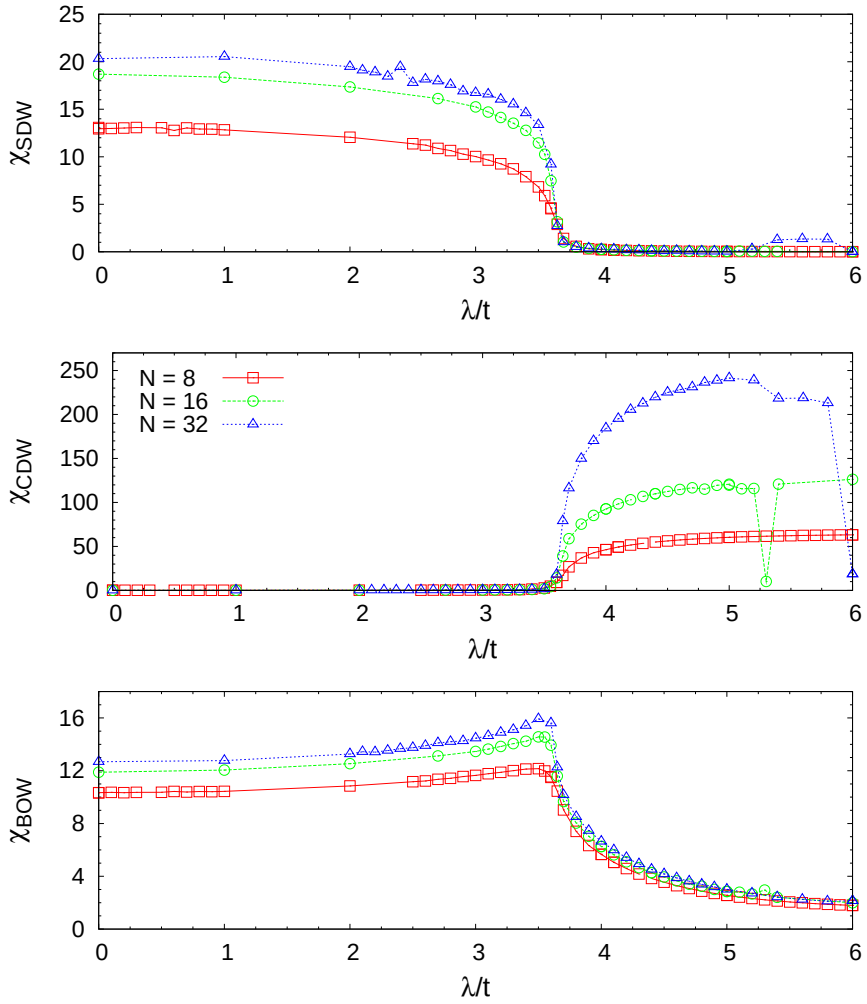

Figure 3.7: Spin density wave (top), charge density wave (middle), and bond ordered wave (bottom) susceptibilities versus electron-phonon coupling λ for $U = 6t$, $V = 1.5t$, $\omega_0 = 2t$, $\beta t = 8$, and $N = 8, 16, 32$.

potential as opposed to many-body effects.

3.3.2 Extended Hubbard Holstein Hamiltonian

Having completed our discussion of the case of the interplay of a static alternating external potential with the correlation terms U, V in the extended Hubbard Hamiltonian, we now give analogous results for the case when we couple to dynamical (Holstein) lattice distortions. Figure 3.7 is a companion to Fig. 3.2, showing the evolution of the spin, charge, and bond susceptibilities with electron-phonon coupling λ

(rather than staggered potential Δ) for different system sizes N. As discussed earlier, λ has a similar qualitative effect to Δ, since it weakens the on-site repulsion U and hence drives CDW formation. There are significant quantitative differences between the two situations. The SDW-CDW transition as a function of electron-phonon coupling λ appears to be much more abrupt. Recall that Δ breaks the lattice symmetry explicitly, selecting out a single preferred sublattice. It induces CDW order even within the SDW phase and as a consequence the change through the transition is less dramatic. The Holstein interaction, in contrast, spontaneously breaks the translational symmetry when it drives CDW order. We note further that BOW order is less sharply peaked at the SDW-CDW boundary.

Figure 3.8 is a companion to Fig. 3.4, similarly showing the susceptibilities as a function of electron-phonon coupling constant λ for a collection of values of V at a single lattice size $N = 32$ and $\omega_0 = 2t$. As V increases, a smaller λ is sufficient to drive CDW formation. There appears to be some variation of the sharpness of the evolution of the susceptibilities near λ_c as V is varied, with the most abrupt behavior occurring for intermediate V. In the extended Hubbard model ($\lambda = 0$), the transitions become monotonically more steep with increasing V. Indeed, as noted earlier, they change from continuous to discontinuous beyond the tri(multi)-critical point. The fluctuations of χ_{CDW} at large λ in Fig. 3.8 (middle panel) often occur in QMC studies of electron-phonon Hamiltonians and are associated with long equilibration times which occur when the electrons and lattice degrees of freedom are strongly coupled.

As with $\widehat{H}_{\mathrm{IHM}}$, the components of the energy (Fig. 3.9) lend important supporting evidence for the locations of the transition points. The behavior of E_V and E_U is the same as that observed previously in Fig. 3.5, and is more or less clear: in the SDW phase most sites are singly occupied and there is a significant contribution to E_V, which then drops abruptly in the CDW phase where doubly occupied and empty sites alternate. In contrast, E_U is small in the SDW phase since sites are

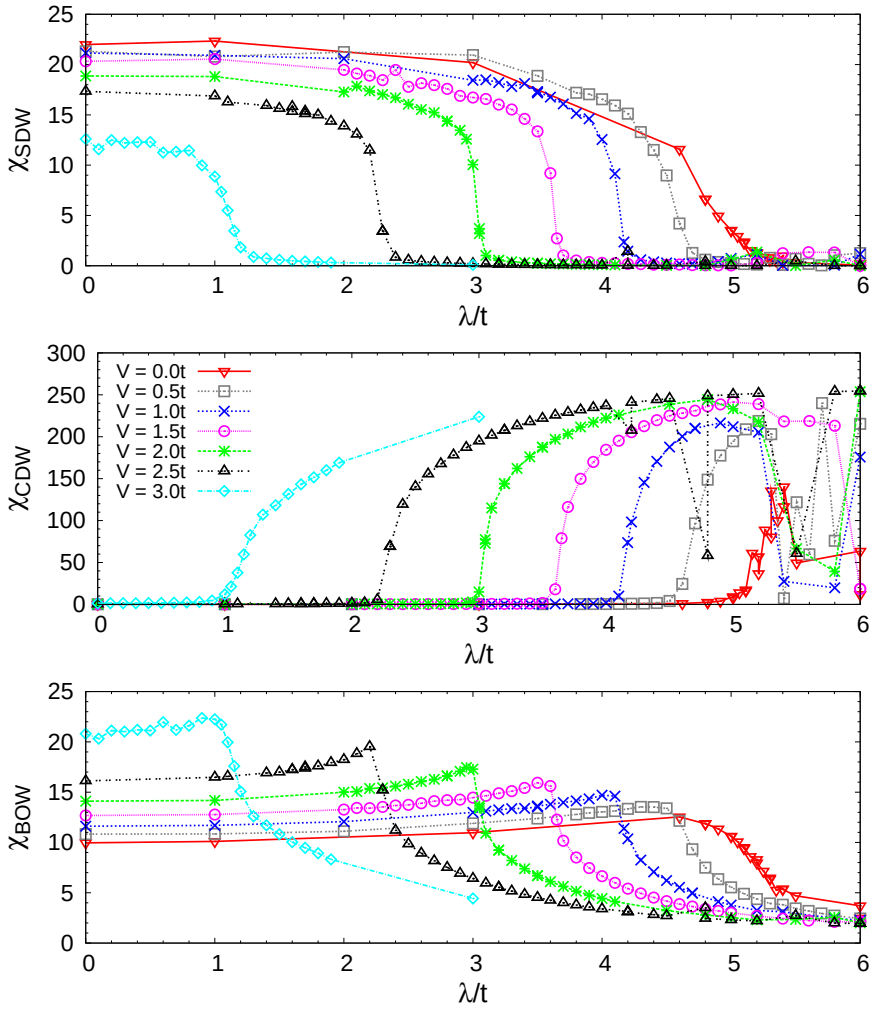

Figure 3.8: Spin density wave (top), charge density wave (middle), and bond ordered wave (bottom) susceptibilities versus electron-phonon coupling λ for $U = 6t$, $V = 0.0t, (0.5t), 3.0t$, $\omega_0 = 2t$, and $N = 32$.

singly occupied, but then increases sharply in the CDW phase. What is perhaps less intuitive is the evolution of the phonon contributions to the energy. As λ grows, the $t = 0$ analysis suggests a smooth quadratic increase, $E^{\text{pot}}_{\text{phonon}} = \lambda^2/2\omega_0^2$. Instead the phonon potential energy remains relatively flat throughout the SDW region, and then jumps up as the CDW is entered. The phonon kinetic energy is especially interesting, showing a well-defined *minimum* in the transition region. The origin of this effect is not clear. $E^{\text{kin}}_{\text{phonon}}$ is measured by the fluctuations of the phonon coordinates in imaginary time. Naively, one might expect kinetic lattice fluctuations to be *largest*

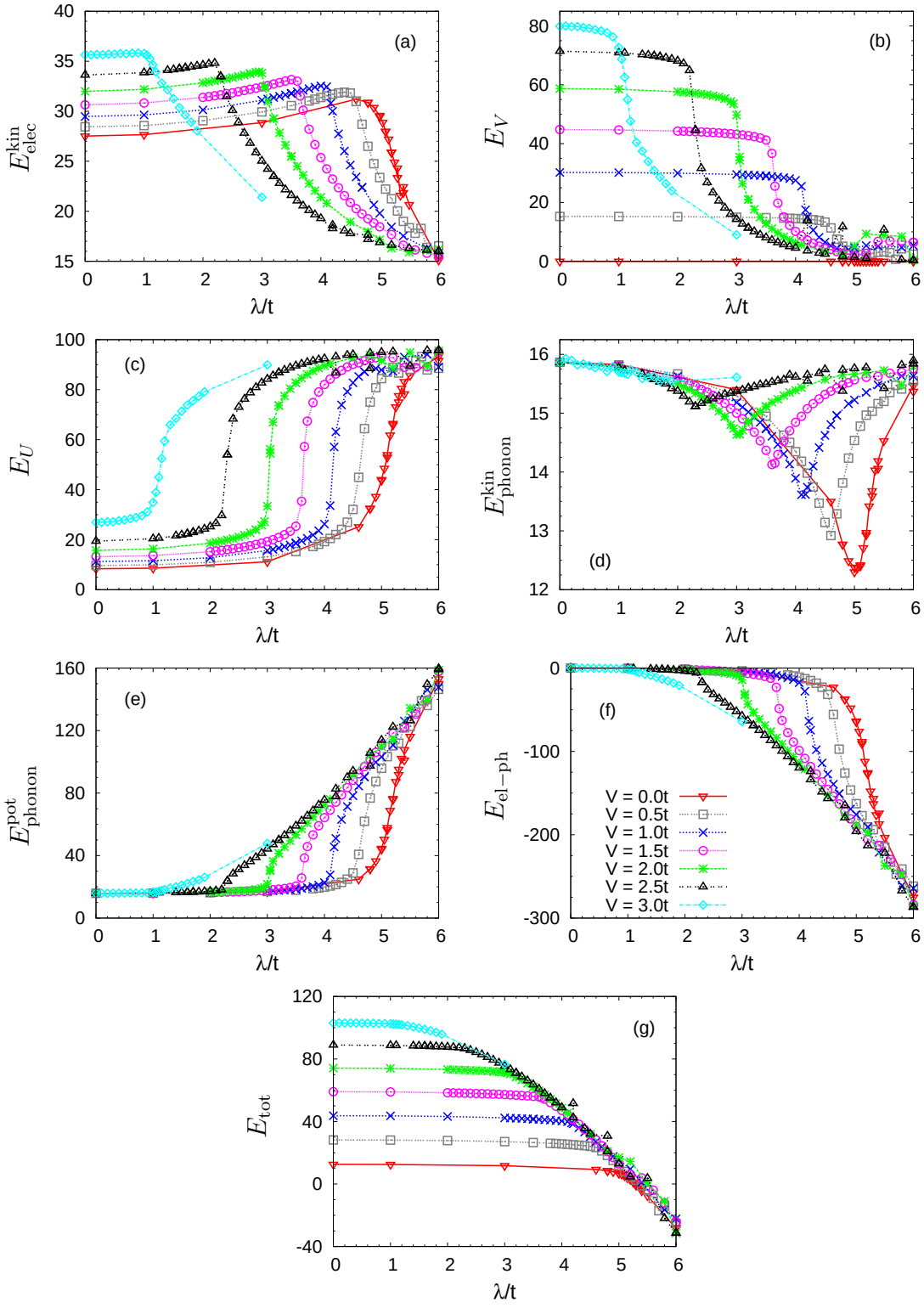

Figure 3.9: (a) Kinetic (hopping), (b) intersite Coulomb, (c) on-site Coulomb, (d) kinetic (phonon), (e) potential (phonon), (f) electron-phonon coupling, and (g) total energies versus coupling constant λ for $U = 6t$, $V = 0.0t, (0.5t), 3.0t$, $\beta t = 8$, $\omega_0 = 2t$, and $N = 32$. The fluctuations in the phonon kinetic energy are significantly smaller than those for all other energies for these parameters.

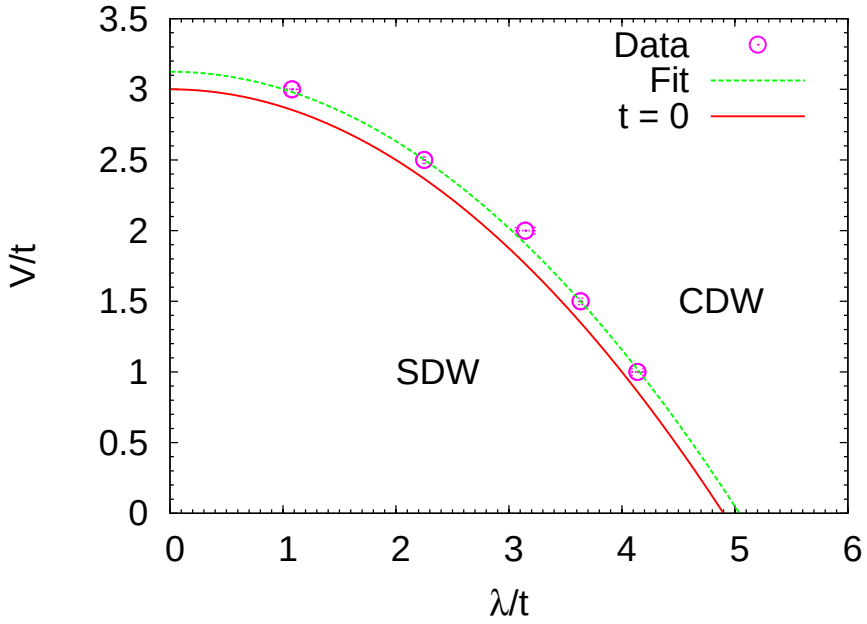

Figure 3.10: This figure shows the phase diagram for intersite V and electron-phonon coupling λ with $U = 6t$, $\omega_0 = 2t$, and $\beta t = 8$. Line with symbols is the result of the WLQMC simulations in this chapter. The functional form of the fit is $V = a\lambda^2 + b$. We show the exact result (line without symbols) for the $t = 0$ phase.

in the SDW-CDW transition region where the system is undecided between which type of order to assume. In the case of the electron kinetic energy we see precisely this effect in Fig. 3.9(a). The opposite appears to be the case for the phonon kinetic energy.

Finally, Fig. 3.10 shows the phase diagram in the V-λ plane at fixed $U = 6t$. It shares the same general features as Fig. 3.6 with a SDW phase near the origin that is destroyed when either the intersite repulsion V or the electron phonon coupling λ increases sufficiently. Figure 3.10 describes how large a value of electron-phonon coupling λ is required to convert the SDW phase, favored by U, to the CDW phase, favored by V, and is representative of how λ affects the extended Hubbard model phase diagram at all intermediate to large interaction strengths. It is important to note that, unlike Fig. 3.6, the QMC phase boundary does not bend away from the $t = 0$ line $V_c = U/2 - \lambda^2/4\omega_0$. Instead, the boundary is uniformly shifted to increase

the critical intersite repulsion, favoring SDW order. Again, the $\lambda = 0$ point on our phase boundary ($V_c = 3.124 \pm 0.011$) agrees well with Jeckelmann's DMRG treatment. (See above discussion of Fig. 3.6.)

For finite λ we can compare against the phase diagram of Sil and Bhattacharyya who study the same extended Hubbard model coupled to Holstein phonons [44]. They draw the phase boundary in the U-V plane for different electron-phonon couplings. Translating to the units used in this chapter, for $U = 6t$ and $V = 2t$, their data suggest that the CDW phase is destroyed at $\lambda_c \approx 2.8$. Our Fig. 3.10 gives $\lambda_c \approx 3.0$ at $V = 2t$ for the same parameters. Likewise, Sil and Bhattacharyya find that for $\lambda = 5.6$ there is no SDW phase at $U = 3t$. This is again nicely consistent with our data, which suggest that when $\lambda = 5.04 \pm 0.06$ there is CDW order.

3.4 Summary

We have presented world-line quantum Monte Carlo simulations of the one-dimensional extended Hubbard Hamiltonian for which coupling to static staggered (ionic Hubbard) or dynamic (Holstein) lattice degrees of freedom is added. The evolution of the susceptibilities to different types of order and the components of the energy were examined. For both static and dynamic couplings the region of charge density wave order in the phase diagram is found to be stabilized, and the phase boundaries are pinned down. Bond order is shown to be enhanced in the vicinity of the spin density to charge density transition.

The results obtained in this work also show good agreement with previous studies. The zero-coupling limit ($\Delta, \lambda = 0$) results conform well with Jeckelmann's DMRG results. For dynamic couplings, the results compare favorably with the results of Sil *et al.*

A comparison of the QMC phase boundaries with their counterpart in the $t = 0$

limit shows a markedly different behavior between the two types of coupling. For static couplings, the CDW phase is enhanced in the QMC calculation. Conversely, there is an enhancement of the SDW correlations with Holstein phonons.

Acknowledgements

We acknowledge support from the DOE under Grant No. DE-FG01-06NA26204 and the NSF Grant No. REU PHY-0243904, and useful input from G.K. Pips.

3.5 References

[1] H. A. Craig, C. N. Varney, W. E. Pickett, and R. T. Scalettar, Static versus dynamic fluctuations in the one-dimensional extended Hubbard model, *Phys. Rev. B* **76**, 125103 (2007).

[2] H. G. Keiss (ed.), *Conjugated Conducting Polymers* (Springer-Verlag, Berlin, 1992).

[3] T. Ishiguro and K. Yamaji, *Organic Superconductors* (Springer-Verlag, Berlin, 1990).

[4] V. J. Emery, in *Highly Conducting One Dimensional Solids*, edited by J. Devreese, R. Evrard, and V. van Doren (Plenum, New York, 1979).

[5] J. Sólyom, The Fermi gas model of one-dimensional conductors, *Adv. Phys.* **28**, 201 (1979).

[6] J. E. Hirsch, Charge-Density-Wave to Spin-Density-Wave Transition in the Extended Hubbard Model, *Phys. Rev. Lett.* **53**, 2327 (1984).

[7] J. E. Hirsch, Phase diagram of the one-dimensional molecular-crystal model with Coulomb interactions: Half-filled-band sector, *Phys. Rev. B* **31**, 6022 (1985).

[8] J. W. Cannon and E. Fradkin, Phase diagram of the extended Hubbard model in one spatial dimension, *Phys. Rev. B* **41**, 9435 (1990).

[9] J. W. Cannon, R. T. Scalettar, and E. Fradkin, Ground-state phase diagram of the one-dimensional extended Hubbard model, *Phys. Rev. B* **44**, 5995 (1991).

[10] M. Nakamura, Mechanism of CDW-SDW Transition in One Dimension, *J. Phys. Soc. Jpn.* **68**, 3123 (1999).

[11] M. Nakamura, Tricritical behavior in the extended Hubbard chains, *Phys. Rev. B* **61**, 16377 (2000).

[12] P. Sengupta, A. W. Sandvik, and D. K. Campbell, Bond-order-wave phase and quantum phase transitions in the one-dimensional extended Hubbard model, *Phys. Rev. B* **65**, 155113 (2002).

[13] M. Tsuchiizu and A. Furusaki, Phase Diagram of the One-Dimensional Extended Hubbard Model at Half Filling, *Phys. Rev. Lett.* **88**, 056402 (2002).

[14] A. W. Sandvik, L. Balents, and D. K. Campbell, Ground State Phases of the Half-Filled One-Dimensional Extended Hubbard Model, *Phys. Rev. Lett.* **92**, 236401 (2004).

[15] M. Tsuchiizu and A. Furusaki, Ground-state phase diagram of the one-dimensional half-filled extended Hubbard model, *Phys. Rev. B* **69**, 035103 (2004).

[16] K.-M. Tam, S.-W. Tsai, and D. K. Campbell, Functional Renormalization Group Analysis of the Half-Filled One-Dimensional Extended Hubbard Model, *Phys. Rev. Lett.* **96**, 036408 (2006).

[17] The model with random, rather than alternating, static distortions is often referred to as the binary alloy Hubbard Hamiltonian. The possibility of a Mott transition away from half filling has recently been discussed (see Ref. 15).

[18] S. S. Kancharla and E. Dagotto, Correlated Insulated Phase Suggests Bond Order between Band and Mott Insulators in Two Dimensions, *Phys. Rev. Lett.* **98**, 016402 (2007).

[19] N. Paris, K. Bouadim, F. Hebert, G. G. Batrouni, and R. T. Scalettar, Quantum Monte Carlo Study of an Interaction-Driven Band-Insulator–to–Metal Transition, *Phys. Rev. Lett.* **98**, 046403 (2007).

[20] K. Byczuk, M. Ulmke, and D. Vollhardt, Ferromagnetism and Metal-Insulator Transition in the Disordered Hubbard Model, *Phys. Rev. Lett.* **90**, 196403 (2003).

[21] K. Byczuk, W. Hofstetter, and D. Vollhardt, Mott-Hubbard metal-insulator transition at noninteger filling, *Phys. Rev. B* **69**, 045112 (2004).

[22] A. Garg, H. R. Krishnamurthy, and M. Randeria, Can Correlations Drive a Band Insulator Metallic?, *Phys. Rev. Lett.* **97**, 046403 (2006).

[23] D. Jaksch, C. Bruder, J. I. Cirac, C. W. Gardiner, and P. Zoller, Cold Bosonic Atoms in Optical Lattices, *Phys. Rev. Lett.* **81**, 3108 (1998).

[24] P. Buonsante and A. Vezzani, Phase diagram for ultracold bosons in optical lattices and superlattices, *Phys. Rev. A* **70**, 033608 (2004).

[25] P. Buonsante, V. Penna, and A. Vezzani, Fractional-filling loophole insulator domains for ultracold bosons in optical superlattices, *Phys. Rev. A* **70**, 061603(R) (2004).

[26] P. Buonsante and A. Vezzani, Cell strong-coupling perturbative approach to the phase diagram of ultracold bosons in optical superlattices, *Phys. Rev. A* **72**, 013614 (2005).

[27] V. G. Rousseau, M. Rigol, F. Hebert, D. P. Arovas, G. G. Batrouni, and R. T. Scalettar, Exact study of the one-dimensional boson Hubbard model with a superlattice potential, *Phys. Rev. B* **73**, 174516 (2006).

[28] N. R. Thomas, A. C. Wilson, and C. J. Foot, Double-well magnetic trap for Bose-Einstein condensates, *Phys. Rev. A* **65**, 063406 (2002).

[29] S. Friebel, C. DAndrea, J. Walz, M. Weitz, and T. W. Hänsch, CO_2-laser optical lattice with cold rubidium atoms, *Phys. Rev. A* **57**, R20 (1998).

[30] P. Ahmadi, V. Ramareddy, and G. S. Summy, Multiple micro-optical atom traps with a spherically aberrated laser beam, *New J. Phys.* **7**, 4 (2005).

[31] S. Peil, J. V. Porto, B. Laburthe Tolra, J. M. Obrecht, B. E. King, M. Subbotin, S. L. Rolston, and W. D. Phillips, Patterned loading of a Bose-Einstein condensate into an optical lattice, *Phys. Rev. A* **67**, 051603(R) (2003).

[32] N. Nagaosa and J. Takimoto, Theory of Neutral-Ionic Transition in Organic Crystals. I. Monte Carlo Simulation of Modified Hubbard Model, *J. Phys. Soc. Japan* **55**, 2735 (1986).

[33] T. Egami, S. Ishihara, and M. Tachiki, Lattice Effect of Strong Electron Correlation: Implication for Ferroelectricity and Superconductivity, *Science* **261**, 1307 (1993).

[34] J. Hubbard and J. B. Torrance, Model of the Neutral-Ionic Phase Transformation, *Phys. Rev. Lett.* **47**, 1750 (1981).

[35] G. Ortiz and R. M. Martin, Macroscopic polarization as a geometric quantum phase: Many-body formulation, *Phys. Rev. B* **49**, 14202 (1994).

[36] R. Resta and S. Sorella, Many-Body Effects on Polarization and Dynamical Charges in a Partly Covalent Polar Insulator, *Phys. Rev. Lett.* **74**, 4738 (1995).

[37] R. Resta and S. Sorella, Electron Localization in the Insulating State, *Phys. Rev. Lett.* **82**, 370 (1999).

[38] M. Fabrizio, A. O. Gogolin, and A. A. Nersesyan, From Band Insulator to Mott Insulator in One Dimension, *Phys. Rev. Lett.* **83**, 2014 (1999).

[39] T. Wilkens and R. M. Martin, Quantum Monte Carlo study of the one-dimensional ionic Hubbard model, *Phys. Rev. B* **63**, 235108 (2001).

[40] C. D. Batista and A. A. Aligia, Exact Bond Ordered Ground State for the Transition between the Band and the Mott Insulator, *Phys. Rev. Lett.* **92**, 246405 (2004).

[41] Y. Z. Zhang, C. Q. Wu, and H. Q. Lin, Bond order wave and energy gap in a one-dimensional bond-charge attraction model, *Phys. Rev. B* **66**, 035115 (2002).

[42] Y. Z. Zhang, C. Q. Wu, and H. Q. Lin, Inducement of bond-order wave due to electron correlation in one dimension, *Phys. Rev. B* **67**, 205109 (2003).

[43] J. Riera and D. Poilblanc, Coexistence of charge-density waves, bond-order waves, and spin-density waves in quasi-one-dimensional charge-transfer salts, *Phys. Rev. B* **62**, R16243 (2000).

[44] S. Sil and B. Bhattacharyya, Effect of electron-phonon interaction on a one-dimensional correlated electron system, *Phys. Rev. B* **54**, 14349 (1996).

[45] J. E. Hirsch, R. L. Sugar, D. J. Scalapino, and R. Blankenbecler, Monte Carlo simulations of one-dimensional fermion systems, *Phys. Rev. B* **26**, 5033 (1982).

[46] H. F. Trotter, On the product of semi-groups of operators, *Proc. Am. Math. Soc.* **10**, 545 (1959).

[47] M. Suzuki, General correction theorems on decomposition formulae of exponential operators and extrapolation methods for quantum Monte Carlo simulations, *Phys. Lett. A* **113**, 299 (1985).

[48] R. M. Fye, New results on Trotter-like approximations, *Phys. Rev. B* **33**, 6271 (1986).

[49] R. M. Fye and R. T. Scalettar, Calculation of specific heat and susceptibilities with the use of the Trotter approximation, *Phys. Rev. B* **36**, 3833 (1987).

[50] M. Barma and B. S. Shastry, Classical equivalents of one-dimensional quantum-mechanical systems, *Phys. Rev. B* **18**, 3351 (1978).

[51] A. W. Sandvik and J. Kurkijärvi, Quantum Monte Carlo simulation method for spin systems, *Phys. Rev. B* **43**, 5950 (1991).

[52] A. W. Sandvik, A generalization of Handscomb's quantum Monte Carlo scheme-application to the 1D Hubbard model, *J. Phys. A* **25**, 3667 (1992).

[53] A. W. Sandvik, Stochastic series expansion method with operator-loop update, *Phys. Rev. B* **59**, R14157 (1999).

[54] N. V. Prokof'ev, B. V. Svistunov, and I. S. Tupitsyn, Exact, complete, and universal continuous-time worldline Monte Carlo approach to the statistics of discrete quantum systems, *J. Exp. Theor. Phys.* **87**, 310 (1998).

[55] In addition to moves that change a phonon coordinate at a single space-time point, we also include moves that modify the phonon coordinates at all imaginary times for a given spatial site.

[56] E. Jeckelmann, Ground-State Phase Diagram of a Half-Filled One-Dimensional Extended Hubbard Model, *Phys. Rev. Lett.* **89**, 236401 (2002).

[57] A. W. Sandvik, P. Sengupta, and D. K. Campbell, Comment on "Ground-State Phase Diagram of a Half-Filled One-Dimensional Extended Hubbard Model", *Phys. Rev. Lett.* **91**, 089701 (2003).

[58] E. Jeckelmann, Jeckelmann Replies:, *Phys. Rev. Lett.* **91**, 089702 (2003).

Chapter 4

Quantum Monte Carlo study of the visibility of one-dimensional Bose-Fermi mixtures

The work described in this Chapter was done in collaboration with Valery Rousseau and Richard Scalettar. It has been published in Reference 1.

4.1 Introduction

It has been widely suggested that the strong correlations responsible for magnetism, superconductivity, and the metal-insulator transition in the solid state can be studied via ultracold optically trapped atoms. Indeed, this idea has been successfully realized in the context of both bosonic and fermionic atoms. In the former case, the transition between condensed (superfluid) and insulating phases was demonstrated through the evolution of the interference pattern after the release and expansion of the gas [2]. Initial studies focused on the height [2] and width [3] of the central interference peak, with later work looking at the visibility $\mathcal{V}$, which measures the difference between the maxima and minima of the momentum distribution function $S(\mathbf{k})$ [4–6]. Interesting

"kinks" are observed in $\mathcal{V}$ which are associated with the redistribution of the density as the superfluid shells evolve into insulating regions [7, 8]. For trapped fermions [9–13], Mott phases could also form [14–16], however, without a signal in $S(\mathbf{k})$. Instead, the evolution of the kinetic energy has been proposed as a means to pinpoint the transition [17].

Attention has turned at present to multicomponent systems, which offer a rich set of phenomena including Bose-Einstein condensation (BEC)-BCS crossover for two attractive fermionic species and Fulde-Ferrell-Larkin-Ovchinnikov phases in situations with two imbalanced fermion populations. Two recent experimental papers report the effect of the addition of fermionic ^{40}K atoms on the visibility of bosonic ^{87}Rb in a three-dimensional trap [18, 19]. The basic result is a decrease in the bosonic visibility $\mathcal{V}_b$ driven by the fermion admixture. A large number of qualitative explanations has been put forth for this phenomenon, including the localization of the bosons by the random fermionic impurities, the segmentation of the bosonic superfluid, the adiabatic heating of the bosonic cloud when the lattice depth is increased in the presence of the two species, an enhanced bosonic mass due to the coupling to the fermions, and the growth of Mott-insulating regions. A fundamental difficulty is that exact quantum Monte Carlo (QMC) calculations show an increase in $\mathcal{V}_b$ [20], in disagreement with experiment. In this chapter we resolve this issue.

The behavior of Bose-Fermi mixtures has attracted considerable theoretical attention. The Hamiltonian was derived and its parameters linked to experimental quantities by Albus *et al.* [21]. The equilibrium phase diagram has been studied using mean-field theory and Gutzwiller decoupling [21–23], perturbation theory [22], dynamical mean-field theory (DMFT) [23], exact diagonalization [24], quantum Monte Carlo methods [20, 25–27], and density matrix renormalization group (DMRG) [20, 28]. The results of these studies include the observation of Mott-insulating phases at "double half-filling", anticorrelated winding of the two species of quantum parti-

cles, molecule formation, and precise determination of the exponents characterizing correlation function decay in the different phases. The behavior of the visibility was addressed by Pollet *et al.* [20], who find interesting nonmonotonic structures with fermion density. However, $\mathcal{V}_b$ is always increased relative to the pure case [29].

In this chapter we explore the visibility of Bose-Fermi mixtures in one dimension using QMC simulations with the canonical worm algorithm [30–32]. While previous QMC studies have reported a growth of $\mathcal{V}_b$, we show that a significant reduction, such as seen experimentally, is also possible without invoking temperature effects [20]. The enhancement (reduction) of $\mathcal{V}_b$ caused by the disruption (inducement) of the bosonic Mott-insulator phase by the boson-fermion interactions. $\mathcal{V}_b$ also exhibits kinks reminiscent of those in the pure boson case. In the subsequent sections we write down the Hamiltonian and observables and briefly discuss the QMC algorithm. We then present the evolution of $\mathcal{V}_b$ with fermion concentration, its interpretation in terms of the bosonic density profiles, and evidence for the formation of a molecular superfluid in the trap center.

4.2 Model and Computational Methods

The one-dimensional (1D) Bose-Fermi Hubbard Hamiltonian is [21]

$$\begin{aligned} H = & -t_b \sum_j (\hat{b}_j^\dagger \hat{b}_{j+1} + \text{h.c.}) - t_f \sum_j (\hat{c}_j^\dagger \hat{c}_{j+1} + \text{h.c.}) \\ & + W \sum_i x_i^2 (\hat{n}_b^{(i)} + \hat{n}_f^{(i)}) + \frac{U_{bb}}{2} \sum_i \hat{n}_b^{(i)} (\hat{n}_b^{(i)} - 1) + U_{bf} \sum_i \hat{n}_b^{(i)} \hat{n}_f^{(i)}, \end{aligned} \tag{4.1}$$

where $\hat{b}_j$ ($\hat{b}_j^\dagger$) and $\hat{c}_j$ ($\hat{c}_j^\dagger$) are the annihilation (creation) operators of the bosons and (spin-polarized) fermions at lattice site j, respectively, and $\hat{n}_b^{(i)} = \hat{b}_i^\dagger \hat{b}_i$, $\hat{n}_f^{(i)} = \hat{c}_i^\dagger \hat{c}_i$ are the corresponding number operators. The first two terms of Eq. (4.1) describe bosonic and fermionic nearest-neighbor hopping. The curvature of the trap is W, and

the coordinate of the jth site is given by $x_j = ja$, where a is the lattice constant. U_{bb} and U_{bf} are the on-site boson-boson and boson-fermion interactions. Here nearest-neighbor interactions are not considered as they are orders of magnitude smaller in strength. In this work we consider 80-site chains with the nearest-neighbor hopping set to be identical for fermions and bosons ($t_b = t_f = t = 1$) and trapping potential $W = 0.01t$.

In the canonical worm algorithm [30–32] employed in our calculation, operator expectation values are sampled through the introduction of open-ended world lines that extend over equal imaginary time into a path integral expression for the partition function. The properties we study include the kinetic, potential, and trap energies, the density profiles, and the visibility,

$$\mathcal{V} = \frac{S_{\max} - S_{\min}}{S_{\max} + S_{\min}} , \tag{4.2}$$

where $S_{\max}$ and $S_{\min}$ are the maximum and minimum values of momentum distribution function,

$$S(k) = \frac{1}{L} \sum_{j,l} \mathrm{e}^{ik(x_j - x_l)} \langle \hat{b}_j^\dagger \hat{b}_l \rangle. \tag{4.3}$$

4.3 Results

The enhanced visibilities with fermion concentration reported previously [20] are in contrast with the trend to reduced $\mathcal{V}_b$ measured experimentally [18, 19]. In Fig. 4.1, we see the origin of this effect in a system with 40 bosons: the visibility enhancement at large U_{bb} is caused by the destruction of the Mott phase at the trap center by the fermions. It is natural to conjecture that if $n_b^{(i)} < 1$ at the trap center the additional attraction due to the fermions could induce Mott-insulating behavior and reduce $\mathcal{V}$. In Fig. 4.2(a), we show that this expectation is correct. Here, we fix $U_{bb} = 12t$ and

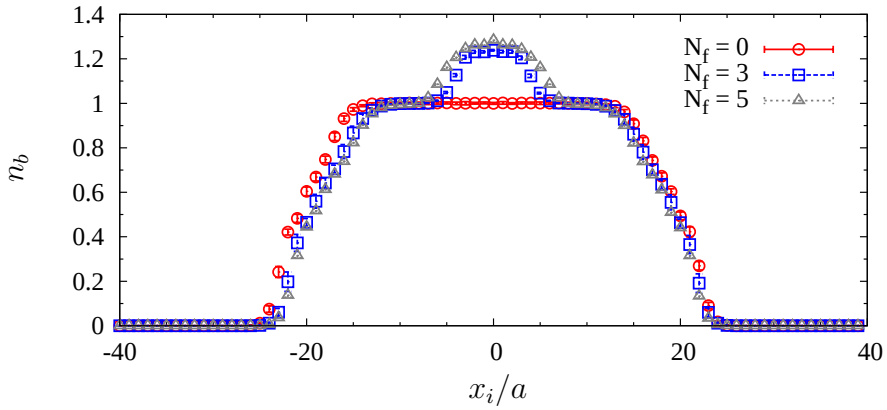

Figure 4.1: Comparison of the density profiles at $U_{bb} = 8.3t$ and $U_{bf} = -5.0t$ for $N_f = 0, 3, 5$ fermions on an 80-site chain with 40 bosons. The Mott insulator at the trap center for the pure bosonic case is destroyed by the addition of fermions. This drives the increase in the visibility.

increase N_b for both the pure case and for a system with fermion number fixed at $N_f = 9$ and boson-fermion interaction at $U_{bf} = -5t$. What we observe is that in a window where the boson central density is approaching $n_b^{(i)} = 1$ the bosonic visibility is decreased by the presence of the fermions. The cause is clear: if the bosons are poised just below Mott-insulating behavior, then the fermions can induce it. This is supported by a comparison of the density profiles in Fig. 4.2(b).

The primary mechanism through which fermions affect $\mathcal{V}_b$ is the local adjustment of the site energy and hence of the local bosonic density. This is an effect which occurs regardless of the dimensionality. Hence, we expect aspects of our conclusions to be relevant to experiments in higher dimension [20]. While we have shown a decreased visibility similar to that seen experimentally, the enhancement of visibility may be the more generic behavior in one dimension. In the one-dimensional "state diagram" of the purely bosonic case [33] the area of parameter space occupied by the phase with a Mott plateau of $n_b^{(i)} = 2$ is very narrow. Thus the prospect for the fermions to drive the system into this phase is limited.

In the case of a pure bosonic system [8], the change in visibility with the boson-boson interaction strength U_{bb} is not smooth, but is accompanied by "kinks." These

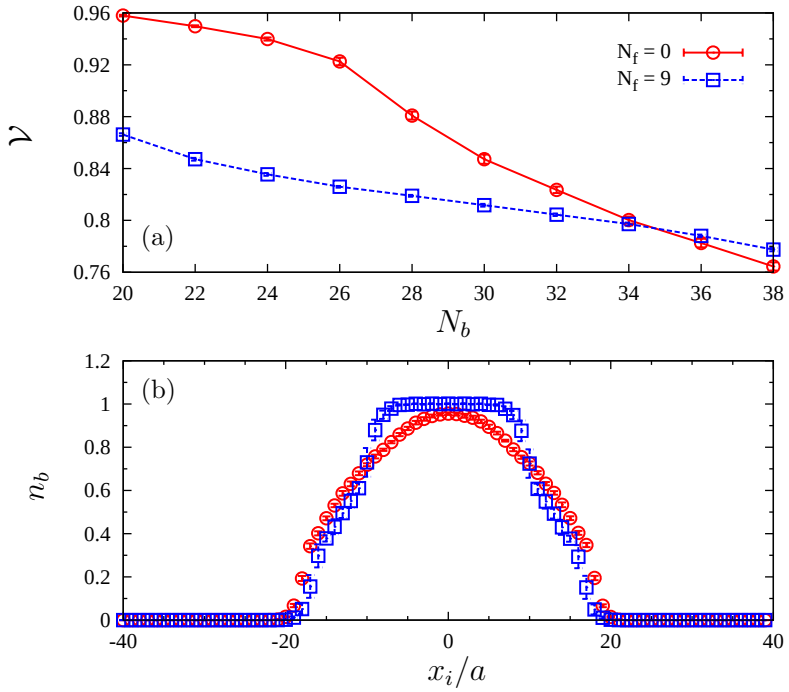

Figure 4.2: (a) Bosonic visibility $\mathcal{V}_b$ as a function of the number of bosons for $N_f = 0$ and 9 fermions with fixed $U_{bb} = 12.0t$ and $U_{bf} = -5.0t$. (b) Bosonic density profiles for $N_b = 26$ bosons and $N_f = 0, 9$ fermions. The addition of the fermions induces Mott-insulating behavior in the bosons. The key consequence is a decrease in $\mathcal{V}_b$ for $N_f = 9$ relative to $N_f = 0$, similar to that seen in the experiments.

kinks are associated with a freezing of the density profile when the transfer of the bosonic density from the trap center is interrupted by the formation of Mott insulator shoulders. In Fig. 4.3, the behavior of the visibilities and density profiles with U_{bb} in the presence of fermions is shown. $\mathcal{V}_b$ decreases with U_{bb} as the interaction reduces the quasicondensate fraction $S^b_{\max}$. Conversely, the interactions enhance $S^f_{\max}$ and $\mathcal{V}_f$ increases with U_{bb}. There are, however, additional kinks in the case when fermions are present whose origin we shall discuss below. Figure 4.4 helps to quantify this freezing by showing the evolution of the trap, interaction, and kinetic energies with U_{bb}. These energies exhibit a sequence of plateaus and rapid drops corresponding to the kink locations in Fig. 4.3.

Figure 4.5(a) compares the visibility evolution for the pure bosonic case ($N_f = 0$) with two different fermion numbers $N_f = 3$ and 5. For $N_f = 3$, the kink at lowest

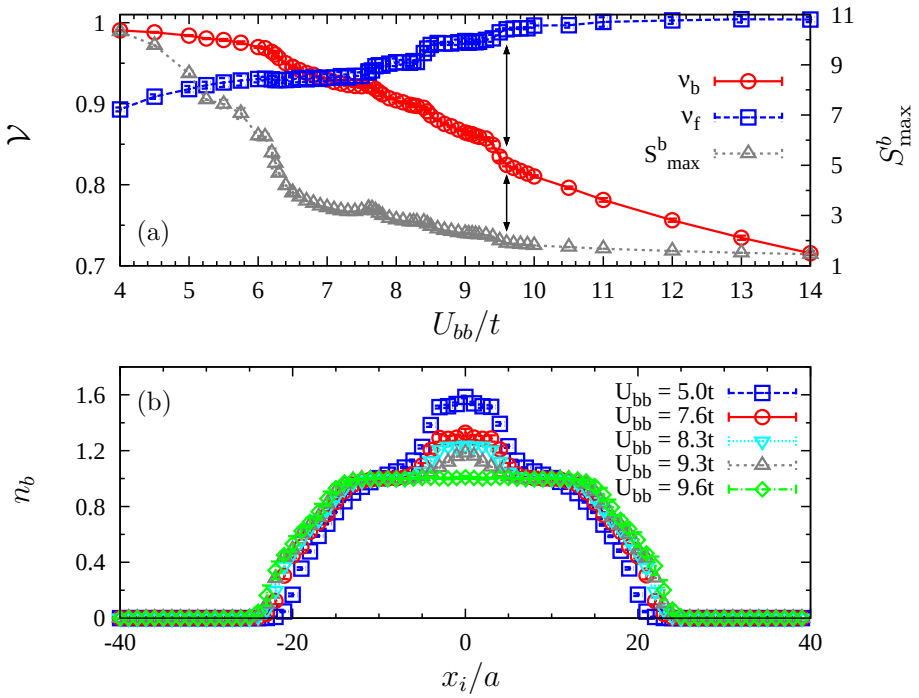

Figure 4.3: (a) Bosonic and fermionic visibilities and bosonic $S_{\max}$ as functions of U_{bb}/t for a system with 40 bosons, 3 fermions, and $U_{bf} = -5.0t$. The "plateau" regions where the rate of reduction of $\mathcal{V}$ is reduced are due to freezing of the density profiles (see text). The fast decrease after $U_{bb}/t \approx 9.3$ is due to the formation of a Mott-insulating region in the central core, which is fully formed and indicated by the arrow at $U_{bb}/t = 9.6$. (b) Boson density profiles at five different values of U_{bb}/t.

$U_{bb} = 6.1t$ is associated with the initial emergence of the Mott shoulders. This kink coincides with one in the pure bosonic case $N_f = 0$ because the shoulders form outside the regions occupied by the fermions at the trap center. For $N_f = 5$, the width of the fermion density is comparable to the size of the bosonic superfluid in the center of the trap, and the kink at $U_{bb} = 6.0t$ signifies a freezing of the bosonic density but not the formation of the Mott shoulders. Instead, the kink visible at $U_{bb} \approx 6.8t$ is responsible for the formation of the Mott shoulders. This shift to higher U_{bb} is expected since the attractive U_{bf} delays the transfer of bosonic density out of the center. Figures 4.5(b) and 4.5(c) compare the components of the energy. Each plateau signifies that the bosonic and fermionic densities are frozen over the range in U_{bb}. The sizes of the plateaus vary and the reason for this may be addressed in future

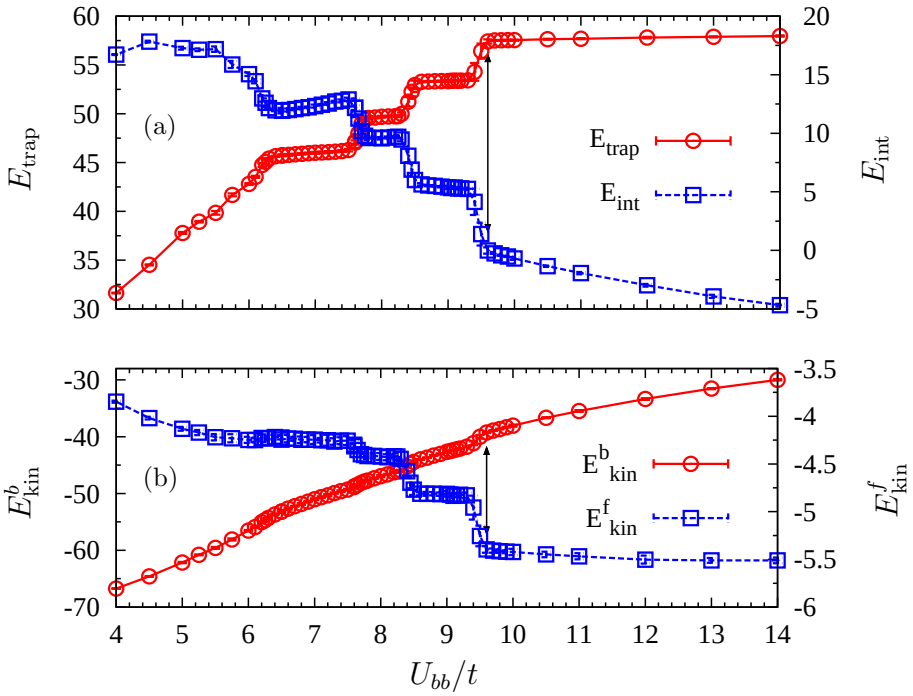

Figure 4.4: (a) Trapping ($E_{\rm trap}$) and interaction ($E_{\rm int}$) energies as functions of U_{bb}/t for the system of Fig. 4.3. (b) Bosonic ($E^b_{\rm kin}$) and fermionic ($E^f_{\rm kin}$) kinetic energies.

work. Past experiments [18, 19] did not have the resolution to exhibit the kinks we have seen in these simulations; however, they might be seen with improved accuracy.

We also note in Fig. 4.5 that the number of plateaus is directly related to the number of fermions in the Bose-Fermi mixture and that each plateau is roughly the same size, indicating that bound pairs of bosons and fermions are being destroyed as U_{bb} is increased. This conclusion is substantiated in Fig. 4.6, where we compare the bosonic density with the fermionic density. The fermionic density is offset by a constant to emphasize the near perfect overlap in the densities near the center of the trap, indicating that the trap center is populated by a molecular superfluid (MSF). Indeed, at the weakest coupling, Fig. 4.6(a), the fermion density precisely equals the excess boson density above the commensurate Mott value $n_b^{(i)} = 1$. When U_{bb} is increased, moving from one plateau to another in Fig. 4.5, the MSF region in the center of the trap shrinks. For the kink at highest U_{bb} ($\approx 9.8t$ for $N_f = 5$), the

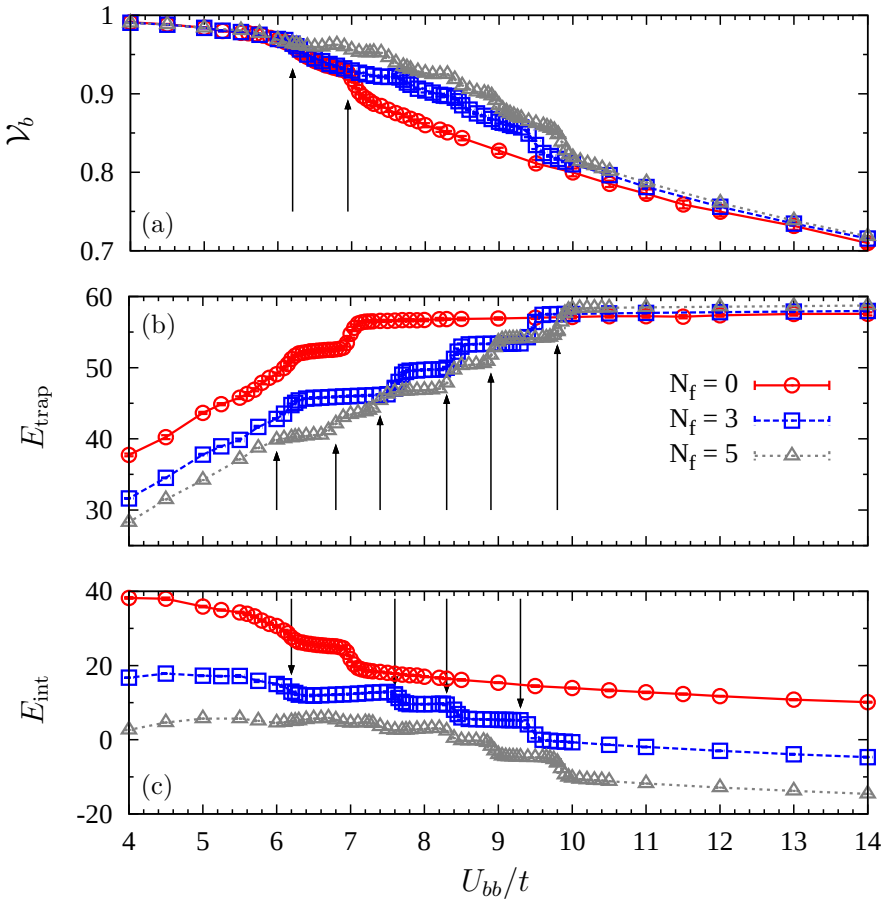

Figure 4.5: Comparison of (a) bosonic visibility $\mathcal{V}_b$, (b) the trapping energy, and (c) the interaction energy for $N_f = 0$, 3, and 5 fermions on an 80-site chain with 40 bosons and fixed $U_{bf} = -5.0t$. The arrows in panels (a), (c), and (b), respectively, denote the locations of the kinks (the onset of rapid change in energy and visibility) for $N_f = 0$, 3, and 5 fermions.

MSF region is destroyed, the bosonic density is a Mott insulator, and the fermionic visibility $\mathcal{V}_f \to 1$.

4.4 Summary

In summary, we have shown that the visibility of Bose-Fermi mixtures can be enhanced or reduced by the boson-fermion interactions depending on whether the bosonic density in the pure case is above or below commensuration. This result resolves a fundamental disagreement between experiment and QMC simulations. There are nu-

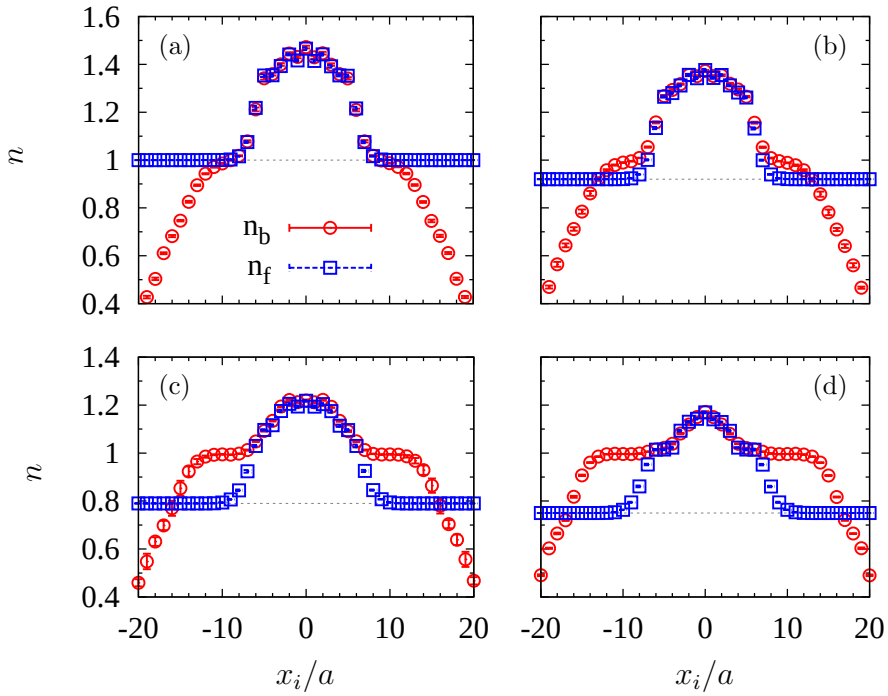

Figure 4.6: Bosonic and fermionic density profiles for (a) $U_{bb} = 6.3t$, (b) $U_{bb} = 7.2t$, (c) $U_{bb} = 8.6t$, and (d) $U_{bb} = 9.5t$ with 5 fermions, 40 bosons, and fixed $U_{bf} = -5.0t$. The fermionic density is offset and the dashed gray line indicates zero density. The densities match in the center of the trap, with the region of coincidence decreasing as U_{bb} increases.

merous kinks in the visibility and the different energies that result from freezing of the density profiles. While our bosonic component is sufficiently large so that our results are converged with respect to lattice size, the number of fermions is much smaller. It is possible that the kinks will merge together and be less easy to observe in a larger system. The density profiles near the kinks show direct evidence for a molecular superfluid in the center of the trap and that a larger U_{bb} is required to destroy the bound pairs with larger N_f and subsequently induce Mott-insulating behavior.

Acknowledgements

Supported under ARO Award W911NF0710576 with funds from the DARPA OLE Program, NSF PHY05-51164 (preprint NSF-KITP-07-195), with useful input from

T. Mavericks.

4.5 References

[1] C. N. Varney, V. G. Rousseau, and R. T. Scalettar, Quantum Monte Carlo study of the visibility of one-dimensional Bose-Fermi mixtures, *Phys. Rev. A* **77**, 041608(R) (2008).

[2] M. Greiner, O. Mandel, T. Esslinger, T. W. Hänsch, and I. Bloch, Quantum phase transition from a superfluid to a Mott insulator in a gas of ultracold atoms, *Nature* **415**, 39 (2002).

[3] T. Stöferle, H. Moritz, C. Schori, M. Köhl, and T. Esslinger, Transition from a Strongly Interacting 1D Superfluid to a Mott Insulator, *Phys. Rev. Lett.* **92**, 130403 (2004).

[4] F. Gerbier, A. Widera, S. Folling, O. Mandel, T. Gericke, and I. Bloch, Phase Coherence of an Atomic Mott Insulator, *Phys. Rev. Lett.* **95**, 050404 (2005).

[5] F. Gerbier, A. Widera, S. Fölling, O. Mandel, T. Gericke, and I. Bloch, Interference pattern and visibility of a Mott insulator, *Phys. Rev. A* **72**, 053606 (2005).

[6] R. B. Diener, Q. Zhou, H. Zhai, and T.-L. Ho, Criterion for Bosonic Superfluidity in an Optical Lattice, *Phys. Rev. Lett.* **98**, 180404 (2007).

[7] R. Roth and K. Burnett, Superfluidity and interference pattern of ultracold bosons in optical lattices, *Phys. Rev. A* **67**, 031602(R) (2003).

[8] P. Sengupta, M. Rigol, G. G. Batrouni, P. J. H. Denteneer, and R. T. Scalettar, Phase Coherence, Visibility, and the Superfluid–Mott-Insulator Transition on One-Dimensional Optical Lattices, *Phys. Rev. Lett.* **95**, 220402 (2005).

[9] G. Modugno, F. Ferlaino, R. Heidemann, G. Roati, and M. Inguscio, Production of a Fermi gas of atoms in an optical lattice, *Phys. Rev. A* **68**, 011601(R) (2003).

[10] H. Ott, E. de Mirandes, F. Ferlaino, G. Roati, G. Modugno, and M. Inguscio, Collisionally Induced Transport in Periodic Potentials, *Phys. Rev. Lett.* **92**, 160601 (2004).

[11] H. Ott, E. de Mirandes, F. Ferlaino, G. Roati, V. Türck, G. Modugno, and M. Inguscio, Radio Frequency Selective Addressing of Localized Atoms in a Periodic Potential, *Phys. Rev. Lett.* **93**, 120407 (2004).

[12] M. Köhl, H. Moritz, T. Stöferle, K. Günter, and T. Esslinger, Fermionic Atoms in a Three Dimensional Optical Lattice: Observing Fermi Surfaces, Dynamics, and Interactions, *Phys. Rev. Lett.* **94**, 080403 (2005).

[13] H. Moritz, T. Stöferle, K. Günter, M. Köhl, and T. Esslinger, Confinement Induced Molecules in a 1D Fermi Gas, *Phys. Rev. Lett.* **94**, 210401 (2005).

[14] M. Rigol, A. Muramatsu, G. G. Batrouni, and R. T. Scalettar, Local Quantum Criticality in Confined Fermions on Optical Lattices, *Phys. Rev. Lett.* **91**, 130403 (2003).

[15] M. Rigol and A. Muramatsu, Quantum Monte Carlo study of confined fermions in one-dimensional optical lattices, *Phys. Rev. A* **69**, 053612 (2004).

[16] M. Rigol and A. Muramatsu, Numerical simulations of strongly correlated fermions confined in 1D optical lattices, *Opt. Commun.* **243**, 33 (2004).

[17] M. Rigol, R. T. Scalettar, P. Sengupta, and G. G. Batrouni, Time-of-flight observables and the formation of Mott domains of fermions and bosons on optical lattices, *Phys. Rev. B* **73**, 121103 (2006).

[18] K. Günter, T. Stöferle, H. Moritz, M. Köhl, and T. Esslinger, Bose-Fermi Mixtures in a Three-Dimensional Optical Lattice, *Phys. Rev. Lett.* **96**, 180402 (2006).

[19] S. Ospelkaus, C. Ospelkaus, O. Wille, M. Succo, P. Ernst, K. Sengstock, and K. Bongs, Localization of Bosonic Atoms by Fermionic Impurities in a Three-Dimensional Optical Lattice, *Phys. Rev. Lett.* **96**, 180403 (2006).

[20] L. Pollet, C. Kollath, U. Schollwöck, and M. Troyer, Mixture of bosonic and spin-polarized fermionic atoms in an optical lattice, *Phys. Rev. A* **77**, 023608 (2008).

[21] A. Albus, F. Illuminati, and J. Eisert, Mixtures of bosonic and fermionic atoms in optical lattices, *Phys. Rev. A* **68**, 023606 (2003).

[22] M. Cramer, J. Eisert, and F. Illuminati, Inhomogeneous Atomic Bose-Fermi Mixtures in Cubic Lattices, *Phys. Rev. Lett.* **93**, 190405 (2004).

[23] I. Titvinidze, M. Snoek, and W. Hofstetter, Supersolid Bose-Fermi Mixtures in Optical Lattices, *Phys. Rev. Lett.* **100**, 100401 (2008).

[24] R. Roth and K. Burnett, Quantum phases of atomic boson-fermion mixtures in optical lattices, *Phys. Rev. A* **69**, 021601 (2004).

[25] L. Pollet, M. Troyer, K. Van Houcke, and S. M. A. Rombouts, Phase Diagram of Bose-Fermi Mixtures in One-Dimensional Optical Lattices, *Phys. Rev. Lett.* **96**, 190402 (2006).

[26] P. Sengupta and L. P. Pryadko, Quantum degenerate Bose-Fermi mixtures on one-dimensional optical lattices, *Phys. Rev. B* **75**, 132507 (2007).

[27] F. Hébert, F. Haudin, L. Pollet, and G. G. Batrouni, Mott insulators and correlated superfluids in ultracold Bose-Fermi mixtures, *Phys. Rev. A* **76**, 043619 (2007).

[28] A. Mering and M. Fleischhauer, One-dimensional Bose-Fermi-Hubbard model in the heavy-fermion limit, *Phys. Rev. A* **77**, 023601 (2008).

[29] For one set of parameters, $\mathcal{V}$ for non-zero N_f falls below the $N_f = 0$ value, but only when N_f exceed N_b. In addition, the decrease is less than ten percent.

[30] N. V. Prokof'ev, B. V. Svistunov, and I. S. Tupitsyn, Exact, complete, and universal continuous-time worldline Monte Carlo approach to the statistics of discrete quantum systems, *JETP* **87**, 310 (1998).

[31] S. M. A. Rombouts, K. Van Houcke, and L. Pollet, Loop Updates for Quantum Monte Carlo Simulations in the Canonical Ensemble, *Phys. Rev. Lett.* **96**, 180603 (2006).

[32] K. Van Houcke, S. M. A. Rombouts, and L. Pollet, Quantum Monte Carlo simulation in the canonical ensemble at finite temperature, *Phys. Rev. E* **73**, 056703 (2006).

[33] G. G. Batrouni, V. Rousseau, R. T. Scalettar, M. Rigol, A. Muramatsu, P. J. H. Denteneer, and M. Troyer, Mott Domains of Bosons Confined on Optical Lattices, *Phys. Rev. Lett.* **89**, 117203 (2002).

Chapter 5

Quantum Monte Carlo study of the two-dimensional fermion Hubbard model

The work described in this Chapter was done in collaboration with Simone Chiesa, Che-Rung Lee, Zhaojun Bai, Mark Jarrell, and Richard Scalettar. It has been published in Reference 1.

5.1 Introduction

Originally introduced to explain magnetism and metal-insulator transitions in solids with strong electronic correlations and narrow energy bands [2–6], the underlying physics of the fermion Hubbard Hamiltonian [7–10] remains a topic of considerable interest. In two dimensions, when the lattice is doped away from half-filling, do the fermions condense into a superconducting state? If so, what is the symmetry of the pairing order parameter [11–15]? Do charge inhomogeneities (stripes and checkerboards) emerge, and what is their interplay with magnetic and superconducting order [16–19]?

In contrast to this uncertainty concerning the properties of the doped lattice, the qualitative behavior at half-filling (one fermion per site) is much more well understood. The interaction strength U causes both the development of long-range antiferromagnetic order (LRAFO) and insulating behavior. Even so, there are still some remaining open fundamental questions, for example, in the precise way in which the model evolves from the weak-coupling to strong-coupling limits, especially in two dimensions, as we explain below.

At weak-coupling, one pictures the insulating behavior to arise from a Fermi-surface instability which drives LRAFO and a gap in the quasiparticle density of states. On the other hand, at strong coupling the insulating behavior is caused by Mott physics and the suppression of electron mobility to avoid double occupancy. These points of view are clearly linked, however, since for large U/t the Hubbard Hamiltonian has well-defined local moments and maps onto the antiferromagnetic Heisenberg model with exchange constant $J = 4t^2/U$ [20].

Developing an analytic theory which bridges these viewpoints quantitatively is problematic. Hartree-Fock (HF) theory provides one simple point of view, but predicts LRAFO at finite temperatures in two dimensions, in violation of the Mermin-Wagner theorem. In fact, even in higher dimension when the Néel tempertaure T_{N} can be nonzero, HF theory predicts $T_{\mathrm{N}} \propto U$ instead of the correct $T_{\mathrm{N}} \propto J = 4t^2/U$. Sophisticated approaches such as the self-consistent renormalized theory [21, 22], the fluctuation-exchange approximation [23], and two-particle self-consistent theory [24] obey the Mermin-Wagner theorem and provide a good description of the Hubbard Hamiltonian at weak-coupling, but fail for large U/t. A recent approach [25] based on the mapping to the nonlinear sigma model [26] has made some progress in connecting the two regimes.

The need to pin down the behavior of the two-dimensional (2D) half-filled Hubbard model more quantititively, in a way which links the weak-coupling and strong-

coupling limits, is particularly germane at present with the achievement of cooling and quantum degeneracy in ultracold gases of fermionic atoms [27–32]. Such systems offer the prospect of acting as an "optical lattice emulator" (OLE) of the fermion Hubbard model, allowing a precise comparison of experimental and theoretical phase diagrams which is difficult in the solid state, where the (single band) Hubbard Hamiltonian provides only a rather approximate depiction of the full complexity of the atomic orbitals. Obviously, the achievement of this goal is one which requires accurate computations. A particular issue in the field of OLE concerns whether the temperature dependence of the double occupancy rate changes sign during the course of the evolution from weak to strong coupling [33].

It is the intent of this chapter to present considerably improved results for the effective bandwidth, momentum distribution, and magnetic correlations of the square lattice fermion Hubbard Hamiltonian. We will employ the determinant quantum Monte Carlo (DQMC) method, which provides an approximation-free solution of the model, on lattices large enough to use finite-size scaling to, for example, reliably extract the antiferromagnetic order parameter as a function of interaction strength. There is a considerable existing body of QMC studies of the two-dimensional half-filled Hubbard model, both on finite lattices and in infinite dimension. A partial list includes Refs. 14, 19, and 34–41.

5.2 Model and Computational Methods

The fermion Hubbard Hamiltonian,

$$H = -t \sum_{\langle \mathbf{i}\,\mathbf{j}\rangle\sigma} \left(c^{\dagger}_{\mathbf{j}\sigma} c_{\mathbf{i}\sigma} + c^{\dagger}_{\mathbf{i}\sigma} c_{\mathbf{j}\sigma} \right) + U \sum_{\mathbf{i}} \left(n_{\mathbf{i}\uparrow} - \frac{1}{2} \right) \left(n_{\mathbf{i}\downarrow} - \frac{1}{2} \right) - \mu \sum_{\mathbf{i}\sigma} n_{\mathbf{i}\sigma} \,, \qquad (5.1)$$

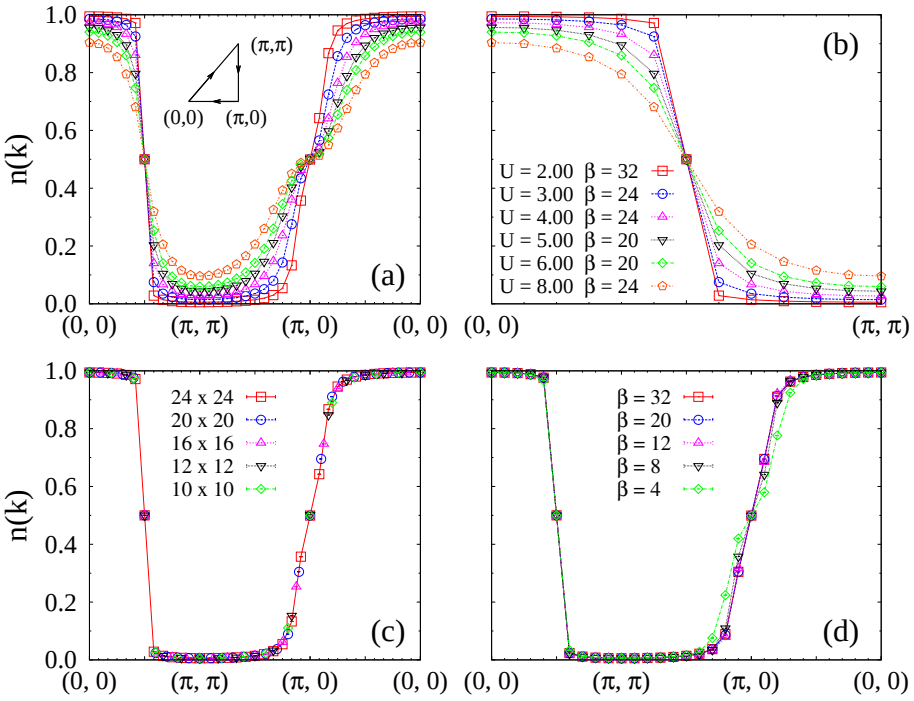

Figure 5.1: [(a) and (b)] The momentum distribution, Eq. (5.2), is shown for interaction strengths U ranging from $U = 2t$ (one quarter the bandwidth) to $U = W = 8t$. A sharp Fermi surface is seen at weak-coupling as the momentum cuts across the Fermi surface at $\mathbf{k} = (\pi/2, \pi/2)$. Larger U broadens $n(\mathbf{k})$ considerably. The occupation becomes substantial outside the nominal Fermi surface. Panel (a) shows the full BZ, while panel (b) provides higher resolution for the portion of the cut perpendicular to the Fermi surface at $(\pi/2, \pi/2)$. (c) At $U = 2t$ and $\beta t = 32$, $n(\mathbf{k})$ has only a weak lattice size dependence, apart from the better resolution as L increases. (d) For $U = 2t$ on a 20×20 lattice, $n(\mathbf{k})$ is converged to its low temperature value once $T < t/8$. (By contrast, the spin correlations reach their ground state values only at considerably lower T.)

describes a set of itinerant electrons, represented by $c_{\mathbf{j}\sigma}(c^\dagger_{\mathbf{j}\sigma})$, the annihilation (creation) operators at lattice site $\mathbf{j}$ and spin σ. The corresponding number operator $n_{\mathbf{j}\sigma} = c^\dagger_{\mathbf{j}\sigma} c_{\mathbf{j}\sigma}$. The first term represents the hopping (kinetic energy) of the electrons. We will choose the parameter $t = 1$ to set our unit of energy. The non-interacting dispersion relation is $\varepsilon(\mathbf{k}) = -2t(\cos k_x + \cos k_y)$ and has bandwidth $W = 8t$. U is the on-site repulsion of spin-up and spin-down electrons occupying the same lattice site, and μ is the chemical potential which controls the particle density. We will mostly be interested in the properties of the model on $N = L \times L$ square lattices at half-filling

(the number of particles is equal to the number of lattice sites) which occurs at $\mu = 0$ with our particle-hole symmetric choice of the representation of the interaction term.

We will also focus exclusively on the case of the square lattice. This particular geometry has several interesting features. The half-filled square lattice Fermi surface exhibits perfect nesting, and the density of states is (logarithmically) divergent. As a consequence, the antiferromagnetic and insulating transitions occur immediately for any nonzero value of the interaction strength U, instead of requiring a finite degree of correlation, as is more generically the case.

Our DQMC algorithm is based on Ref. 42 and has been refined by including "global moves" to improve ergodicity [43] and "delayed updating" of the fermion Green's function [44, 45], which increases the efficiency of the linear algebra. Details concerning this new code are available at Ref. 46. Some other approaches to fermion Hubbard model simulations are contained in Refs. 40 and 47–49.

5.3 Single Particle Properties

We begin by showing single-particle properties. The momentum distribution $n(\mathbf{k}) = \frac{1}{2}\sum_\sigma \langle c^\dagger_{\mathbf{k}\sigma} c_{\mathbf{k}\sigma}\rangle$ is obtained directly in DQMC via Fourier transform of the equal-time Green's function $G_{\mathbf{ji}} = \langle c_{\mathbf{j}\sigma} c^\dagger_{\mathbf{i}\sigma}\rangle$

$$n(\mathbf{k}) = 1 - \frac{1}{2N}\sum_{\mathbf{i},\mathbf{j},\sigma} e^{i\mathbf{k}\cdot(\mathbf{j}-\mathbf{i})}\,\langle c_{\mathbf{j}\sigma} c^\dagger_{\mathbf{i}\sigma}\rangle \ . \tag{5.2}$$

At $U = 0$ and at half-filling, $n(\mathbf{k}) = 1(0)$ inside (outside) a square with vertices $(\pi, 0)$, $(0, \pi)$, $(-\pi, 0)$, and $(0, -\pi)$ within the Brillouin zone (BZ). In Fig. 5.1(a), we show $n(\mathbf{k})$ around the irreducible part of the BZ, while Fig. 5.1(b) focuses on the region near the Fermi-surface point $(\pi/2, \pi/2)$. Interactions broaden the $U = 0$ Fermi surface considerably. Figure 5.1(c) shows that data for different lattice sizes fall on the same curve. Smearing due to finite temperature effects is seen in Fig. 5.1(d) to be small

below $T = t/8$ ($\beta t = 8$).

Recent optical lattice experiments [30] have imaged this Fermi surface for a three-dimensional cloud of fermionic ^{40}K atoms prepared in a balanced mixture of two hyperfine states which act as the Hubbard Hamiltonian spin degree of freedom. In Fig. 5.2 we show a sequence of color contour plots for different densities at weak and intermediate couplings, $U/t = 2, 4$. As in the experiments, and in agreement with Fig. 5.1, the Fermi surface may still be clearly discerned, and evolves from a circular topology at low densities into the rotated square as the BZ boundaries are approached at half-filling. Because of the sign problem [50, 51] which occurs in the doped system, the temperatures shown in the figure are rather higher than those used in Fig. 5.1 at half-filling.

Another single-particle quantity of interest is the effective hopping,

$$\frac{t_{\text{eff}}}{t} = \frac{\langle c^\dagger_{\mathbf{j}+\hat{x}\,\sigma} c_{\mathbf{j}\,\sigma} + c^\dagger_{\mathbf{j}\,\sigma} c_{\mathbf{j}+\hat{x}\,\sigma} \rangle_U}{\langle c^\dagger_{\mathbf{j}+\hat{x}\,\sigma} c_{\mathbf{j}\,\sigma} + c^\dagger_{\mathbf{j}\,\sigma} c_{\mathbf{j}+\hat{x}\,\sigma} \rangle_{U=0}} , \tag{5.3}$$

which measures the ratio of the kinetic energy at finite U to its non-interacting value. As the electron correlations grow larger, hopping is increasingly inhibited, and t_{eff} is diminished. In Fig. 5.3, we show a plot of this ratio as a function of U for a 10×10 lattice. Note that despite the insulating nature of the system, the effective hopping is nonzero and does not serve as an order parameter for the metal-insulator transition. Indeed, t_{eff} is responsible for the superexchange interaction which drives antiferromagnetic order. The effective hopping can be evaluated analytically at small and large U [11]. The DQMC data interpolates between these two limits.

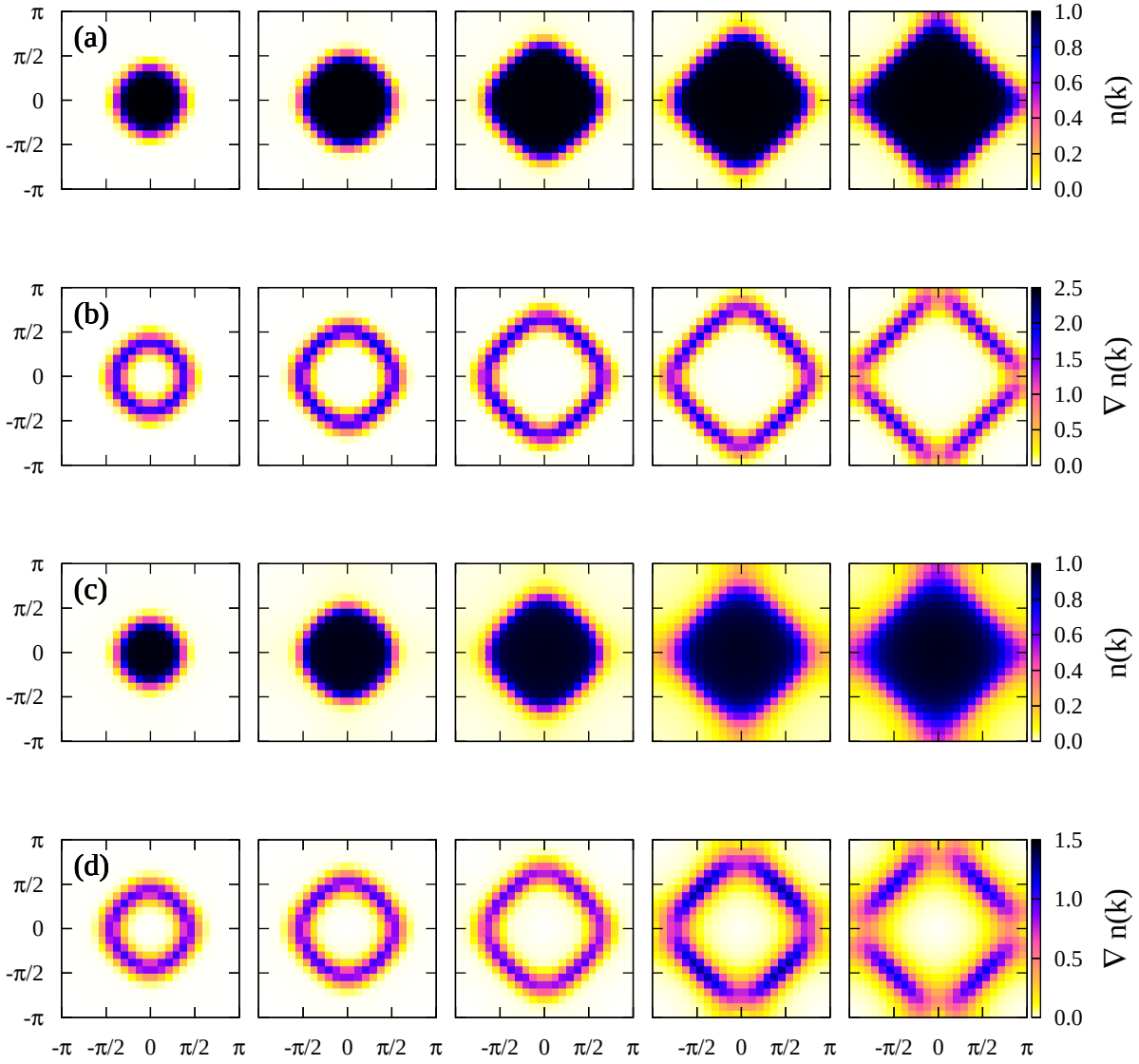

Figure 5.2: Color contour plot depiction of the momentum distribution $n(\mathbf{k})$ and its gradient $\nabla n(\mathbf{k})$. (a) Left to right, $n(\mathbf{k})$ at weak-coupling $U = 2t$ and fillings $\rho = 0.23$, 0.41, 0.61, 0.79, and 1.0. (b) $\nabla n(\mathbf{k})$ for the same parameters. [(c) and (d)] Intermediate coupling $U = 4t$ and fillings $\rho = 0.21$, 0.41, 0.59, 0.79 and 1.0. The increased breadth of the Fermi surface with interaction strength is evident. The lattice size $= 24 \times 24$ and inverse temperature $\beta t = 8$ except at $U = 4t$ and fillings $\rho = 0.59$ and 0.79, where the sign problem restricts the simulation to inverse temperatures $\beta t = 6$ and 4, respectively.

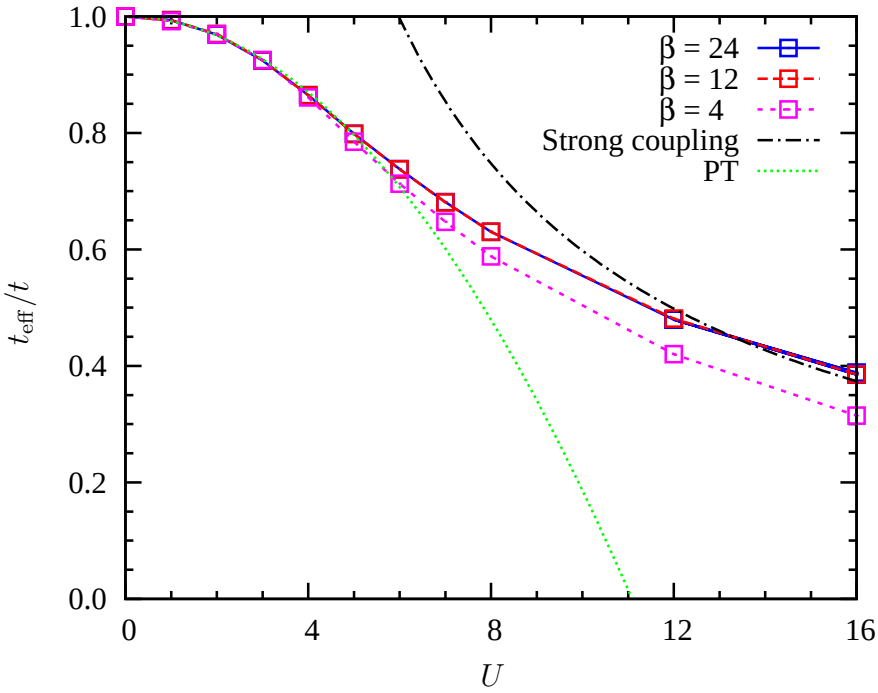

Figure 5.3: As the interaction energy U increases, the kinetic energy declines. Here we show $t_{\rm eff}/t$, the ratio between the expectation value of $\langle c^\dagger_{\mathbf{j}+\hat{x}\,\sigma} c_{\mathbf{j}\,\sigma}\rangle$ at U with its value at $U = 0$, for a 10×10 lattice. Strong-coupling and perturbative graphs are also shown for $\beta t = 12$.

5.4 Magnetic Correlations

We turn now to two-particle properties, focusing on the magnetic behavior. The real-space spin-spin correlation function is defined as

$$C(\mathbf{l}) = \langle (n_{\mathbf{j}+\mathbf{l}\uparrow} - n_{\mathbf{j}+\mathbf{l}\downarrow})(n_{\mathbf{j}\uparrow} - n_{\mathbf{j}\downarrow})\rangle \tag{5.4}$$

and measures the extent to which the z component of spin on site $\mathbf{j}$ aligns with that on a site a distance $\mathbf{l}$ away. Although defined in Eq. (5.4) using the z direction, $C(\mathbf{l})$ is rotationally invariant and in fact, we measure all three components to monitor ergodicity in our simulations and average over all directions to provide an improved estimator for the magnetic properties.

The local moment $\langle m^2\rangle = C(0,0) = \langle (n_{\mathbf{j}\uparrow} - n_{\mathbf{j}\downarrow})^2\rangle$ is the zero separation value

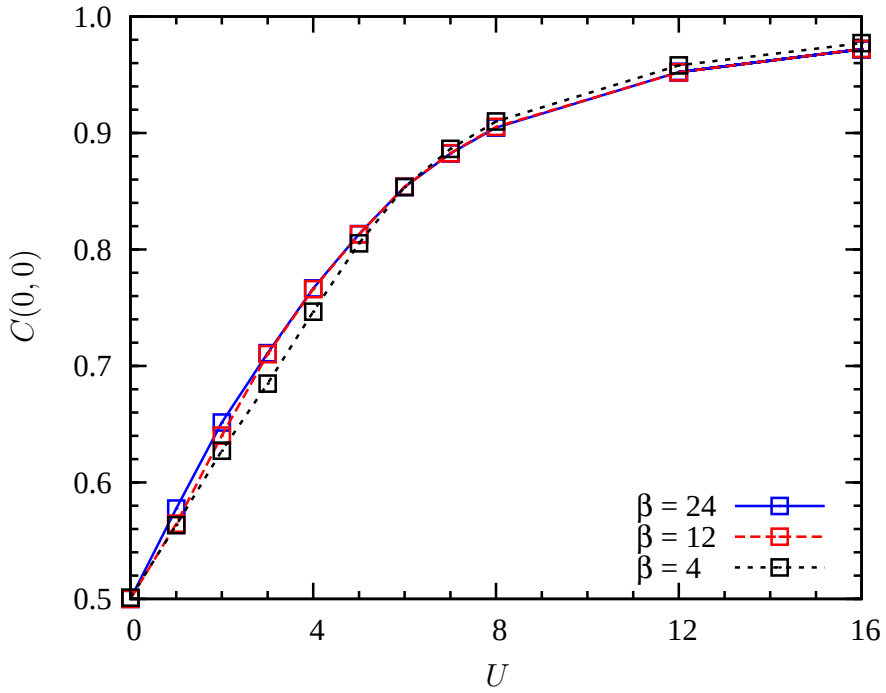

Figure 5.4: The local moment $\langle m^2 \rangle$ is the zero spatial separation value of the spin-spin correlation function $C(\mathbf{l} = (0,0))$. At weak-coupling $\langle m^2 \rangle = \frac{1}{2}$. As the interaction energy U increases, $\langle m^2 \rangle$ approaches 1, indicating the complete absence of double occupancy and a well-formed moment on each site.

of the spin-spin correlation function. The singly occupied states $|\uparrow\rangle$ and $|\downarrow\rangle$ have $\langle m^2 \rangle = 1$ while the empty and doubly occupied ones $|0\rangle$ and $|\uparrow\downarrow\rangle$, have $\langle m^2 \rangle = 0$. In the non-interacting limit, at half-filling, each of the four possible site configurations is equally likely. Hence the average moment $\langle m^2 \rangle = \frac{1}{2}$.

The on-site repulsion U suppresses the doubly occupied configuration and hence also the empty one, if the total occupation is fixed at one fermion per site. Ultimately, charge fluctuations are completely eliminated, $\langle m^2 \rangle \to 1$ and the Hubbard model maps onto the spin-$\frac{1}{2}$ Heisenberg Hamiltonian. This is illustrated in Fig. 5.4 for a 10×10 lattice. By the time $U = W = 8t$, the local moment has attained 90% of its full value. Thermal fluctuations also inhibit local moment formation but the data shown for different temperatures in Fig. 5.4 indicate they are mostly eliminated by the time T decreases below $t/12 = W/96$.

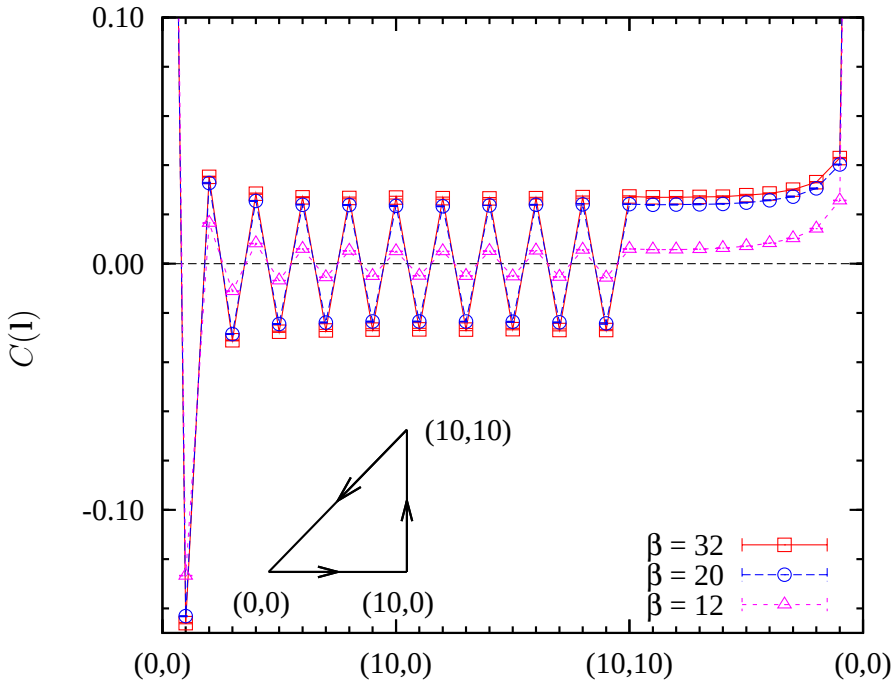

Figure 5.5: Comparison of the equal-time spin-spin correlation function $C(\mathbf{l})$ on a 20×20 lattice with $\langle n \rangle = 1$ and $U = 2t$ for inverse temperatures $\beta t = 12, 20$, and 32. The horizontal axis follows the triangular path on the lattice shown in the inset. Anti-ferromagnetic correlations are present for all temperatures, and saturation is visible at $\beta t = 32$.

Local moments provide an intuitive picture of the onset of long-range correlation in the strong-coupling regime. They first form on the temperature scale U, which acts to eliminate double occupancy, and then, at yet lower T, they order via antiferromagnetic exchange interaction with $J = 4t^2/U$. In contrast with this situation, weak-coupling correlations are better described as arising from the instability of the Fermi gas against formation of a spin-density wave, a peculiarity of the square lattice, suggesting an ordering temperature proportional to U.

Figure 5.5 shows the spin-spin correlation function in the latter regime ($U = 2$) for a 20×20 lattice at $\beta t = 12$, 20, and 32. The correlations extend over the entire lattice even at $\beta t = 12$, i.e., the correlation length has become comparable to the system size already at this temperature. The values of $C(\mathbf{l})$ continue to grow as T is increased further, saturating at $\beta t \simeq 32$. This observation disproves the commonly

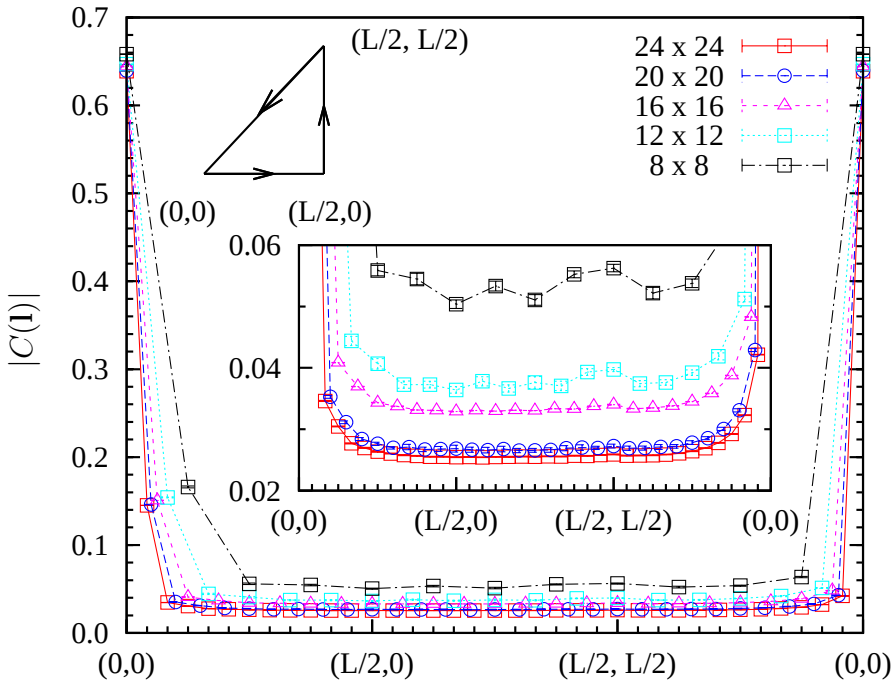

Figure 5.6: Comparison of the absolute value of the equal-time spin-spin correlation function $C(\mathbf{l})$ at $U = 2t$ and $\beta t = 32$ for $L \times L$ lattices with $L = 8, 12, 16, 20$, and 24. The inset is a close up view of the long-range correlations.

held idea that on finite clusters, the order parameter stop growing after the correlation length exceeds the linear size of the system. Such saturation happens at a much lower temperature, only after thermal fluctuations have been largely eliminated.

A comparison of $|C(\mathbf{l})|$ for $U = 2$ and different lattice sizes is given in Fig. 5.6, where data for $L = 8$ up to $L = 24$ are plotted and we have taken the absolute value to make the convergence with L clearer. We have fixed $\beta t = 32$ so the spin correlations have reached their asymptotic low-temperature values. As expected, the smallest lattice sizes (8×8) overestimate the tendency to order, with $|C(\mathbf{l})|$ significantly larger than values for larger L. However, by the time $L = 20$ the finite-size effects are small.

We next compare the spin-spin correlation function for various U at low temperatures on a 24×24 lattice in Fig. 5.7. Long-range order is present at all interaction strengths. For each U, we have chosen temperatures such that the ground state has been reached for this lattice size. Since statistical fluctuations increase signifi-

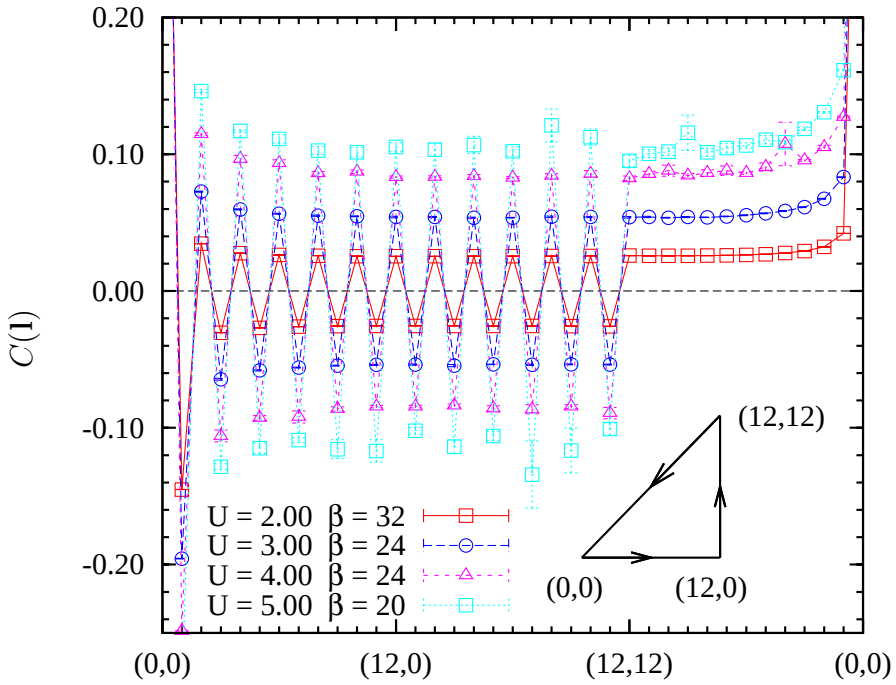

Figure 5.7: The equal-time spin-spin correlation function $C(\mathbf{l})$ on a 24×24 lattice with $\langle n \rangle = 1$. Data are shown for various U at low temperatures. Antiferromagnetic correlations are enhanced for larger values of U. The increase in statitstical fluctuations with interaction strength in the DQMC method is evident.

cantly with U and with β in DQMC, it is advantageous not to simulate unnecessarily cold systems. As discussed above, such temperature should increase with U in the weak-coupling regime and scale proportionally to $1/U$ in the strong-coupling one. We indeed find the highest saturation temperatures in the intermediate regime, at $U/t \simeq 4$.

The magnetic structure factor $S(\mathbf{k})$ is the Fourier transform of the real-space spin-spin correlation function $C(\mathbf{l})$,

$$S(\mathbf{k}) = \sum_{\mathbf{l}} e^{i\mathbf{k}\cdot\mathbf{l}} C(\mathbf{l}) \,, \tag{5.5}$$

where $S(\mathbf{k})$ is plotted in Fig. 5.8 as a function of $\mathbf{k}$ for several lattice sizes with $U = 2t$ and $\beta t = 32$. $S(\mathbf{k})$ is small and lattice size independent away from the ordering vector $\mathbf{k} = \mathbf{Q} \equiv (\pi, \pi)$. The sharp peak at $\mathbf{Q}$ emphasizes the antiferromagnetic nature of

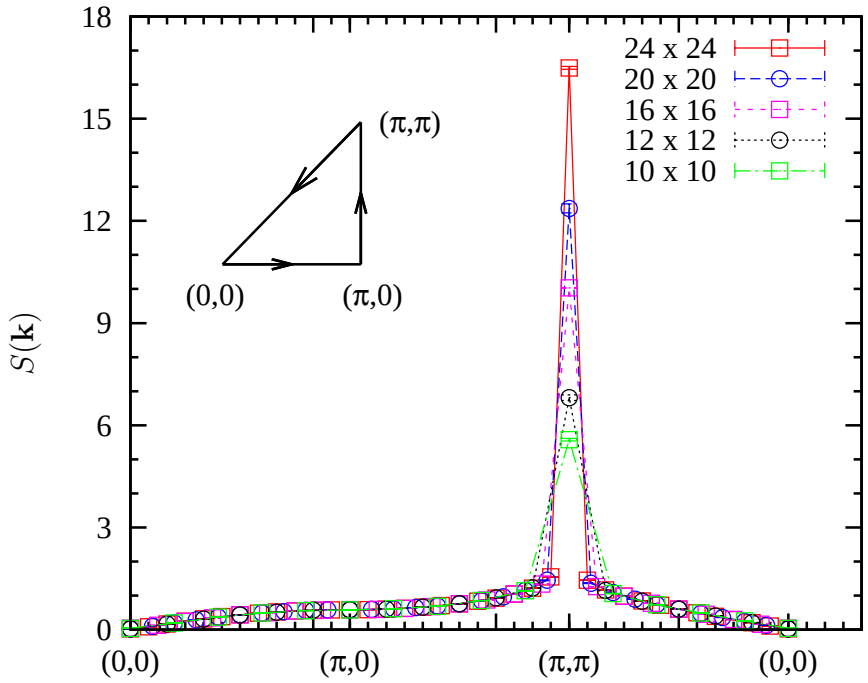

Figure 5.8: The magnetic structure factor $S(\mathbf{k})$ for $U = 2t$ and $\beta t = 32$. The horizontal axis traces out the triangular path shown in the inset. The function is sharply peaked at $\mathbf{k} = \mathbf{Q} \equiv (\pi, \pi)$.

the correlations on a half-filled lattice.

In order to understand the implications of the lattice size dependence at the ordering vector in Fig. 5.8, we show in Fig. 5.9 the antiferromagnetic structure factor for $U = 2t$ as a function of inverse temperature for various L. As expected, as L increases, a larger value of β is required to eliminate the low-lying spin-wave excitations and to saturate the structure factor to its ground state value.

It is seen from Eq. (5.5) that $S(\mathbf{Q})$ will grow linearly with the number of sites $N = L^2$ if there is long range antiferromagnetic order. Huse[52] has used spin-wave theory to work out the first correction to this scaling,

$$\frac{S(\pi,\pi)}{L^2} = \frac{m_{\rm af}^2}{3} + \frac{a}{L}\,. \tag{5.6}$$

Here $m_{\rm af}$ is the antiferromagnetic order parameter. $m_{\rm af}$ can also be extracted from

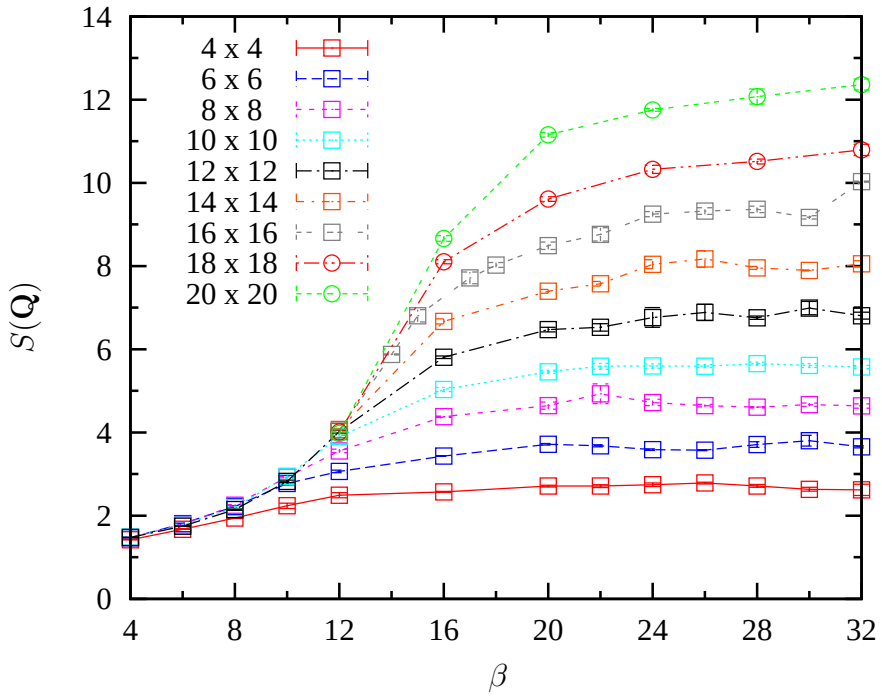

Figure 5.9: The antiferromagnetic structure factor $S(\mathbf{Q})$ as a function of inverse temperature at $U = 2t$ for $L \times L$ lattices with $L = 4, 6, 8, 10, 12, 14, 16, 18$, and 20.

the spin-spin correlation function between the two most distant points on a lattice, $C(L/2, L/2)$, with a similar spin-wave theory correction,

$$C(L/2, L/2) = \frac{m_{\mathrm{af}}^2}{3} + \frac{b}{L}\,. \tag{5.7}$$

We expect that the correction $b < a$ since the structure factor includes spin correlations at short distances which markedly exceed m_{af}^2, in addition to the finite lattice effects at larger length scales. For similar reasons S is expected to show larger corrections to the asymptotic $1/L$ scaling behavior than C. Part of the origin of these corrections is trivial and evident from Fig. 5.6: S is the average of quantities as different as $C(0,0)$ and $C(L/2, L/2)$. In the large L limit, S and its $1/L$ finite-size error are dominated by the contribution of the large distance correlations but for small L

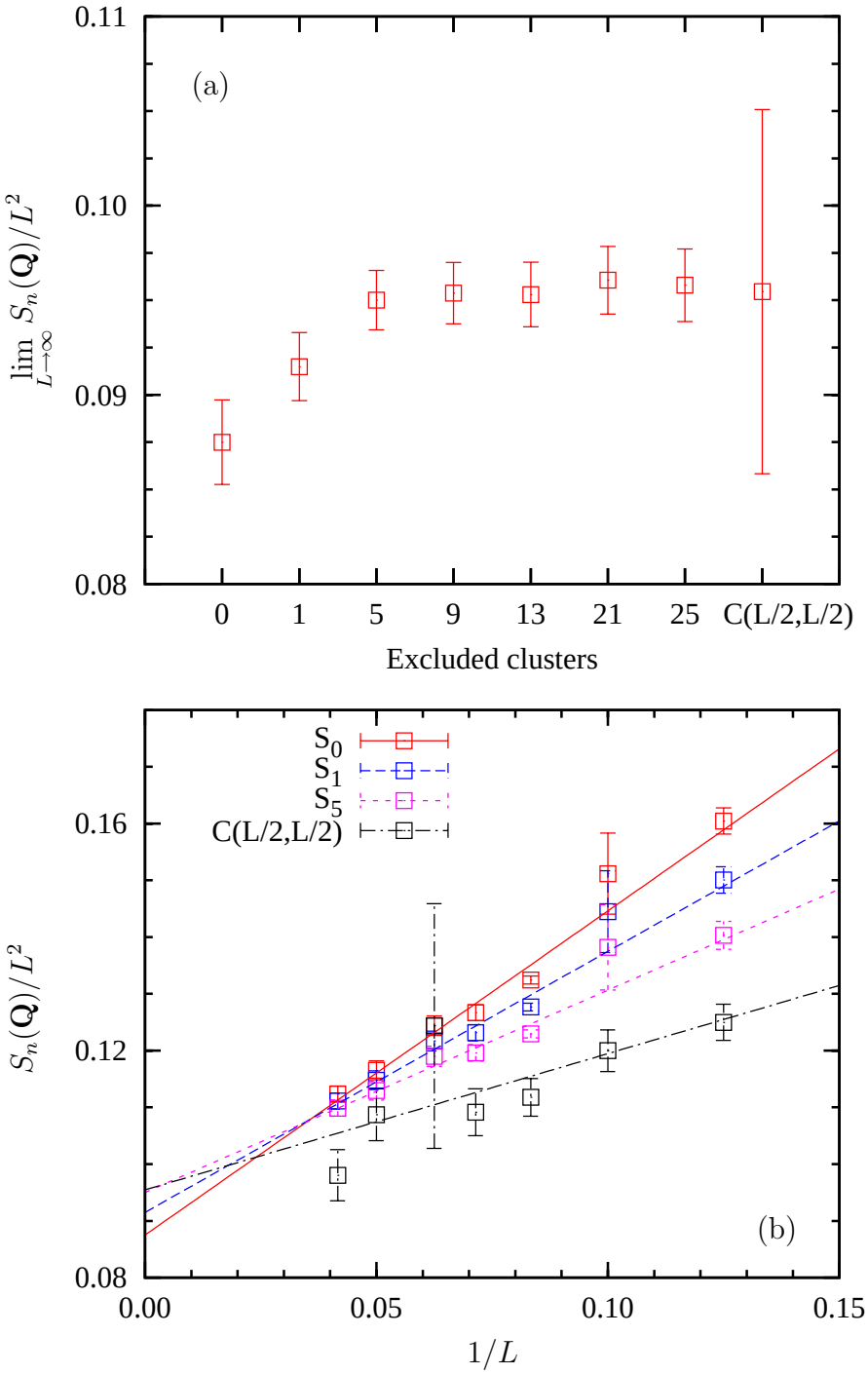

Figure 5.10: Scaling results for $U = 5t$ and $\beta t = 20$. (a) Convergence of the extrapolated value of $S_n(\mathbf{Q})$ as a function of the number of sites in the excluded cluster. See Eq. (5.9) for the definition of S_n. A large fraction of the $1/L^2$ bias is removed without loss in precision. $C(L/2, L/2)$ is plagued by a much larger error bar. (b) Scaling of $S_n(\mathbf{Q})$ for $n = 0$, 1, and 5 and $C(L/2, L/2)$ as a function of the inverse linear lattice size. The extrapolation was performed via a linear least-squares fit in all cases.

a bias roughly proportional to

$$\frac{C(0,0) - C(L/2, L/2)}{L^2} \tag{5.8}$$

is clearly present. This bias is larger for small U since the numerator in Eq. (5.8) gets smaller with increasing U and saturates to the value of the Heisenberg model at $U/t \simeq 8$. On the other hand, the error bars on S are often significantly smaller than on C, a fact that is certainly advantageous in the final finite-size scaling analysis.

A measure of magnetic order that incorporates the extended linearity of C and the better statistical property of S is given by

$$S_n(\mathbf{Q}) = \frac{L^2}{L^2 - n} \sum_{\mathbf{l}, l > l_c} e^{i\mathbf{Q}\cdot\mathbf{l}} C(\mathbf{l}) \,, \tag{5.9}$$

where n is the number of distances shorter than l_c. Equation (5.9) is nothing but the interpolation between S, corresponding to $n = 0$, and C, the case of $n = L^2 - 1$. Figure 5.10(a) shows how the $L \to \infty$ extrapolation evolves by increasing l_c. When l_c is small the linear extrapolation is significantly biased by the small-L results. As l_c increases one reaches statistical convergence already for $l_c = 1$ (corresponding to $n = 5$, the cluster formed by the origin and the nearest neighbors) with minimal loss of statistical precision. That $l_c = 1$ is all is needed to reach statistical convergence is also manifest in Fig. 5.6 where $C(\mathbf{l})$ drops to almost a constant beyond this value.

In Fig. 5.10(b) we show $S_n(\mathbf{Q})/L^2$ versus inverse linear lattice size $1/L$ for $U = 5t$ and $n = 0$, 1, and 5 since as shown in Fig. 5.10(a), there is no real gain in accuracy by excluding larger subclusters. The inverse temperature is $\beta t = 20$, so that S has reached its zero-temperature value regardless of L. We have repeated this finite-size scaling analysis for couplings $U/t = 2$, 3, 4, 6, 7, and 8 and extrapolated to infinite L using a linear least-square fit in $1/L$. In Fig. 5.11, we show the resulting antiferromagnetic order parameter m_{af} as a function of U/t employing the same

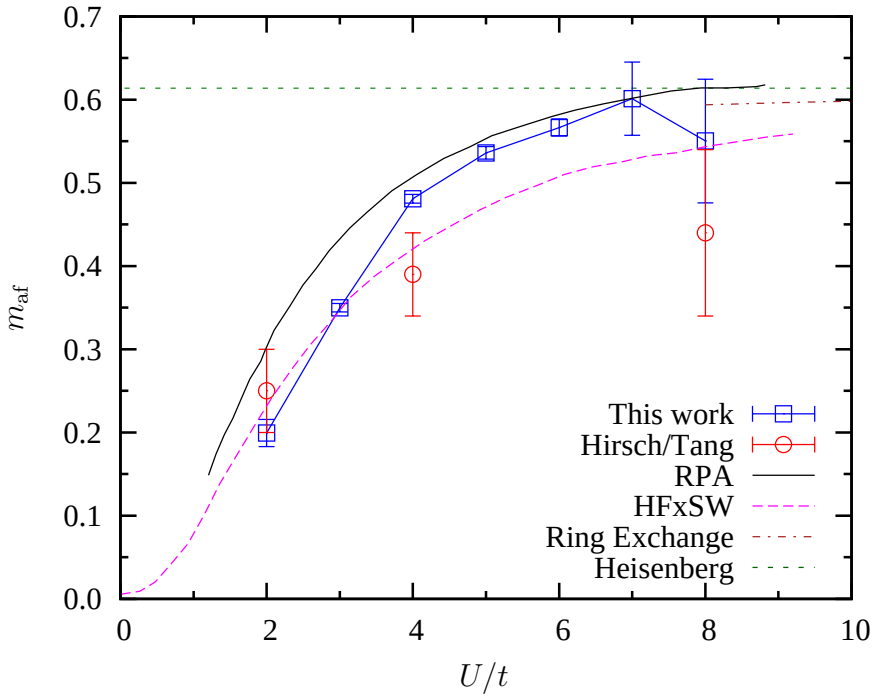

Figure 5.11: Order parameter m_{af} as a function of the interaction strength U. Earlier DQMC values (Ref. 53) are circles and Hartree-Fock theory scaled by the Heisenberg result from Ref. 50 are shown as a dashed magenta line. The green line (short dashes) and the brown line (dashed and dotted) indicate the strong-coupling Heisenberg limits from QMC (Ref. 54) and spin-only low-energy theory with ring-exchange (Ref. 55), respectively. Also shown is the RPA calculation of Ref. 56 (solid black line).

normalization convention of the other Hubbard model studies reported in this figure. The early DQMC values obtained by Hirsch and Tang,[53] which are consistent with the ones obtained here, are shown.

Figure 5.11 also summarizes a number of the available analytic treatments. The dashed magenta line is the result of Hartree-Fock theory scaled by the Heisenberg result at strong-coupling.[50] The solid black line is the random-phase-approximation (RPA) treatment in which the single-particle propagators in the usual RPA sum are also dressed by the one-loop paramagnon correction to their self-energy [56]. Also shown (brown line) are the results of a spin-only low-energy theory [55] which includes not only the usual Heisenberg $J = 4t^2/U$ but also all higher order (e.g., ring exchange) terms up to t^4/U^3. Finally, the dotted green line is the Heisenberg value determined

by Sandvik.[54]

5.5 Summary

In this chapter we have presented the results of determinant quantum Monte Carlo calculations for the magnetic properties of the half-filled square lattice Hubbard Hamiltonian. DQMC allows us to bridge the weak-coupling and strong-coupling regimes with a single methodology, and a particular outcome of our work has been the calculation of the antiferromagnetic order parameter in the ground state as a function of U/t. We expect these values will be useful in validating OLE experiments on the fermion Hubbard model.

By using an improved DQMC code, we have been also able to provide results on larger lattices than those originally explored.[11] This not only has allowed us to do more accurate finite-size scaling for the order parameter but we also obtain considerably better momentum resolution and hence a description of the Green's function $G(\mathbf{k})$ which also offers the prospect of improved contact with time of flight images from optical lattice emulators.[29–32]

This study demonstrates a significantly improved capability to simulate interacting fermion systems, driven by more powerful hardware as well as algorithmic advances. Systems of 500 sites (fermions) can now be handled on a modest cluster of desktop computers. Larger system simulations can easily be contemplated using more powerful hardware and would scale as the cube of the number of particles, in the absence of the sign problem. This remaining sign problem bottleneck prevents the study of the densities of most interest to high-temperature superconductivity, i.e., dopings of $5 - 15\%$ away from half-filling, and motivates the interest in analog computation for the Hubbard Hamiltonian.[57] It should be noted, however, that the sign problem can be rather modest for other densities, e.g., quarter-filling, where we

now have the capability to undertake large scale studies.

Acknowledgements

Research supported by the DOE SciDAC and SSAAP Programs (Grants No. DOE-DE-FC0206ER25793 and No. DOE-DE-FG01-06NA26204), and by ARO under Award No. W911NF0710576 with funds from the DARPA OLE Program. RTS thanks the Aspen Center of Physics for its program on QUantum Simulation/Computation.

5.6 References

[1] C. N. Varney, C.-R. Lee, Z. J. Bai, S. Chiesa, M. Jarrell, and R. T. Scalettar, Quantum Monte Carlo study of the two-dimensional fermion Hubbard model, *Phys. Rev. B* **80**, 075116 (2009).

[2] P. W. Anderson, An Approximate Quantum Theory of the Antiferromagnetic Ground State, *Phys. Rev.* **86**, 694 (1952).

[3] J. Hubbard, Electron Correlations in Narrow Energy Bands, *Proc. Roy. Soc. London A* **276**, 238 (1963).

[4] J. Hubbard, Electron Correlations in Narrow Energy Bands. II. The Degenerate Band Case, *Proc. Roy. Soc. London A* **277**, 237 (1964).

[5] J. Hubbard, Electron Correlations in Narrow Energy Bands. III. An Improved Solution, *Proc. Roy. Soc. London A* **281**, 401 (1964).

[6] J. Hubbard, Electron Correlations in Narrow Energy Bands. IV. The Atomic Representation, *Proc. Roy. Soc. London A* **285**, 542 (1965).

[7] M. Rasetti (ed.), *The Hubbard Model: Recent Results*, vol. 7 of *Series on Advances in Statistical Mechanics* (World Scientific, Singapore, 1991).

[8] A. Montorsi (ed.), *The Hubbard Model: A Collection of Reprints* (World Scientific, Singapore, 1992).

[9] F. Gebhard (ed.), *The Mott Metal-Insulator Transition: Model and Methods* (Springer, New York, 1997).

[10] P. Fazekas, *Lecture Notes on Electron Correlation and Magnetism* (World Scientific, Singapore, 1999).

[11] S. R. White, D. J. Scalapino, R. L. Sugar, N. E. Bickers, and R. T. Scalettar, Attractive and repulsive pairing interaction vertices for the two-dimensional Hubbard model, *Phys. Rev. B* **39**, 839 (1989).

[12] D. J. Scalapino, Does the Hubbard Model Have the Right Stuff, in *Proceedings of the International School of Physics, "Enrico Fermi"*, edited by R. A. Broglia and J. R. Schrieffer (1994), and references cited therein.

[13] D. J. Scalapino, Some Results from Quantum Monte Carlo Studies of the 2D Hubbard Model, *J. Low Temp. Phys.* **95**, 169 (1994).

[14] T. A. Maier, M. Jarrell, T. C. Schulthess, P. R. C. Kent, and J. B. White, Systematic Study of d-Wave Superconductivity in the 2D Repulsive Hubbard Model, *Phys. Rev. Lett.* **95**, 237001 (2005).

[15] D. J. Scalapino, *Handbook of High Temperature Superconductivity*, ch. 13, pp. 495–526 (Springer, New York, 2007).

[16] A. J. Millis, Condensed-matter physics: Stripes of a different stripe, *Nature (London)* **392**, 438 (1998).

[17] S. R. White and D. J. Scalapino, Phase separation and stripe formation in the two-dimensional $t - J$ model: A comparison of numerical results, *Phys. Rev. B* **61**, 6320 (2000).

[18] G. Alvarez, M. Mayr, A. Moreo, and E. Dagotto, Areas of superconductivity and giant proximity effects in underdoped cuprates, *Phys. Rev. B* **71**, 014514 (2005).

[19] C.-C. Chang and S. Zhang, Spatially inhomogeneous phase in the two-dimensional repulsive Hubbard model, *Phys. Rev. B* **78**, 165101 (2008).

[20] J. D. Reger and A. P. Young, Monte Carlo simulations of the spin-1/2 Heisenberg antiferromagnet on a square lattice, *Phys. Rev. B* **37**, 5978 (1988).

[21] T. Moriya, *Spin Fluctuations in Itinerant Electron Magnetism*, vol. 56 of *Springer Series in Solid State Sciences* (Springer-Verlag, Berlin, 1985).

[22] T. Moriya and K. Ueda, Spin fluctuations and high temperature superconductivity, *Adv. Phys.* **49**, 555 (2000).

[23] N. E. Bickers and D. J. Scalapino, Conserving approximations for strongly fluctuating electron systems. I. Formalism and calculational approach, *Ann. Phys. (NY)* **193**, 206 (1989).

[24] Y. Vilk and A.-M. Tremblay, Non-Perturbative Many-Body Approach to the Hubbard Model and Single-Particle Pseudogap, *J. Phys. I* **7**, 1309 (1997).

[25] K. Borejsza and N. Dupuis, Antiferromagnetism and single-particle properties in the two-dimensional half-filled Hubbard model: A nonlinear sigma model approach, *Phys. Rev. B* **69**, 085119 (2004).

[26] H. J. Schultz, Functional Integrals for Correlated Electrons, in *The Hubbard Model: Its Physics and Mathematical Physics*, edited by D. Baeriswyl, D. K. Campbell, J. M. Carmelo, F. Guinea, and E. Louis (Springer, 1995).

[27] B. DeMarco and D. S. Jin, Onset of Fermi Degeneracy in a Trapped Atomic Gas, *Science* **285**, 1703 (1999).

[28] A. G. Truscott, K. E. Strecker, W. I. McAlexander, G. B. Partridge, and R. G. Hulet, Observation of Fermi Pressure in a Gas of Trapped Atoms, *Science* **291**, 2570 (2001).

[29] K. M. O'Hara, S. L. Hemmer, M. E. Gehm, S. R. Granade, and J. E. Thomas, Observation of a Strongly Interacting Degenerate Fermi Gas of Atoms, *Science* **298**, 2179 (2002).

[30] M. Köhl, H. Moritz, T. Stöferle, K. Günter, and T. Esslinger, Fermionic Atoms in a Three Dimensional Optical Lattice: Observing Fermi Surfaces, Dynamics, and Interactions, *Phys. Rev. Lett.* **94**, 080403 (2005).

[31] M. Köhl and T. Esslinger, Fermionic atoms in an optical lattice: a new synthetic material, *Europhys. News* **37**, 18 (2006).

[32] R. Jordens, N. Strohmaier, K. Gunter, H. Moritz, and T. Esslinger, A Mott insulator of fermionic atoms in an optical lattice, *Nature* **455**, 204 (2008).

[33] F. Werner, O. Parcollet, A. Georges, and S. R. Hassan, Interaction-Induced Adiabatic Cooling and Antiferromagnetism of Cold Fermions in Optical Lattices, *Phys. Rev. Lett.* **95**, 056401 (2005).

[34] D. Vollhardt, Investigation of correlated electron systems using the limit of high dimensions, in *Correlated Electron Systems*, edited by V. J. Emery, p. 57 (World Scientific, Singapore, 1993).

[35] N. Bulut, D. J. Scalapino, and S. R. White, Electronic Properties of the Insulating Half-Filled Hubbard Model, *Phys. Rev. Lett.* **73**, 748 (1994).

[36] S. Haas, A. Moreo, and E. Dagotto, Antiferromagnetically Induced Photoemission Band in the Cuprates, *Phys. Rev. Lett.* **74**, 4281 (1995).

[37] A. Georges, G. Kotliar, W. Krauth, and M. J. Rozenberg, Dynamical mean-field theory of strongly correlated fermion systems and the limit of infinite dimensions, *Rev. Mod. Phys.* **68**, 13 (1996).

[38] R. Preuss, W. Hanke, C. Gröber, and H. G. Evertz, Pseudogaps and Their Interplay with Magnetic Excitations in the Doped 2D Hubbard Model, *Phys. Rev. Lett.* **79**, 1122 (1997).

[39] C. Gröber, R. Eder, and W. Hanke, Anomalous low-doping phase of the Hubbard model, *Phys. Rev. B* **62**, 4336 (2000).

[40] T. Maier, M. Jarrell, T. Pruschke, and M. H. Hettler, Quantum cluster theories, *Rev. Mod. Phys.* **77**, 1027 (2005).

[41] A.-M. Daré, L. Raymond, G. Albinet, and A.-M. S. Tremblay, Interaction-induced adiabatic cooling for antiferromagnetism in optical lattices, *Phys. Rev. B* **76**, 064402 (2007).

[42] R. Blankenbecler, D. J. Scalapino, and R. L. Sugar, Monte Carlo calculations of coupled boson-fermion systems. I, *Phys. Rev. D* **24**, 2278 (1981).

[43] R. T. Scalettar, R. M. Noack, and R. R. P. Singh, Ergodicity at large couplings with the determinant Monte Carlo algorithm, *Phys. Rev. B* **44**, 10502 (1991).

[44] G. Alvarez, M. S. Summers, D. E. Maxwell, M. Eisenbach, J. S. Meredith, J. M. Larkin, J. Levesque, T. A. Maier, P. R. C. Kent, E. F. D'Azevedo, and T. C. Schulthess, New algorithm to enable 400+ TFlop/s sustained performance in simulations of disorder effects in high-Tc superconductors, in *SC '08: Proceedings of the 2008 ACM/IEEE conference on Supercomputing*, pp. 1–10 (IEEE Press, Piscataway, NJ, USA, 2008).

[45] K. Michelsons and M. Jarrell, (unpublished).

[46] The development of this new determinant quantum Monte Carlo program is part of the DOE SciDAC program. QUantum Electron Simulation Toolbox (QUEST) is a FORTRAN 90/95 package using new algorithms, such as delayed updating, and integrating modern BLAS/LAPACK numerical kernels. QUEST has integrated several legacy codes by modularizing their computational components for ease of maintenance and program interfacing. QUEST also allows general lattice geometries. The current version can be accessed via http://www.cs.ucdavis.edu/~bai/QUEST.

[47] A useful collection of lectures summarizing some of the alternate approaches to Hubbard model QMC is contained in the NATO Advanced Study Institute: Quantum Monte Carlo Methods in Physics and Chemistry (1998), available at http://www.phys.uri.edu/~nigh/QMC-NATO/webpage/abstracts/lecturers.html. These include "Phase Separation in the 2D Hubbard Model: A Challenging Application of Fixed-Node QMC", (Bachelet); "Quantum Monte Carlo for Lattice Fermions," (Muramatsu); and "Constrained Path Quantum Monte Carlo for Fermions," (Zhang).

[48] K. Van Houcke, E. Kozik, N. V. Prokofév, and B. V. Svistunov, in *Computer Simulation Studies in Condensed Matter Physics XXI*, edited by D. P. Landau, S. P. Lewis, and H. B. Schüttler (Springer-Verlag, Berlin, 2008).

[49] N. V. Prokof'ev and B. V. Svistunov, Bold diagrammatic Monte Carlo: A generic sign-problem tolerant technique for polaron models and possibly interacting many-body problems, *Phys. Rev. B* **77**, 125101 (2008).

[50] J. E. Hirsch, Two-dimensional Hubbard model: Numerical simulation study, *Phys. Rev. B* **31**, 4403 (1985).

[51] E. Y. Loh, J. E. Gubernatis, R. T. Scalettar, S. R. White, D. J. Scalapino, and R. L. Sugar, Sign problem in the numerical simulation of many-electron systems, *Phys. Rev. B* **41**, 9301 (1990).

[52] D. A. Huse, Ground-state staggered magnetization of two-dimensional quantum Heisenberg antiferromagnets, *Phys. Rev. B* **37**, 2380 (1988).

[53] J. E. Hirsch and S. Tang, Antiferromagnetism in the Two-Dimensional Hubbard Model, *Phys. Rev. Lett.* **62**, 591 (1989).

[54] A. W. Sandvik, Finite-size scaling of the ground-state parameters of the two-dimensional Heisenberg model, *Phys. Rev. B* **56**, 11678 (1997).

[55] J.-Y. P. Delannoy, M. J. P. Gingras, P. C. W. Holdsworth, and A.-M. S. Tremblay, Néel order, ring exchange, and charge fluctuations in the half-filled Hubbard model, *Phys. Rev. B* **72**, 115114 (2005).

[56] J. R. Schrieffer, X. G. Wen, and S. C. Zhang, Dynamic spin fluctuations and the bag mechanism of high-Tc superconductivity, *Phys. Rev. B* **39**, 11663 (1989).

[57] R. P. Feynman, Simulating physics with computers, *Inter. J. of Theor. Phys.* **21**, 467 (1982).

Chapter 6

Conclusion

In this dissertation, I have investigated the properties and phases of the Hubbard Hamiltonian in a number of different contexts. In one dimension, I have studied the effects of lattice fluctuations on the extended Hubbard model and the impact of adding fermions to bosons in an optical trap (the Bose-Fermi Hubbard model). Lastly, I have studied the properties of the fermion Hubbard Hamiltonian in two dimensions, particularly the momentum distribution at various fillings and the magnetic order at half-filling. These projects are linked together by a common theme of understanding the effect of electron-electron interactions in causing ordered phases in solids.

For the extended Hubbard Hamiltonian, we have examined the impact of a coupling to the lattice on the spin, charge, and bond order correlations with world-line quantum Monte Carlo. We find that a coupling to the lattice via a static, alternating one-body potential Δ results in an enhancement of the charge density wave (CDW) correlations, causing a reduction in the antiferromagnetism. The boundary between the spin density wave (SDW) and CDW phases is also characterized by abrupt evolution of the individual components of the energy. The energy associated with U increases with the development of double occupancy, and the energy associated with V decreases sharply in the CDW phase. Moreover, the kinetic energy has a maximum

along the SDW-CDW transition line, like the bond-ordered wave (BOW) susceptibility χ_{BOW}, indicating a tendency for BOW order.

When we couple to dynamical lattice distortions via a Holstein electron-phonon coupling, a similar effect occurs. The SDW-CDW transition as a function of the electron-phonon coupling λ is, however, more abrupt than the transition for the static coupling to the lattice Δ, as λ spontaneously breaks the translational symmetry of the lattice. In contrast, Δ explicitly breaks the lattice symmetry, resulting in an increase of CDW order within the SDW phase and a less dramatic crossover.

Comparing the phase boundaries for the QMC results with the $t = 0$ limit illustrates that the two types of coupling have a distinct difference in behavior. When the coupling is static, the CDW phase is generally enhanced by t. At strong-coupling, the hopping has a very small effect on the SDW-CDW phase boundary, while for weak intersite interactions V, the phase boundary is sharply shifted in favor of the CDW phase. When the lattice degrees of freedom are dynamic, the SDW-CDW phase boundary in QMC is uniformly shifted from the $t = 0$ line to increase the critical intersite repulsion, favoring SDW order.

In Chapter 4, the one-dimensional Bose-Fermi Hubbard Hamiltonian was studied with the canonical worm algorithm. In contrast with previous QMC studies that only found that the addition of fermions to a boson system cause an enhancement of the visibility $\mathcal{V}$ (and consequently the superfluidity), we showed that it is possible for fermions to force the bosons in the center of the trap to become a Mott insulator, causing a reduction in $\mathcal{V}$. We also found that $\mathcal{V}$ exhibits kinks reminiscent of those in the pure boson system. The number of kinks in the visibility is directly correlated to the number of the fermions in the trap, and the densities for both particle species overlap exactly in the trap center. These kinks also appear in the trap, interaction, and kinetic energies and coincide with rapid changes in the bosonic and fermionic densities. We found that the center of the trap is occupied by a molecular superfluid,

and that bound pairs of fermions and bosons are being destroyed as the boson-boson interaction strength U_{bb} is increased.

Next, determinant quantum Monte Carlo was used to examine the properties of the half-filled, two-dimensional fermion Hubbard model. The momentum distribution $n(\mathbf{k})$ shows a sharp Fermi surface at weak-coupling, while large interaction strength U broadens $n(\mathbf{k})$. Away from half-filling, the Fermi surface can still be discerned and evolves from a circular topology at low fillings into the rotated square at half-filling. The effective hopping t_{eff} is measured as a function of U, and increasing the interaction strength inhibits the hopping but t_{eff} remains non-zero in the Heisenberg limit.

The magnetic properties of this system were extensively studied. The local moment $\langle m^2 \rangle$ is the zero separation value of the spin-spin correlation function $C(\mathbf{l})$ and was measured as a function of the interaction strength. The on-site repulsion suppresses double occupancy and $\langle m^2 \rangle \rightarrow 1$ in the Heisenberg limit. For non-zero separation, the spin-spin correlation function exhibits antiferromagnetic correlations with long range order. In three dimensions there is a finite Néel temperature T_N at which the system becomes magnetically ordered. In two dimensions, $T_N = 0$ for all U, but an analog of T_N is the temperature T_* at which the correlation length ξ exceeds the lattice size. This is maximized at intermediate U. Additionally, we measure the magnetic structure factor $S(\mathbf{k})$, which is Fourier transform of the spin-spin correlation function. It is sharply peaked at $\mathbf{Q} = (\pi, \pi)$ and saturates at low temperatures, where the saturation temperature depends both on the lattice size and U.

Finite-size scaling can be performed on both the spin-spin correlation function and its Fourier transform to extract the magnetic order parameter m_{af}. We find, however, that the magnetic structure factor produces better statistics than $C(\mathbf{l})$, but $C(\mathbf{l})$ has extended linearity. We introduce a measure of the magnetic order, the excluded cluster structure factor $S_n(\mathbf{Q})$, that incorporates these features of the spin-

spin correlation function and the magnetic structure factor. By performing finite-size analysis on $S_n(\mathbf{Q})$, we measure the interaction dependence of the antiferromagnetic order parameter $m_{\mathrm{af}}(U)$ from weak-coupling to the strong-coupling Heisenberg limit.

We have shown that the two-dimensional Hubbard model can be studied on large lattices. Recent experiments have been done for fermions in an optical lattice at temperatures that are near the Fermi temperature. Large lattices are needed because the confining potential causes a spatial inhomogeneity of the density which can only be resolved if the system is many tens of sites in linear dimension. Currently, we can simulate temperatures two to four times colder than state of the art experiments before the fermion sign problem makes the simulation impossible. We are currently investigating the local properties of the system, including the density and the number fluctuation, for every phase in the wedding cake structure. In addition, we will measure the on-site, nearest-neighbor, and next-nearest-neighbor spin correlations. For systems with a Mott shoulder, we believe that magnetic order will persist for these distances along the Mott shoulder (which is a ring around a superfluid center). One bright area for the future of quantum simulations lies in studying such inhomogeneous systems.

Glossary

bond ordered wave (BOW) A phase of matter characterized by alternating high and low hopping (kinetic energy).

Bose-Einstein condensation A state of matter in which a large fraction of the bosons in a system collapse or condense into the lowest quantum state.

charge density wave (CDW) A phase of matter characterized by a spatial oscillation of charge density.

density profile Spatial distribution of particles

first-order phase transition The first derivative of the free energy with respect to a thermodynamic variable has a discontinuity.

lattice depth Amplitude of the optical lattice potential.

Mott insulator An insulator that results from the magnetic correlations in a material

second-order phase transition The first derivative of the free energy with respect to a thermodynamic variable is continuous but the second derivative exhibits a discontinuity.

spin density wave (SDW) A antiferromagnetic state is characterized by a spatial oscillation of the electron-spin density.

superfluid A phase of matter in which liquids move without friction (the viscosity is zero). For bosons, it is a consequence of Bose-Einstein condensation. For fermions, superfluidity can be achieved through the formation of Cooper pairs.

supersolid A spatially ordered material with superfluid properties. The system has simultaneous diagonal and off-diagonal long-range-order.

tricritical point A point in the phase diagram of a system at which three-phase coexistance terminates.

Index